

DESIGN FOR 3D AGILITY AND VIRTUAL COMPLIANCE USING
PROPRIOCEPTIVE FORCE CONTROL IN DYNAMIC LEGGED ROBOTS

A DISSERTATION
SUBMITTED TO THE ROBOTICS INSTITUTE,
SCHOOL OF COMPUTER SCIENCE AT CARNEGIE MELLON UNIVERSITY
IN PARTIAL FULFILLMENT OF THE REQUIREMENTS
FOR THE DEGREE OF
MASTER OF SCIENCE

CMU-RI-TR-16-39

Simon Kalouche
October 2016

© Copyright by Simon Kalouche 2017
All Rights Reserved

I certify that I have read this dissertation and that, in my opinion, it is fully adequate in scope and quality as a dissertation for the degree of Master of Science.

(Howie Choset) Principal Adviser

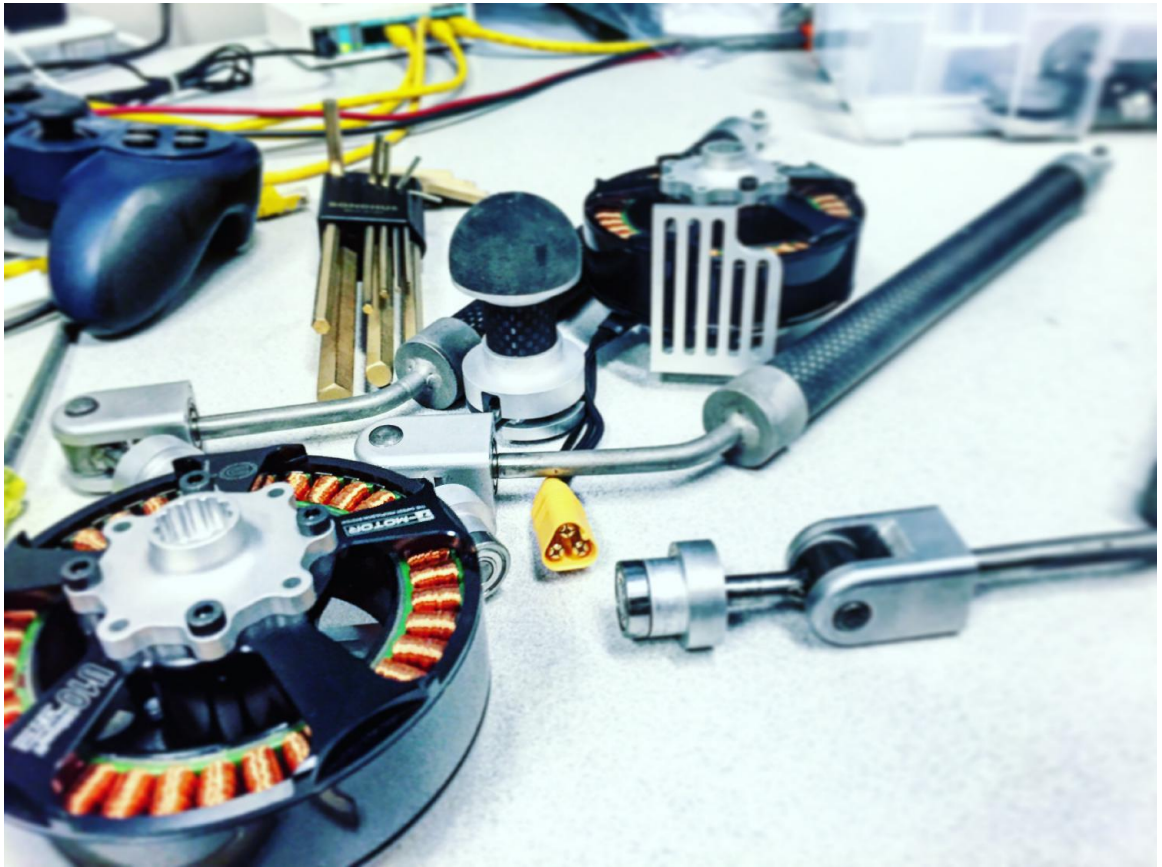
I certify that I have read this dissertation and that, in my opinion, it is fully adequate in scope and quality as a dissertation for the degree of Master of Science.

(Hartmut Geyer)

I certify that I have read this dissertation and that, in my opinion, it is fully adequate in scope and quality as a dissertation for the degree of Master of Science.

(H. Benjamin Brown)

Approved for the Carnegie Mellon University Committee on Graduate Studies



"Simplicity is the ultimate sophistication" - Leonardo Da Vinci

Abstract

For legged robots to be effective in real-world scenarios they must be capable of robustly navigating complex 3D environments using multiple modes of mobility. To achieve mobility over such a broad set of terrain topographies - spanning structured and unstructured environments - an ideal robot will employ both static, highly stable motions (e.g. dexterous crawling, climbing, walking), as well as highly dynamic agility maneuvers (e.g. leaping, inertial reorientation, controlled landing; running; etc.) to optimally traverse the terrain at hand. Therefore, a capable legged robot must be both dexterous, for precise footstep placement, and dynamic, for running and jumping when obstacles are insurmountable by static gaits alone. For example, extra-terrestrial landscapes or a collapsed rubble environment, ubiquitous to war and disaster zones, will contain regions of highly rugged yet relatively level ground. In these environments using high bandwidth virtual compliance, made possible by low impedance actuators, will allow the robot's legs to actively conform to the terrain producing a more efficient and swift mode of locomotion as compared to a statically stable crawling gait which requires accurate terrain mapping and explicit foot step planning. Alternatively if the terrain is both sloped and rugged it may be ideal to crawl or climb slowly using precise footholds made possible by dexterous limbs with a large workspace. Likewise, unstructured or collapsed disaster environments often contain local discontinuities (e.g. cavities, pits, ditches, curbs, obstructions, large local elevation changes relative to the robots leg length, etc.) in the robot's path. For these situations dynamic jumping, controlled inertial re-orientation during flight, and compliant landing would allow the robot to traverse the otherwise insurmountable obstacle and continue forward with its mission. This thesis explores the design of a new electromechanically actuated robot with legs capable of dexterous walking, running, and most significantly, explosive omni-directional jumping and actively compliant landing. A robot with such capabilities does not yet exist but is needed for legged robots to make the next *leap* in real-world effectiveness.

Acknowledgments

I would like to thank my adviser, my parents, family, and friends for supporting me through all my academic and professional endeavors. I would also like to thank all current and past members of the Biorobotics Lab and other affiliates that I have worked with at CMU. Specifically, a great deal of thanks is owed to Youshuang Ding who developed the low-level firmware for the custom motor controllers and was fundamental to the success of this project. Additionally, I would like to thank Ben Brown, Hartmut Geyer, Dave Rollinson, Matthew Travers, Alex Ansari, Chaohui Gong, Arun Rangaprasad, Lu Li, Curtis Layton, Matthew Tesch, Florian Enner, Alex Long, Gavin Kenneally, Ted Kern, and Matt Martone all of whom contributed along the way. This research was conducted with Government support under and awarded by DoD, Air Force Office of Scientific Research, National Defense Science and Engineering Graduate (NDSEG) Fellowship, 32 CFR 168a.

Contents

Abstract	v
Acknowledgments	vi
1 Introduction	1
1.1 Motivation	3
1.2 Hypothesis	7
1.3 Contribution	7
1.4 Thesis Outline	8
2 Design Principles for Dynamic Legged Robots	10
2.1 State of the Art in Dynamic Legged Robots	10
2.2 Leg Design Principles for Agility	14
2.2.1 High Force, High Speed Legs	15
2.2.2 Passive or Active Compliance	17
2.2.3 Robust/Resilient Mechanisms and Structure	18
2.2.4 Energy Efficiency	19
2.3 Actuation Principles for Agility and Virtual Compliance	20
2.3.1 Thermal Specific Torque Density	21
2.3.2 Proprioceptive Actuation and Sensing	30
2.3.3 Mechanical Robustness	31
2.3.4 Energy Efficiency	31
2.4 Actuator Comparison	32
2.4.1 DD v. QDD v. GM v. SEA	32
2.4.2 Experimental Validation of Actuator Properties	39
3 Leg Design for 3D Agility	47
3.1 A Novel 3-RSR Leg Topology	47
3.1.1 Kinematics	48

3.2	Comparison of 3-DoF Leg Topologies	53
3.2.1	Force Envelope Analysis	54
3.2.2	Workspace Analysis	57
3.2.3	Proprioceptive Force Sensitivity Analysis	58
3.2.4	Energy Transfer	59
3.2.5	Summary	60
3.3	Mechanical Design of the 3-RSR	60
3.3.1	Spherical Knee Joint Design	62
3.3.2	Hip Design and Actuator Placement	64
3.3.3	Foot Design	64
3.3.4	Mass Budgeting	65
3.3.5	Finite Element Analysis (FEA)	65
3.4	Actuator Requirements for Omni-Directional Jumping	66
3.5	Quasi-Direct-Drive Actuator	67
3.5.1	Mechanical Design	67
3.5.2	Electrical Design	68
3.5.3	Actuator Control	69
3.6	Sensing	80
3.7	Experiments	80
3.7.1	Complete System	80
3.7.2	Omni-Directional Force Vectoring with Force Plate	81
3.7.3	Omni-Directional Running	81
3.8	Summary and Design Insights of the GOAT leg	81
4	Proprioceptive Force Control for Dynamic Virtual Compliance	86
4.1	Simple Legged Locomotion Controllers	86
4.1.1	SLIP Models	86
4.1.2	Raibert Hopping Controller	89
4.2	Virtual Model Control for Compliant Dynamic Motions	91
4.2.1	Virtual Joint Compliance	92
4.2.2	Virtual Full Leg Compliance	92
4.2.3	Simulation Model	93
4.2.4	Experimental Validation	93
4.2.5	Virtual Compliance Experiments	96
4.2.6	Proprioceptive Foot Force Sensing	100
4.2.7	1-DoF Vertical Hopping	100
5	Conclusion and Future Work	103

List of Tables

2.1	Results for a series of actuation tests on 4 types of actuators. All tests were done using a single axis SRI M2210E torque load cell and all actuators were commanded at control frequencies of 1kHz. Gear motor bandwidth is especially poor which is most likely attributed to the large amount of backlash present in the gear train. Higher end gearmotors with lower backlash can be expected to perform much better than results obtained here and with a higher bandwidth than SEAs as suggested by theory and other literature.	46
3.1	Comparison of leg parameters for three different 3-DoF leg topologies.	54
3.2	Comparison of performance measures for 3-DoF leg topologies.	60
3.3	Lookup table for six-step square commutation [47].	71
4.1	State machine for Raibert hopping controller [6].	90
4.2	Agile Performance Comparison in Dynamic Legged Robots. The bulk of the data from this table has been tabulated and presented originally by Kenneally et. al in [12]. The performance specifications of GOAT are added to Kenneally's table for purpose of comparison to other dynamic legged machines. We introduce a slightly different metric however for vertical agility which is just the max jumping height of the robot's body and the energy delivered to the body during the jump. DoF is the degrees of freedom per leg.	98

List of Figures

1.1	Goat jumping across a cliff. Source: W.Wayne Lockwood, M.D./Corbis, Britannica.	2
1.2	Boston Dynamics legged robots in 2016 [2].	3
2.1	The current state of art in dynamic legged machines in 2016: 1) Boston Dynamics (BDI) SpotMini, 2) Penn/Ghost Robotics Minitaur, 3) ATRIAS, 4) RHex and Canid, 5) StarLETH, 6) BDI Spot, 7) MIT Cheetah, 8) BDI Atlas.	11
2.2	Common robot leg topologies. The robots shown from left to right include the Raibert quadruped/monopod [6], BDI Spot [2] and MIT Cheetah [9][38], Boston Dynamics Big Dog [7], Penn/Ghost Robotics Minitaur [12] and ATRIAS [10], the GOAT leg with a parallel spatial 3-RSR topology.	13
2.3	An infrared image of a motor winding captured by a Flir Thermal Camera. It is important to select a motor that not only has a high torque density but one that can sustain that torque over periods of time without overheating. The image shows temperatures higher than 100°C, therefore to prevent motor burnout thermal management is necessary.	21
2.4	(a) Flux density in steel saturates at around 2 Tesla where flux densities any higher than 2 T produce rapidly increasing reluctance and the core loses ability to conduct flux. (b) Minimizing the air gap decreases magnetic reluctance which increases flux and flux density. (c) Using teeth and slots in the stator allows magnetic force on the winding coils to be transferred more effectively to rotor torque while reducing the air gap. Figure Source: [46].	23
2.5	Simplified brushless DC motor cross-section. The copper winding coils are shown by the gold dots and x's indicating wire traveling out-of and into the page respectively. The dotted lines represent the end-turn segments of the coils which do not contribute to magnetic interaction forces.	26

2.6	Comparison of actuation strategies with respect to meeting the requirements of various robot applications including: Dynamic Legged Robots (DLR), Human-Robot Interaction (HRI), Industrial Robots (IR), Quadrotors/Aerial Robots (QAR), and Wheeled Robots (WR). An optimal actuator could be determined by maximizing the area enclosed by the polygon of a weighted web graph.	33
2.7	(a) Model of a series elastic actuator with series spring stiffness k_s , spring dampening b_s , gear reduction n , and motor rotor inertia I_m , (b) is a model of a stiff gear motor, (c) is a model of a quasi-direct-drive actuator, (d) is a model of a direct-drive actuator. τ_m and τ_l are the motor and load torques for a fixed input and output.	36
2.8	Impact of spring stiffness on control bandwidth for series elastic actuators.	37
2.9	Relationship between actuator inertia and spring stiffness on control bandwidth and impact force.	37
2.10	The ideal configuration for maximizing reduction of a single-stage planetary gear is to fix the ring gear, couple the sun gear to the motor input, and the planet carrier to the output. Circles represent the gear's pitch radius so teeth are not shown.	39
2.11	Actuators configured as (a) Direct drive, (b) quasi-direct-drive (1-stage planetary), (c) gear motor (2-stage planetary), and (d) Hebi X-5 SEA module in the torque testing rig. The motor back is fixed directly to a mounting plate and the output of the actuator is coupled to the 1-axis load cell whose housing is also bolted to the rig.	40
2.12	Experimental torque bandwidth testing for a direct-drive T-motor commanded sinusoidal torque trajectories at 20, 70 and 100 Hz.	42
2.13	Experimental torque bandwidth testing for a QDD (T-motor with a 1-stage planetary gear train) commanded sinusoidal torque trajectories at 20, 30 and 40 Hz	42
2.14	Experimental torque bandwidth testing for a GM (T-motor with a 2-stage planetary gear train) commanded sinusoidal torque trajectories at 10, 20 and 40 Hz	42
2.15	Experimental torque bandwidth testing for a SEA (Hebi X5-1) commanded sinusoidal torque trajectories at 10, 20 and 30 Hz.	43
2.16	(a) DD, (b) QDD, (c) GM, (d) SEA. Rise time, settling time, peak time, overshoot, and proprioceptive torque sensing accuracy and error are calculated using the following step response experiments shown here.	44
2.17	Methodology for actuator selection and design starting from the basic, unmodified electric motor where torque is the limiting resource. This specific methodology flow results in robots like StarlETH [11], ATRIAS [10], and BiMASC [21].	45
2.18	Methodology for actuator selection and design starting from the basic, unmodified electric motor where torque is the limiting resource. This specific methodology flow results in robots like MIT Cheetah [9], Penn Minitaur [12], and GOAT, the robot introduced in this thesis.	45

3.1	CAD Rendering of a viable quadruped using the GOAT leg topology.	48
3.2	the 3-RSR leg topology decomposed into the individual joints at the hip R_1 , knee R_2, R_3, R_4 , and ankle R_5 . Although the mechanism is a 3-RSR the physical realization of the topology is achieved using a 3-RRRRR where the three knee R-joints intersect at a single point for an effective mobility equal to that of a spherical joint.	49
3.3	Optimization of link 1 length, l_1 , for maximum workspace and force production based on the objective function in eq. 3.5. Here the objective function is scaled to fit the left y-axis.	50
3.4	Characterization of the joint torques, foot position, foot velocity, and foot force for a vertical jump. The foot force plot shows force produced by constant hip joint torques of 5 N-m for an example vertical foot trajectory where all 3 hip angles are the same due to symmetry. The joint torque plot shows the actuator torques required to produce a constant 100N for downwards at the foot. For a vertical leg trajectory all 3 joint angles are the same for each point in the trajectory since the mechanism is symmetric. For omni-directional force vectoring the joint angles and torques will not be the same.	52
3.5	Kinematic diagrams showing leg parameters (Table 3.1 and joint axes for (a) 3-DoF prismatic, (b) 3-DoF series-articulated, and (c) 3-DoF 3-RSR Parallel Spatial topologies.	53
3.6	Sagittal-plane force envelope comparison. The y and z axes correspond to the coordinates of the foot in the leg frame. The color contour represents the required torque from each actuator to produce the defined force wrench at that coordinate (i.e. position) in the workspace. (a) and (b) represent forces identical to those described in fig. 3.7.	55
3.7	Frontal-plane force envelope of the 3-RSR leg as compared to the series-articulated and prismatic legs. The x and y axes correspond to the coordinates of the foot in the leg frame. The color contour represents the required torque from each actuator to produce the defined force wrench at that foot coordinate in the workspace. In (a) the force generated at the foot follows eq. 3.12, while the foot force in (b) is always -100 N in the z-direction. (c) shows a simulation of the 3-RSR leg producing a force vectored in the direction indicated by the orange arrow. The green arrows indicate relative magnitude of the 3 actuator torques required to produce the desired foot force. For a vertical foot trajectory & force the 3 green arrows will be equal.	56
3.8	Workspace volume for the (a) prismatic, (b) series-articulated, & (c) 3-RSR topologies shown on a quadruped body hiding all but 1 leg. Joint limits used for series-articulated & prismatic legs are based on the joint limits of the MIT Cheetah & the Raibert Hopper.	57

3.9	(a) Top view of frontal plane for each leg topology. The contour plot indicates by color what the proprioceptive sensitivity (i.e. torque in N-m) of each actuator is to a 1 N force acting on the foot. The coordinate on the plot corresponds to the $\{x,y\}$ position of the foot. (b) Matlab kinematic simulation of each foot topology vectoring force in an arbitrary direction.	58
3.10	Side view of the sagittal plane for each leg topology. The contour plot indicates by color what the proprioceptive sensitivity (i.e. torque in N-m) of each actuator is to a 1 N force acting on the foot. The coordinate on the plot corresponds to the y,z position of the foot.	59
3.11	Renderings of CAD models for the 3-RSR leg design and actuator modules.	60
3.12	Knee joint design showing the 3 revolute joints with intersecting axes. Solidworks FEA results indicate that stresses as high as 123 ksi are present at the bearing support shaft of the distal knee segment with a conservative applied force of 300 N and safety factor of 4. Therefore, this component is machined from medium carbon steel with 125 ksi yield strength in contrast to most of the other components which are machined from 7075 Aluminum with 73 ksi yield strength.	61
3.13	FEA was conducted on each component and the two other critical components were determined to be (a) the other extended shaft in the knee (R_2) and (b) the ankle link which connects the foot to the carbon fiber l_2 rod. A static analysis was used to determine the maximum expected force each part could see and those forces ranging from 75N to 200N were applied in the FEA.	62
3.14	Optimization plot showing the relationship between the fixed knee angle and total hip joint range.	63
3.15	Various mechanical components of the 3-RSR leg including foot, knee, and driven link l_1	64
3.16	The Tiger Motor U10 shown here has a large 40 mm gap radius and a lightweight frame. The T-motor U8, U10, and U12 were determined to have one of the highest thermal specific torques of any COTS motor ($0.42 \frac{Nm}{kgC^\circ}$ at $r_{gap} = 40 \text{ mm}$) [43]. For reference the custom MIT cheetah motors have a thermal specific torque of $0.71 \frac{Nm}{kgC^\circ}$ at $r_{gap} = 49 \text{ mm}$ [9].	68
3.17	The quasi-direct-drive actuator module driven by a T-motor U10 with a single stage Matex 1:7 planetary gear stage.	69
3.18	Custom GOAT motor driver configured with a Piccolo TMS320F28069M MCU and a DRV8301 Bridge Driver which drives 6 N-channel Vishay SUM110N06-05L 60 V MOSFETs with 175°C temperature limit.	70
3.19	The custom Hebi Robotics communications board outfitted with a 32-bit ARM Cortex processor, Ethernet switch, and SPI port among other I/O ports for prototyping. . .	70

3.20	(a) is a simple motor model showing torque production for three different phase alignments of the rotor's permanent magnet and stator's electromagnetic fields. (b) shows a decomposition of magnetic force or pull direction into two components: one that produces torque and one that pulls outward and wastes energy. The purpose of FOC is to continuously apply a magnetic field in the stator windings which converts all the magnetic force into the component that produces torque. (c) shows the phase-shift that exists between phase winding voltage and phase current, which is around 20° here. (d) shows the commanded voltage sinusoids vs. electrical angle and the corresponding magnetic field produced by the energized windings. Figure source: [56].	72
3.21	(a) is a flow chart showing the FOC commutation. (b) is the control strategy which minimizes I_d and maximizes I_q . Figure source: [56].	73
3.22	Representation the input (a, b, c) winding reference frame and the rotating $d-q$ frame for a 4-pole brushless motor.	73
3.23	Output of the RMS current limiter which monitors the RMS current and saturates the commanded output torque when necessary to remain within the motor winding's thermal limits.	75
3.24	Thermal analysis showing the time response in winding temperature to 4 commanded torques ranging from 1.19 N-m to 2.85 N-m with associated thermal time constants. Thermal time constant was calculated by 63% of the time taken to reach steady-state. If steady state was not reached the maximum temperature was used. A FLIR E40 Infrared Thermal Imaging Camera was used to collect real-time temperature data on the windings.	76
3.25	A FLIR E40 Infrared Thermal Imaging Camera was used to observe the temperature gradient over the motor windings and the PCB containing the motor driver FET bridges. (a) is a top-view IR image of the torque test rig with the motor driver PCB (cursor 1) and the T-motor (cursor 2). (b) shows a closer view of the T-motor U10. The thermal image depicts which stator winding poles are being energized and the temperature at those windings.	76
3.26	Schematic wiring diagram of the electronics for a single GOAT actuator.	78

3.27	A torque vs current plot of the motor shows the torque constant to be $0.072 \frac{N-m}{A}$. The magnetic flux in the motor core begins to saturate at 70 A and the thermal limits of the motor driver half-bridges reach their thermal limits between 75-80 A. The shaded color zones indicate allowable duty time and duration of holding torque. The green region indicates infinite holding as this region is within the continuous current and thermal limits of the motor; green-yellow corresponds to duty times ranging from 5 minutes to 20 seconds; yellow indicates short duty cycles of up to a few seconds; orange indicates duty cycles less than 1 second; and red indicates peak instantaneous torques with a duty cycle of a few milliseconds.	79
3.28	Torque calibration to determine the relationship between the commanded value in the custom motor-controller Matlab API.	79
3.29	Data from the 6-axis force-torque load cell was collected to determine the ground reaction forces generated at the foot of the robot. The commanded and actual forces are presented. The data shows that the leg can produce equal forces along all vectors of the frontal plane (i.e. any combination of F_x and F_y within the actuators limits). This corresponds with the analytical data presented in Figs. 3.6 and 3.7.	82
3.30	Passive landing tests were performed using 3 COTS torsion springs ($k_s = 4.11 \frac{N-m}{rad}$) in the 3 hip R-joints. The left image shows resting knee-below-hip position while the right image shows the 3-RSR knee-above-hip configuration absorbing energy upon landing.	82
3.31	GOAT Leg prototype with T-motor U10 actuators mounted in direct-drive configuration.	83
3.32	GOAT Leg prototype and experimental 1-DoF vertical jumping test bed. Electronics and power (LiPo battery — blue) are both shown in the bottom right image off-board, as tested. The gray ground plate the robot is standing on is a 6-axis force-torque load cell.	84
4.1	Spring-loaded inverted pendulum (SLIP) model with spring stiffness k and nominal leg length l_0 for (a) a 1-DoF hopper and (b) a 2-DoF hopper [61].	88
4.2	Leg model for the Raibert hopper parallel controller.	90
4.3	MATLAB SimMechanics model of the 3-DoF, 3-RSR leg being simulated for 1-DoF hopping and compliant landing.	94
4.4	Calibration curves for the impedance controller based on gain scheduling. The impedance controller is based takes a position error and desired torque as inputs and outputs a position gain which generates the commanded input torque.	95
4.5	Schematic of the hopping control architecture using virtual model control to virtually emulate a mechanical spring/damper. This allows the leg to compliantly absorb the impact during touchdown/landing.	95

4.6	Experimental results using impedance controller based on continuous gain scheduling. The position error increases linearly with time but the commanded torque trajectory is non-linear (sinusoidal). Any arbitrary torque trajectory can be chosen; the continuous gain scheduler will modulate the gain based on the desired torque and the current position error. The torque trajectory is followed within 10% error by the direct-drive actuator at a bandwidth greater than 200 Hz.	97
4.7	High jump experiments with the GOAT leg delivering 20.11 J of energy to produce a maximum jump height of 82 cm which is more than double the body height. For Full video: https://www.youtube.com/watch?v=n319xVomJTQ	97
4.8	Experiments were conducted to compare (from left to right) 1) physical joint compliance using mechanical torsion springs in each of the three hip joints without any motors, 2) virtual joint compliance where motors are used to emulate torsion springs of various stiffness in the hip (no physical springs), and 3) virtual full leg compliance where motors are used to emulate the forces of a spring-damper connecting the hip to the foot (no physical springs). Virtual component placement is shown in blue. . .	99
4.9	Experiments using 3 different virtual spring stiffness' and dampening coefficients and observing the response upon landing. The top two plots have virtual joint compliance with stiffness of 18 and 36 Nm/rad while the bottom plot has a full leg virtual rectified spring stiffness of 250 N/m and dampening of 10 N-s/m. The response for the whole leg compliance is ideal with the shown parameters.	99
4.10	To determine the accuracy of the proprioceptive sensing of foot forces through motor current the actuator torque feedback is plugged into eq 4.33 to calculate the foot force. This calculated proprioceptive foot force is then compared to the ground truth from the 6-axis force-torque plate. The data shown here is from a jump/land experiment with virtual whole leg compliance with stiffness of 400 N/m and dampening of 15 N-s/m.	101
4.11	Data from a second test showing proprioceptive foot force sensing accuracy during a jump/land experiment.	102
4.12	GOAT leg performing continuous 30 cm hopping at 1.5 Hz on a 1-DoF test rig. . . .	102

Chapter 1

Introduction

With the advent of modern machinery society has benefited tremendously in the transportation of people and materials. Machines like boats, trains, cars, and planes have all been invented to overcome the inherent speed and distance limitations of humans. While these conventional vehicles have enabled us to travel the globe more efficiently, they still require some degree of infrastructure and are incapable of directly accessing many of Earth's most isolated and elusive locations where sure-footed animals roam freely.

As man-kind pushes the barriers of exploration further to extra-terrestrial lands where flat terrain is sparse and the atmosphere is drastically less dense, conventional wheeled vehicles and aircraft lose much of the utility they have here on Earth. Thus, an exhaustive exploration of these impassable environments requires an alternative approach in design – an approach to which we can turn to biology for inspiration.

For example, the mountain goat (*Oreamnos americanus*) is notorious for its awing mobility in seemingly untraversable terrains. This legged mammal exhibits unmatched multi-modal mobility to scale steep, mountainous and cliff-like terrains – often using its dexterous limbs to precisely position its feet and toes, maintaining static balance on cliffs with a narrow base of support. Between instances of static stability the mountain goat exhibits intervals of highly dynamic and powerful jumping maneuvers to change elevation or reach locations unreachable by statically stable motions alone. In addition to climbing trees, rocks, and cliffs, the mountain goat is capable of jumping up to 12 feet in a single leap, running up to 15 mph and paddle swimming in bodies of water [1]. This form of multi-modal mobility is unsurpassed and remains greatly unmatched by conventional land vehicles. Therefore, for decades scientists and researchers have turned to biology and specifically cursorial creatures for inspiration in designing more competent and agile machines.

As humans and animals subconsciously move through the world with our inherent finesse we often overlook the complexity of mobility and the lengthy evolutionary process which has afforded us these abilities that we still do not fully comprehend. Therefore, this thesis is a stepping stone



Figure 1.1: Goat jumping across a cliff. Source: W.Wayne Lockwood, M.D./Corbis, Britannica.

in the arduous endeavor to create machines with mobility matching and exceeding that of their mammalian cursorial counterparts.

There is still much progress to be made in transforming the current state-of-art in legged robots from research projects, operating in controlled environments, to deployable and robust platforms with real-world utility and mobility that approaches that of humans and animals. The most notable progress in legged robots deployed in unstructured, real-world, environments is demonstrated by recent videos released by Boston Dynamics. These robots include Atlas, BigDog, Spot and the all electric SpotMini shown in Fig. 1.2 [2]-[4]. These videos show both biped and quadruped, hydraulically and electrically actuated, robot's navigating everything from forested landscapes to confined spaces and staircases in warehouses and residential environments [4]. However, as control, autonomous balancing, and legged motion planning algorithms continue to progress the largest barrier preventing these machines from reaching real-world utility continues to be 1) multi-modal mobility using force control to interact compliantly with the world like humans and animals; and 2) power efficiency to ensure tasks with reasonable durations can be executed without the need for manual recharging or external power supplies or tethers.

Specifically, this dissertation is geared towards the development of a new leg topology and actuation paradigm which will enable legged machines to use proprioceptive force control to exhibit multi-modal 3D agility through both static and highly dynamic motions. This work discusses design concepts, actuation principles, implementation details, mathematical analysis, and control strategies for achieving a new level of 3D agility and active compliance in dynamic legged robots that hopefully one day will be adept for exhaustive exploration of extra-terrestrial worlds.



Figure 1.2: Boston Dynamics legged robots in 2016 [2].

1.1 Motivation

It is estimated that nearly 50% of Earth's landmass is currently inaccessible to wheeled or tracked machines [6]. Humans and animals, however, are readily able to access most of these areas and it is desirable that robots and machines be able to do the same. Biologically inspired robots, specifically legged robots, offer enhanced mobility in these impassable environments in situations where it is unsafe or unfeasible for humans to travel. Although there exist dozens of promising legged robots today, most are limited dynamically and all make significant trade-offs between efficiency, dexterity, and dynamic mobility [7]-[16]. Thus, there are still open questions pertaining to leg topology and actuation schemes which best optimizes performance across the efficiency, dexterity, and dynamic mobility spectrum.

For legged robots to be effective in real-world scenarios they must be capable of robustly navigating complex 3D environments using multiple modes of mobility. To achieve mobility over such a broad set of terrain topographies - spanning structured and unstructured environments - an ideal robot will employ both static, highly stable motions (e.g. dexterous crawling, climbing, walking), as well as highly dynamic agility maneuvers (e.g. leaping; compliant landing; running; etc.) to optimally traverse the terrain at hand. Therefore, a capable legged robot must be both dexterous, for precise footstep placement, and dynamic, for running and jumping when obstacles are insurmountable by static gaits alone. For example, extra-terrestrial landscapes or a collapsed rubble

environment, ubiquitous to war and disaster zones, will contain regions of highly rugged yet relatively level ground. In these environments using high bandwidth virtual compliance, made possible by low impedance actuators, will allow the robot's legs to actively conform to the terrain producing a more efficient and swift mode of locomotion as compared to a statically stable crawling gait which requires accurate terrain mapping and explicit foot step planning. Alternatively if the terrain is both sloped and rugged it may be ideal to crawl or climb slowly using precise footholds made possible by dexterous limbs with a large workspace. Likewise, collapsed war and disaster zones often contain local discontinuities in the robot's path. For these situations dynamic jumping, controlled inertial re-orientation during flight, and controlled landing would allow the robot to traverse the otherwise insurmountable obstacle and continue forward with its mission. To accomplish this range of mobility the conventional pure position based control method will not be adequate. Thus, machines must be designed to enable both accurate position and **force** control working in parallel.

The real utility of legged robots is in traveling to locations that are not safe or hard to reach by humans. These areas of interest are characterized by:

1. Highly unstructured terrains, that are often impassible to wheeled vehicles and currently existing legged robots;
2. Obstacles of large and steep variations in ground elevation (relative to the robots height) creating discontinuous paths for walking (i.e. theres a limit to the slope of a terrain that can be walked over which is around 45 degrees for humans);
3. Pits, holes, ditches and local cavities which also create discontinuities in a walking path;
4. Tight and compact spaces where turning or reorienting to then walk or jump is not possible or ideal
5. Long distance missions over diverse terrains where different gaits or modes of locomotion can improve both mobility, efficiency, and longevity.

Legged robots utilize a variety of leg topologies and actuation strategies to enable mobility over such a large set of terrains. However, the most prominent, currently existing dynamic legged robots (SpotMini [4], MIT Cheetah [9] [4], ATRIAS [10], Minitaur [12], etc.) shown in Fig. 2.1, share a fundamental shortcoming that constrains the leg's most powerful actuators, force producing capability, and thus dynamic mobility, to the robots sagittal plane. Sagittally constrained and 2.5D dynamic motions severely inhibit a robots mobility in real-world, complex, 3D environments. For instance, in tight spaces with discontinuous walking paths, current robots would be required to turn in place to face a desired heading and then walk or jump forward over/onto an obstacle. This is less ideal than simply moving or jumping in the direction of the desired heading without having to reorient the body first. Another scenario is in any human environment where omni-wheels are

currently used but limited by steps, cables on the ground, etc. In these environments an omnidirectional legged robot would be capable in terms of mobility. In other words, currently existing dynamic robots exhibit exceptional mobility in the forward walking and running direction but are rather unexceptional at running and jumping sideways, diagonally, or backwards. This limitation is a direct consequence of the current leg topologies and designs being researched, explored, and developed.

In addition to limited mobility in the full space of $SE(3)$ today's dynamically capable legged robots use leg topologies with Jacobians characterized by an unequal distribution of torque requirements across the leg's actuators needed to produce adequate foot forces for running and jumping. This characteristic of leg design yields unused resources (i.e. actuators) while simultaneously demanding extreme performance from other actuators. An ideal leg design would equally distribute loads across all actuators to avoid wasting resources while reducing system mass and minimizing the potential of damaging over-burdened components.

If a leg topology burdens one actuator with the majority of the load for running, walking, and jumping that actuator must have sufficient torque and speed to do so. The most common method of achieving the required torque is via a transmission which allows the abundant resource of speed in electromagnetic actuators to be converted to torque, a more limited resource. While transmissions such as gears, belts, pulleys, and linkages can multiply an actuators torque, they introduce undesired complexities such as backlash, friction, and other modeling non-linearities all of which contribute to a system's mechanical impedance [17]. Mechanical impedance is the inverse of force transparency, thus a challenge becomes imminent as one goes about designing a machine with sufficient torque for dynamic motions yet high force transparency (i.e. low impedance) for utilizing force control to compliantly interact with the surrounding environment.

For effective high-speed traversal through unmapped, unstructured environments a robot must be able to efficiently deliver energy and absorb impacts from jumping and landing. To address this requirement many researcher's have designed robot's with inherent, built-in, mechanical compliance using pneumatics, series-elasticity, leaf springs, and bow-legs [6][10][19]. While this inherent compliance is advantageous in protecting actuator transmissions and passively conforming to uncertainties in the environment, mechanical compliance undesirably:

1. imposes limits on actuation bandwidth;
2. fixes a single mechanical spring and dampening coefficient to the leg which is typically tuned to a single specific running speed or ground stiffness and not optimal in general for all situations [21];
3. requires large and inefficient mechanisms to achieve variable mechanical stiffness [21];
4. introduces control complexities when attempting to accurately model the compliance which is often non-linear [22][24].

Therefore, to address the requirement of absorbing and delivering energy while avoiding the issues associated with mechanical compliance, the ability of a robot to virtually mimic the role of a mechanical spring and damper becomes very desirable. This ability can be accomplished using high fidelity virtual model control. Virtual model control is force-control based frame-work in which a robot's actuators can be used to emulate the dynamics of mechanical components such as springs and dampers [25]. Virtual model control affords a robot the ability to tune leg stiffness and dampening, in real-time, to be optimal for any terrain or running speed [25].

High fidelity virtual model control, which reacts to disturbances on the millisecond time-scale, requires high bandwidth, high accuracy, force sensing and control. A common approach to achieve this level of force control has been to use series-elastic actuators (SEAs) or place a load cell, force sensor, or strain gauge at the end-effector which directly interacts with the world (i.e. the foot for legged robots). Using SEAs for force control can work but it associated with the previously mentioned limitations when inherent mechanical compliance is built-in to the system dynamics. For dynamic legged robots it is also disadvantageous to place a sensor distally at the foot to measure ground reaction forces required for virtual model control. This is because 1) adding distal mass (from a load cell) the to the leg will increase limb inertia which reduces limb acceleration hindering high speed dynamics and 2) foot impact forces reach multiple times the robot's total weight and are cyclic by nature of hopping and running which ultimately requires a challenging level of robustness and longevity or decreases sensor lifetime. Therefore, it is ideal to use sensors that are 1) proximal to the body, 2) not in direct contact with the environment (for increased longevity), and 3) capable of high bandwidth sensing.

A solution that addresses these three criteria is measuring motor torque via motor current and using the leg Jacobian to transform measured joint torques into an estimate of the force-torque wrench at the foot (i.e. the ground reaction force). This approach requires no distal sensors, does not put the sensor directly in the contact load path, and is capable of very high bandwidth sensing. However, using joint torque to estimate foot force has its own set of design requirements. For motor current to be a good indicator of joint torque and similarly for joint torque to be a good indicator of foot force the entire leg design (actuators, joints, linkages, structure, etc.) **must** have extremely low mechanical impedance and high force transparency [17][26]. This means the design of every element in the leg must minimize mass, friction, stiction, inertia, reflected inertia, compliance, and backlash. This last and most cumbersome requirement negates the use of nearly all transmission devices which introduce one or more of the listed impedance sources. Additionally, intelligent selection of leg topology plays an important role in minimizing actuator torque requirements to allow for minimal use of transmissions [26]. The design methodology used for the creation and synthesis of the GOAT leg as well as other dynamic robot legs is shown in Fig. 2.17 and 2.18.

With the motivation set, the purpose of this thesis is to describe how to address these design requirements with the initial task of delivering and compliantly absorbing large 3D forces using

robotic limbs and the ultimate goal of improved real-world mobility and utility of legged robots.

1.2 Hypothesis

Considering the initial task of efficiently delivering and absorbing the energy from large 3D forces using a robot’s limbs, this thesis explores the following hypothesis:

A task-optimized parallel 3-DoF leg topology can allow a robotic leg to be dynamic in 3 dimensions while also affording it the ability to use direct-drive actuation — with accurate proprioceptive force sensing — for achieving high fidelity virtual compliance all while maintaining mechanical robustness, low limb inertia, and a usable workspace for agile legged locomotion. This complimentary combination of leg topology and actuation will produce a robot with unparalleled 3D agility.

This hypothesis considers and addresses the fact that traditional parallel mechanisms have a very limited workspace that would typically not be adequate for legged locomotion. It also addresses mechanical robustness in the case of the Delta robot which does have a fairly decent workspace for a parallel mechanism but is notoriously known for being incapable of bearing or delivering large end-effector loads which are pervasive in legged locomotion. The following chapters of this dissertation work toward a validation of the hypothesis stated above.

1.3 Contribution

While this thesis explores the full design methodology used to conceive a completely new leg topology designed for 3D agility, the main contributions of this work include:

1. detailing the synthesis, mechanical design, analysis, characterization, optimization, and physical realization of the 3-RSR parallel leg topology enabling omni-directional force and acceleration vectoring.
2. an exhaustive survey and trade-off analysis, which illuminates the competing design objectives that a designer should consider when designing task specific robotic legs with complimentary topologies, actuation strategies, and control schemes.
3. the successful demonstration — on real hardware — of a mechanically robust 3-DoF, 3-RSR leg performing: a) *explosive* jumping and landing using high fidelity virtual model control and b) high-speed omni-directional running and jumping trajectories while mounted on a test rig.

This thesis introduces and develops GOAT, the **gearless omni-directional acceleration-vectoring** topology. GOAT is a novel 3-DOF, parallel 3-RSR leg topology with an optimized workspace

driven by an ultra low-impedance actuation scheme for precisely ‘feeling’ forces and dynamically reacting to the full 3D world around it. This 3-RSR topology expands the multi-modal mobility of dynamic legged robots beyond operating dynamically in the sagittal plane by enabling explosive omni-directional jumping, running, and dexterous crawling. The 3-RSR topology puts all 3 of its actuators in parallel to reduce torque requirements on any one actuator which allows the direct-drive and quasi-direct drive actuation scheme — which simplify the implementation of high fidelity virtual model control — to be used.

The 3-RSR leg is optimized for maximum kinematic workspace, force envelope, and energy delivery/absorption. It is mechanically designed using finite element analysis (FEA) to be robust and resilient to large 3D impact forces, pervasive in dynamic legged locomotion. Furthermore, the new leg topology is characterized with respect to multi-modal mobility, specifically 3D jumping via omni-directional force vectoring, as compared to conventional leg designs.

In addition to leg design and characterization I present an elaborate trade-off analysis and survey on actuator design principles for dynamic legged robots that achieve a balance of high torque density, high force transparency (i.e. low mechanical impedance) for high fidelity proprioceptive force control, and energy efficiency. By designing with control simplicity in mind, using a novel leg-topology with state-of-the-art actuators, I aim to conceive a new highly dynamic and agile robot capable of unprecedented 3D agility.

1.4 Thesis Outline

Chapter 2 of this thesis discusses design principles for engineers and researchers looking to understand and build agile legged machines. A comprehensive survey of existing robots is presented and the design trade-offs associated with competing goals in legged agility are discussed and clarified. The two high-level design paradigms discussed are selection, synthesis, and mechanical realization of leg topology and actuator design, selection, and low-level control for maximizing performance in the context of legged agility.

Chapter 3 introduces the novel GOAT leg, provides an explanation of the kinematics, presents several design optimizations to maximize workspace and force envelope, and details the mechanical design and finite element analysis for high force 6-axis loading. Chapter 3 then compares the GOAT 3-RSR leg topology to other existing 3-DoF leg topologies across several metrics important to legged robots and legged agility. The mechanical, electrical, and low-level control design of the dynamic direct-drive and quasi-direct-drive actuator modules are then presented. Chapter 3 concludes with a calibration and preliminary experimental results for the high fidelity impedance control of GOAT’s custom actuators.

Chapter 4 presents the control architecture for active virtual compliance in dynamic locomotion using proprioceptive force control. I provide an overview of important existing dynamic models and

control frameworks for compliant and dynamic legged locomotion including SLIP and the Raibert controller. The bulk of chapter 4 is concerned with describing the control algorithm used to achieve virtual compliance in the GOAT leg using a high fidelity impedance controller. Experimental high jumping and virtually compliant landing are performed and the results are analyzed and compared to other legged robots with jumping abilities.

Chapter 2

Design Principles for Dynamic Legged Robots

In this chapter I address the current state-of-art in dynamic legged machines and discuss the advantages, disadvantages, trade-offs and limitations of current leg designs and actuation schemes. This chapter serves to build and document the base of background knowledge that was used to conceive the design of the GOAT leg.

2.1 State of the Art in Dynamic Legged Robots

Extreme multi-modal mobility is for the most part still highly undeveloped. Existing robots that exhibit multi-modal mobility are the RHex [13], LittleDog [27], SandFlea [28], and MIT Cheetah robots [9]. RHex has demonstrated capable locomotion using simple mechanically compliant legs to passively conform to rugged terrains rather than explicitly planning footholds although this comes at the expense of reduced controllability. RHex has also shown dynamic jumping maneuvers although its 1-DoF sagittally constrained legs limit its capabilities in out-of-plane, 3D jumping [29]. LittleDog utilizes an alternative approach to traverse rugged terrains by explicitly planning center of mass trajectories and foot holds while relying on dexterous limbs to interact precisely with its well-perceived environment. LittleDog has also demonstrated dynamic leaping maneuvers but its high impedance actuators, slow leg swing speed, and leg topology complicate force control and ultimately limit the magnitude of its dynamic jumping and running capabilities. Although Boston Dynamics SandFlea employs wheels instead of legs it exhibits highly dynamic multi-modal mobility by driving over flat grounds and using compressed gas to launch itself up to 30 feet in the air to overcome obstacles. MIT Cheetah uses very low-impedance actuators to generate high speed and high force motions with excellent proprioceptive sensing but its dynamic mobility is constrained by its limited

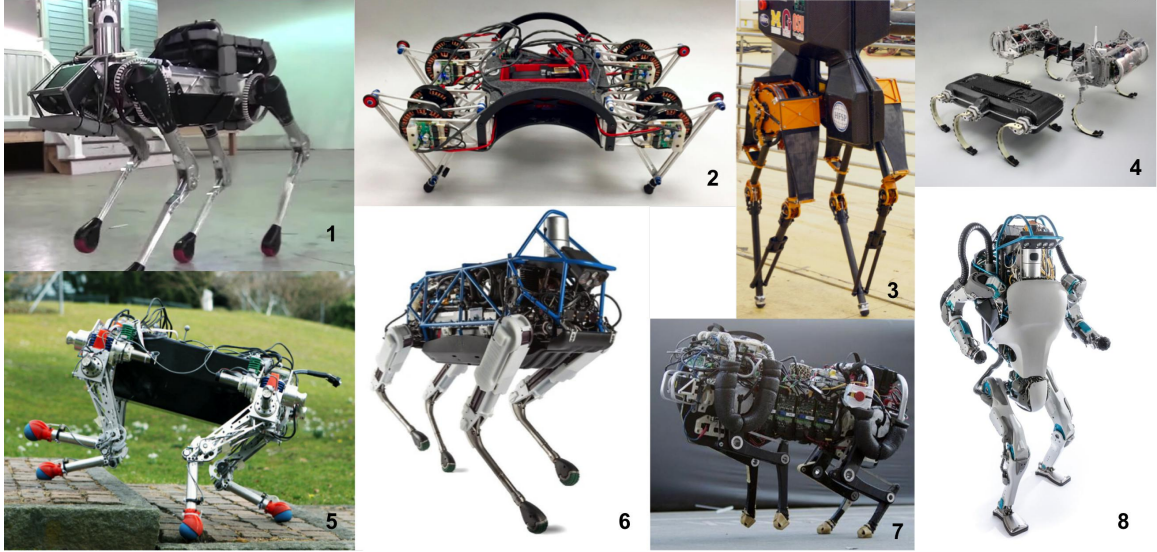


Figure 2.1: The current state of art in dynamic legged machines in 2016: 1) Boston Dynamics (BDI) SpotMini, 2) Penn/Ghost Robotics Minitaur, 3) ATRIAS, 4) RHex and Canid, 5) StarlETH, 6) BDI Spot, 7) MIT Cheetah, 8) BDI Atlas.

leg workspace to motions primarily focused in the sagittal plane [30][38]. MIT Cheetah’s leg design allows it to move impressively in the forward direction but severely restricts its ability to make tight turns, rapid direction changes, or run sideways and backwards. Additionally, many other robots have been designed to utilize multiple modes of mobility including flying, jumping, gliding, walking, rolling, and boating [32]–[36]. This thesis, however, will focus on a slightly different multi-modal mobility as defined by the use of limbs for both static and highly dynamic behaviors with the goal of traversing a much broader set of terrains more efficiently than current legged robots are capable of.

Therefore, an important challenge in designing legged robots with multi-modal mobility is the selection or synthesis of an appropriate leg topology and complimentary actuation scheme to drive the desired dynamic motions. The most prominent of the current state-of-art in legged robots, shown in Fig. 2.1, include Boston Dynamics’ Spot, SpotMini, BigDog, LS3, and Atlas [4][5][7]; HyQ [8]; the Raibert Hoppers [6]; MIT Cheetah [9], ATRIAS [10], StarlETH [11], Penn Minitaur [12], and RHex [29]. These robots share many similar design requirements including: efficient, high force/speed actuators; leg compliance (virtual or mechanical); robust mechanical structure and transmission; high control and proprioceptive sensing bandwidth; low impedance; low limb inertia; and leg topologies with a large workspace and force envelope.

Each of the aforementioned robots differ slightly in design prioritization which has lead to various combinations of actuation schemes and leg topologies shown in Figs. 2.2 and 2.6. Traditional leg topologies include prismatic (Raibert Hoppers, SCHAFT 2016 [16]), series-articulated (MIT

Cheetah, StarlETH, HyQ, SpotMini, Spot), redundant series-articulated (BigDog), 1-DOF motion generation linkage (Canid) [14], or 2-DOF parallel (ATRIAS¹, Penn Minitaur, MIT Super Mini Cheetah [15]).

Prismatic legs (Fig. 2.2) are simple and have the advantage of decoupling actuation for controlling leg angle and leg length separately. Open chain series-articulated legs also decouple actuators controlling leg length and leg angle, have a large workspace, good efficiency and high foot speeds. Redundant series-articulated legs have an even better workspace however, the distally located actuators increase limb inertia therefore, these joints are typically smaller and weaker than proximal joints [7]. Linkages with 1-DOF offer very simple control and very low limb inertia but consequently have a limited workspace typically prescribed to a single foot trajectory parameterized by a 1-DoF rotary input as done in [29].

Parallel mechanisms, such as the 3-RSR, are propitious because they

1. allow the large foot forces required for dynamic maneuvers to be distributed across several actuators with smaller gear reductions, thereby improving force transparency as compared to prismatic and series leg topologies;
2. can be synthesized with leg parameters that achieve a workspace larger than traditional parallel mechanisms that encloses the full running, jumping, and walking task space;
3. can have a very low limb inertia, and thus high speed limb, because actuators can be placed proximally in the hip.

Parallel linkages, however, typically suffer from a small workspace to mechanism-volume ratio and inefficiencies due to negative work caused by internal antagonistic work loops [10]. Fig. 2.2 and Table 3.2 provide a comparison of the common leg topologies used in today's dynamic legged machines.

The two most commonly used actuation strategies in legged robots are electro-hydraulic and electromechanical actuators. Hydraulics make use of the mechanical advantage from pressurized non-compressible fluids. These actuators offer good control bandwidth (≈ 35 Hz), superb force density, and structural robustness which come at the cost of high stiffness, poor force transparency/backdrivability, a limited joint space, poor energy efficiency (due to power system and fluid loss), and relatively large and heavy necessary infrastructure (hydraulic pressure unit (HPU), pumps, heat exchanger, IC engine, filters, accumulators, etc.) [8][11].

Conversely, electromechanical actuators are higher speed, more energy efficient, require less power-related infrastructure, and have a significantly larger joint space or range of motion. Electromechanical actuators can be made to have a high torque density with the use of a gearbox or transmission mechanism but this comes at the cost of N^2 reflected inertia (where N is the reduction ratio), decreased control bandwidth, and increased actuator impedance among other undesirable

¹ATRIAS legs have a total of 3 degrees of freedom. The sagittal plane consists of a planar 2-DOF, 5-bar linkage that's augmented with an abduction/adduction joint to allow for out-of-plane motions

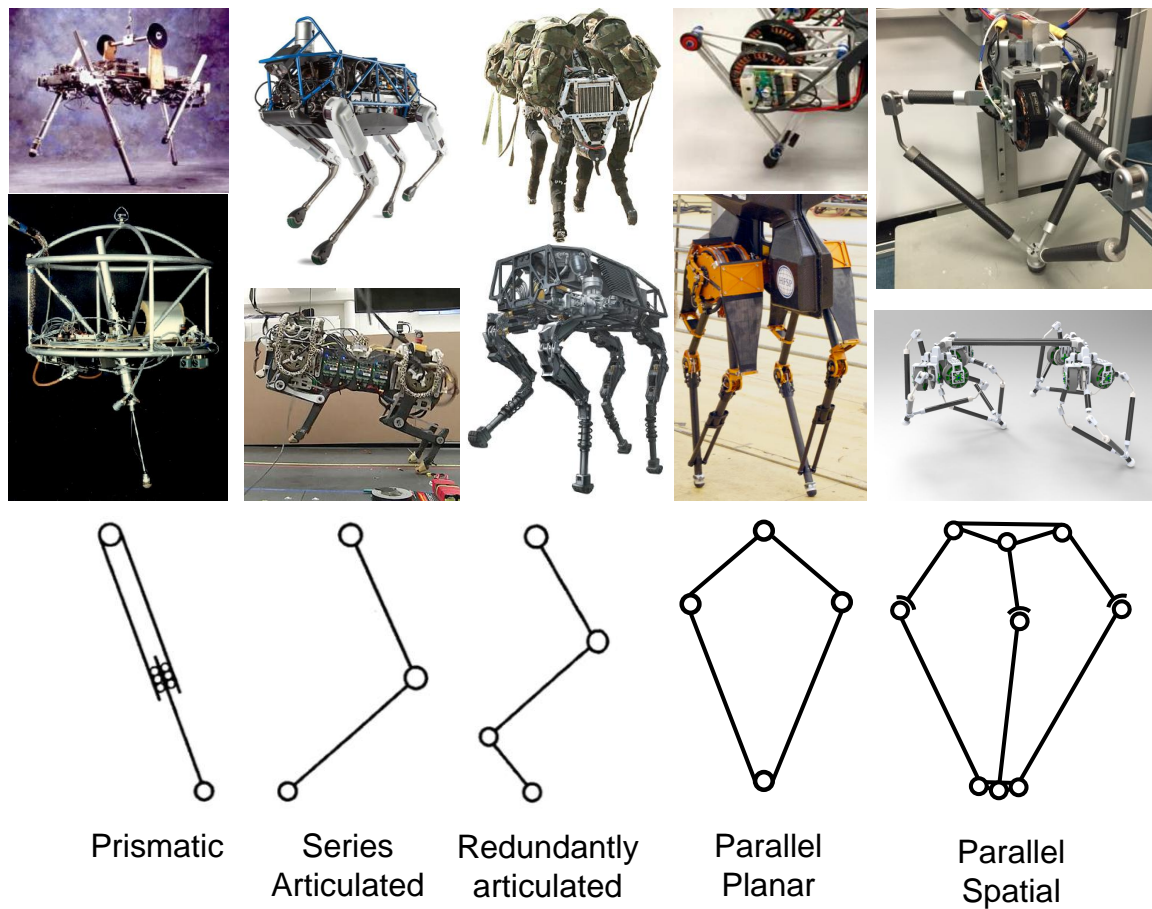


Figure 2.2: Common robot leg topologies. The robots shown from left to right include the Raibert quadruped/monopod [6], BDI Spot [2] and MIT Cheetah [9][38], Boston Dynamics Big Dog [7], Penn/Ghost Robotics Minitaur [12] and ATRIAS [10], the GOAT leg with a parallel spatial 3-RSR topology.

attributes in the context of force-control. Gearboxes are also susceptible to yield stress failures and tooth shearing under large impulse loading and impacts which are pervasive in dynamic legged locomotion.

Electromagnetic actuators can be configured as direct-drive (Minitaur), quasi-direct-drive (MIT Cheetah), series-elastic (ATRIAS, StarlETH, Snake Monster [23]), geared (potentially SpotMini), parallel-elastic, or variable stiffness (BiMASC [21], X-RHex [22]). Similarly pressure-based actuators can take the form of hydraulics (Wildcat, BigDog, LS3 [1.2]), electro-hydraulics (HyQ, Spot), pneumatics (original Raibert Hoppers), and hydrostatics. Recent developments in hydrostatic transmissions have combined quasi-direct-drive actuators with fluid transmission lines using pairs of rolling-diaphragm cylinders to form rotary hydraulic actuators [37]. Hydrostatic transmissions enable freedom in actuator placement to maintain low limb inertia while maintaining high force transparency and bandwidth [17]. Hydrostatics are however, currently limited in force production by the relatively low rated operating pressures of the rolling diaphragms (250 psi) as compared to hydraulic actuators which typically operate at around 3000 psi [37][8].

2.2 Leg Design Principles for Agility

Legged robots utilize a variety of leg topologies and actuation schemes to achieve dynamic mobility. In this section we will study the current state-of-art machines and highlight the areas in which these legged machines excel and are limited. We will focus on the design of the most prominent dynamic legged robots which include the MIT Cheetah, ATRIAS, Penn Minitaur, RHex, StarlETH, Boston Dynamics' Spot, and the original Raibert Hoppers. From this study we can extract principles of legged agility to be used in the design of future legged robots with greater mobility and real-world utility than exists today.

From the following analysis it will become evident that the design of these dynamic legged robots vary significantly yet a majority of their design requirements are shared. Common design requirements for agility include

1. High force, high speed legs
2. Passive or Active Compliance
3. Robust/Resilient leg mechanics and transmission
4. Energy efficient system

These design specifications lead to a number of implementations which make trade-offs based on various prioritizations of each specification. Many of these design specifications are inherently coupled, thus selecting actuation schemes and leg topologies to achieve a desired performance is non-trivial. For example, having high force and high speed legs could conflict with strong leg structure in that

high speed legs for a given set of actuators require a minimization of leg mass and leg inertia. By reducing leg mass, commonly through reduction of the structure's cross-section the yield stresses seen in the leg for a given impulse increases which ultimately reduces mechanical robustness and longevity of the machine as a whole. Similarly, an increase in proprioceptive force sensing fidelity may impede on the leg actuators torque density leading to a reduction in force production of the limb. Additionally, introducing mechanical compliance in the leg design to recycle gait energy from step to step by storing and re-delivering elastic energy hinders high frequency controllability of foot position and force. A basic analysis of these specifications yields three common trade-offs in design which many robots today exemplify and attempt to balance. These trade-offs are

- High torque density vs. low actuator impedance
- Energy Efficiency vs. controllability
- Dexterity vs. efficiency vs. agility

As these inherently coupled design specifications present numerous trade-offs they likewise present many opportunities for innovative designs which attempt to achieve an optimal balance of each requirement. The following subsections analyze the various design specifications and highlight the performance of robot's which prioritize each specification.

2.2.1 High Force, High Speed Legs

1. **High Torque Density Actuators:** In the context of dynamic legged robots, high force is typically considered on the order of 2 to 3 times the robot's body weight. This criteria matches that seen in leg force of human running which reach up to 3 times the body weight [38]. Other literature in legged robot design seem to agree upon a standard of 2 N-m per kilogram of body weight of required knee joint torque for running and disturbance recovery [39]. Similarly, high speed in the context of human/animal running and dynamic legged machines is considered to be at least 2 to 3 joint revolutions per second, corresponding to joint outputs of 180 rpm or 1080 deg/s [40]. With the requirement of both high speed and high force/torque for achieving dynamic behaviors, there is a imminent trade-off as transmissions usually accomplish one at the cost of the other. Therefore, in addition to torque density (defined as mass specific torque), power density (defined by bandwidth times torque density) is also an important performance metric to consider.

While power density is an important measure for legged robots in general, in direct-drive or quasi-direct-drive applications torque is the limiting resource in performance (as opposed to speed) and thus torque density is a more useful metric. Therefore, rather than maximizing power density, legged robots should focus on maximizing torque density or more specifically thermally specific torque density [12].

2. **Low leg mass and leg inertia:** By Newton’s second law acceleration is a function of both body mass and force applied to that mass. So in addition to maximizing torque density it is important to minimize mass and inertia. This is commonly achieved by using mechanisms which locate mass in regions closer to the body as opposed to distally on the leg. Additionally, to reduce leg mass and inertia, high strength-to-weight structural materials such as carbon fiber, aluminum, and titanium can be used. Present and future versions of HyQ and BDI Atlas are now beginning to utilize manufacturing processes that integrate hydraulic actuators and sealed fluid lines directly into the leg structure [41][42].

Running at high speeds and exerting foot forces quickly for explosive dynamic maneuvers requires a leg which must rotate and oscillate rapidly while switching direction throughout every duty cycle. This rapid and cyclic leg swinging requires constant rotational acceleration which is a heavy load on the actuators. Therefore instead of increasing actuator size which consequently increase robot size and total mass the leg design should be such that mass and inertia are minimized while maintaining structural integrity. The MIT Cheetah lowers leg mass and inertia by using a composite carbon-fiber leg and placing hip and knee actuators co-axially in the hip with a 4-bar linkage that extends from the knee actuator to the knee joint to transmit motion. Although the knee actuator is placed proximally in the hip and the contribution of the knee actuator’s mass on leg inertia is minimized the knee actuator mass is not decoupled from the leg inertia as the hip actuator is still required to rotate the mass of the knee actuator’s total mass (rotor and stator). Lowering limb inertia I is desirable because leg acceleration and swing speed can increase for a given set of actuators by $\tau = I\ddot{\theta}$ and inertial forces acting on the body generated by swinging appendages are decreased.

3. **Energy Delivery:** High force and high speed simultaneously implies high power and high energy delivery as $P = F * V$. Therefore, a leg topology with an adequate force map or force envelope, where the force map describes force production of the limb at each position in the limbs workspace, is desired for exerting large amounts of energy over short durations of time to induce jumping and fast running.
4. **Center of Mass located at or close to the hip:** By locating the majority of the legs mass at the hip, the designer of the robot affords the controller simplicity in being able to use simpler inverse dynamic models when developing motion planners. Additionally, if this principle is taken to the extreme as done in ATRIAS, where unsprung leg mass accounts for 5% of the total robot mass simple legged locomotion models such as SLIP and LIPM where leg mass is neglected can become accurate representations of the physical robot [10].

2.2.2 Passive or Active Compliance

While most agree that some degree of compliance is needed, there are currently two schools of thought in terms of achieving compliance in highly dynamic legged robots and there is no clear verdict on whether active or passive compliance trumps the other. While passive compliance utilizes passive dynamics to simplify control and recycle energy the compliance is mechanically ‘built-in’ and therefore cannot be removed when its convenient for the leg to be very stiff. Attempts at mechanically adjusting stiffness are typically complicated, prone to failure, and add system mass [21]. Conversely, active compliance uses motor control software to virtually mimic mechanical compliance. As such there is no physical elastic element to store and redeliver elastic energy and so the efficiency of purely active compliance is not as high as passively compliant systems. However, the efficiency of regenerative power electronics in converting negative mechanical work back into battery potential is improving and will allow active compliance implementations to become more efficient.

Other attempts to achieve compliance include parallel or series mechanical compliance in combination with virtual compliance to reap the benefits of each approach [43][10][11]. While this is an area of current and future research, control complexity for these systems is increased due to the need to accurately model passive dynamics in order to virtually augment the total system’s dynamics.

1. **Accurate, High Bandwidth, Force Sensing:** For active compliance to work effectively the compliance must operate at the kHz time scale which requires high control frequencies and accurate, high bandwidth, force sensing. To deliver virtual forces which emulate physical components such as springs and dampers force sensing is critical and methods for attaining such force control include SEAs, custom strain-based force sensors and load cells, and direct-drive. In addition to actuation and sensing strategies, leg topology plays a key role in proprioceptive force sensing. Therefore, it is important to conduct an analysis of proprioceptive sensitivity when using a motor-current based method of torque sensing and the leg Jacobian to measure foot forces. Additionally, all forces acting at the foot that must be measured accurately by motors located at proximal joints must first pass through the leg mechanism and structure which is susceptible to hindrance from mechanical impedance sources. Therefore, in addition to intelligent selection of leg topology and actuation scheme it is critically important for proprioceptive force sensing that mechanical impedance be minimized and eliminated wherever possible.

2. **Low mechanical impedance:**

Mechanical impedance ($\frac{F}{v}$) can be thought of as anything which impedes the transmission of actuator force from generating motion at the end-effector and vice-versa. Contributing factors of impedance include high mass, inertia, stiffness, dampening, and friction. Minimizing mechanical impedance is ideal for insulating the body from rapid motions of the foot during impact and for enabling high fidelity proprioceptive sensing necessary for high bandwidth

virtual model control. Therefore to maintain low mechanical impedance the actuator and transmission must be designed for high force transparency which can be synonymous with back-drivability. High force transparency enables accurate proprioceptive sensing which is necessary to implement high-bandwidth force control for active compliance while keeping distal leg mass at a minimum. Using motor current to sense actuator torque is advantageous to placing a stiff load cell or force sensor distally at the foot to measure end-effector interaction forces. This is because distal placement of sensors increases leg inertia and mass and also presents robustness issues as peak forces in running animals and robots reach 2.6 to 3 times the body weight which has presented challenges in robust sensor design that's capable of handling these cyclic high impact forces. To achieve low passive mechanical impedance the MIT Cheetah minimizes its transmission reduction ratio to a custom 5.8:1 single stage planetary gear [9]. Taking this specification to the limit for optimal proprioceptive sensing and force transparency requires direct-drive actuation as done with the Minitaur robot [12].

3. **Variable Leg Impedance** Another important feature is legged locomotion for dynamically stable gaits is the ability to modulate or adjust leg stiffness and leg impedance. This ability is an important to be able to tune on the fly for stability and efficiency purposes depending on locomotion speed and terrain stiffness [21]. Countless and often very creative mechanisms have been designed to achieve variable stiffness actuators and legs for mechanically compliant systems with passive mechanical springs [22][21]. These mechanisms tend however, to suffer from slower stiffness modulation rates and cause the overall leg to be larger and heavier which diminishes the return of having variable stiffness in a dynamic robot. The alternative approach is to mimic mechanical stiffness using virtual components to create virtual forces using the system's actuators. This method has the advantage of being able to modulate system impedance and stiffness at the kHz time scale and can generate stiffness over the entire range of the actuators performance. An interesting concept which is relatively unexplored is the combination of a mechanical spring in parallel with virtual compliance. This combination would afford the robot the ability to store gait energy via elastic deformation of the spring while using the high bandwidth actuators to modulate the **effective** stiffness of the combined parallel mechanical and virtual compliance [43]. This offers efficiency advantages over pure virtual compliance but comes at the cost of added mechanical and control complexity.

2.2.3 Robust/Resilient Mechanisms and Structure

1. High Specific Strength Materials:

Designing a leg mechanism to withstand high impact loads and forces more than 3 times the weight of the body is challenging. Even more challenging is designing the mechanism to withstand forces and moments applied about all 3-principles axes (i.e. omni-directional

loading). As a place to begin in design considerations, a designer should consider the use of materials with superior specific strength (strength-to-weight ratio) for the leg components which experience large cyclic loads. Some of these materials in order of increasing specific strength (in $\frac{kN-m}{kg}$) are aluminum (204), titanium (288), composite-reinforced plastic (785), fiber glass (1307), Vectran rope (2071), carbon fiber (2457), and Kevlar (2514). [45]. Using composite materials provides ultimate strength for a given mass but these advantages are gained at the compromise of added fabrication complexity and increased cost as traditional machining/fabrication methods cannot be used.

2. **Bio-tensegrity [9]:** One method of increasing leg robustness to high impact loading is to use tensegrity or 'bio-tensegrity' as coined by the MIT Cheetah developers. Tensegrity uses compression elements suspended within a 'web' of tension elements. In the MIT Cheetah the humerus and radius are composed of foam-core composite plastic and the foot is molded with an embedded webbing tendon that provides compliance and minimizes stress on the radius [9]. Bending stress is minimized in the leg structure by distributing tensile forces to the Kevlar tendons and allowing the main foam core composite leg segments to be loaded primarily in compression[9]. This design reduces leg mass and inertia without sacrificing leg strength [9].

2.2.4 Energy Efficiency

1. **Energy Regeneration:** Just as hybrid vehicles use regenerative power trains to convert kinetic energy back into potential chemical (battery) energy, the motor drivers and drive electronics of legged robots can be designed to do the same. By using the motor as a generator in segments of the gait where external work is being done on the system, the kinetic energy or motion of the system can be used to back-drive the motor which will cause current to be induced in the motor windings which can then be used to regeneratively charge the power supply by increase the voltage to it. This concept of energy regeneration switches the flow of power from the power supply or battery to the foot which is the case during positive work operation to power flow from the foot to the battery in which case external work is being done on the system. The MIT Cheetah has custom designed drive electronics which are capable of converting work done on the robot back into chemical potential energy in a battery [30]. Using their custom electronics the MIT Cheetah has been able to recover 63% of negative mechanical work to reach an unprecedented efficiency and total cost of transport of 0.5 which rivals legged animals of similar size and mass [30].
2. **Elastic Energy Storage:** Many legged robots utilize passive dynamics from mechanical springs and dampers integrated directly into the leg structure. While these mechanical springs offer control simplicity via inherent compliance and passive stability to unmodeled terrains, they also have the advantage of storing and redelivering energy from stride to stride. This

energy recycling can decrease actuator power demand, actuator mass, and energy consumption during each stride. Energy recycling of this form is achieved when the robot’s kinetic energy can be converted efficiently into elastic potential energy in an elastic element upon touch-down and during stance. This stored elastic potential can then be converted back to kinetic energy in the next stride as a delivered thrust force during lift-off. The Bow Leg Hopper and ATRIAS robot, each with spring-like legs, have experimentally demonstrated elastic storage of 2.3 J and 10.4 J of energy per stride equating to 75 and 68² percent stride efficiency, respectively [19][20][10]. This is in comparison to the MIT Cheetah’s 63% efficiency³ (i.e. recovered negative work) which is achieved by energy regeneration alone [30].

3. **Eliminate or Minimize Sources of Energy Loss:** Similarly, the drive electronics, actuators, and transmission should be designed such that power loss is minimized. The main sources of power loss are joule heating and friction. Joule heating is proportional to motor current I squared by $P_{loss} = I^2 R$, where R is the internal resistance of each winding. The MIT Cheetah claims to lose 76% of all input energy to Joule heating in the motor windings so reduction in current consumed will have a massive impact (I^2) on system energy lost as heat. Additionally, friction and stiction arising in bearings, joints, and transmission elements are not only an impedance source but are a source of energy loss. The use of high performance ball or roller bearings rather than bushings can drastically reduce joint friction.

Energy Efficiency is a critical element of legged robot design in that any practical robot with real-world utility must be able to maintain power and last throughout the duration of a mission. Mission lengths can be on the order of hours or days so the typical run times of untethered robots today from a few minutes to a couple hours will need to be improved upon considering the current state of energy densities in high performing Lithium Ion (Li-ion) and Lithium Polymer (LiPo) batteries.

With these principles of leg design considered, a new leg design that attempts to balance these specifications can be conceived. For the purpose of this thesis, the highest priorities in leg design are those which contribute to superior 3D agility and virtual compliance.

2.3 Actuation Principles for Agility and Virtual Compliance

Although there are many factors contributing to the realization of agility and virtual compliance in legged robots, the most significant factors – which an actuator designed for agility should optimize – are:

²68 percent is attained from approximately 28% energy recycling in the spring and 40% energy regeneration in the motors and power electronics [10].

³The MIT Cheetah is the most efficient *dynamic* legged robot that utilizes only electromechanical energy regeneration because it uses legs that have no mechanical compliance and thus reaps no benefits of elastic energy storage [30].

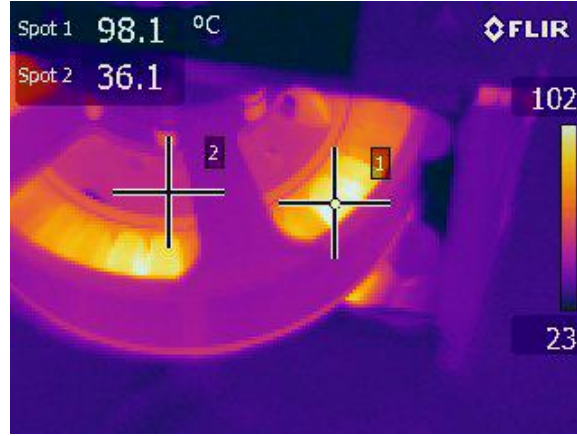


Figure 2.3: An infrared image of a motor winding captured by a Flir Thermal Camera. It is important to select a motor that not only has a high torque density but one that can sustain that torque over periods of time without overheating. The image shows temperatures higher than 100°C , therefore to prevent motor burnout thermal management is necessary.

1. Thermal Specific Torque Density [12]
2. Proprioceptive Sensing
3. Mechanical Robustness
4. Energy Efficiency

This section discusses each of the four specifications experimentally deemed as high-priority in the design of actuators for agile and actively compliant legged machines.

2.3.1 Thermal Specific Torque Density

Since specific torque is the first limiting resource in DD and QDD applications, to maximize speed, torque density, and proprioceptive force control the motor's geometrical and winding parameters should follow design principles which call for maximum thermal specific torque density defined in [12] as

$$K_{ts} := \frac{K_t}{m} \sqrt{\frac{1}{R_{th}R}} \quad (2.1)$$

where K_t is the torque constant ($\frac{\text{Nm}}{\text{A}}$), m is the motor mass (kg), R_{th} is the motor thermal resistance ($\frac{^{\circ}\text{C}}{\text{W}}$), and R is the winding electrical resistance (Ω). This measure describes a motor's ability to produce torque at stall while the windings dissipate energy through Joule heating corresponding to 100°C rise [12].

Parameters affecting thermal specific torque include motor geometry, winding configuration, pole configuration, and permanent magnet material.

Motor Geometry

Motor torque T_m is proportional to [46]

$$T_m = F \times R_{gap} \quad (2.2)$$

$$F = (\bar{B}\bar{A}) \times A_{RS} = (\bar{B}\bar{A}) \times (2\pi R_{gap}L) \quad (2.3)$$

$$T_m = 2\pi(\bar{B}\bar{A})R_{gap}^2L \quad (2.4)$$

where F is the tangential component of magnetic force generated by all the electromagnetic stator poles on the rotor, \bar{B} is the magnetic flux density (i.e the average magnitude of the radial flux density over the entire cylindrical surface of the rotor), \bar{A} is the specific electrical loading (i.e. the axial current per meter of circumference of the rotor), A_{RS} is the surface area of the rotor which contains the permanent magnet poles, R_{gap} is radial distance from the axle to the gap between the rotor and stator, and L is the axial length of the motor [46]. The magnetic force f_m for a single winding pole is defined by

$$f_m = Bli \quad (2.5)$$

where B is the magnetic flux density in (Wb/m²) or teslas, l is the length of the magnetic path (i.e. radial stator thickness or length of the stator tooth), and i is the current in one winding in Amps. The magnetic flux density and reluctance $\mathcal{R}(x)$ in Henry's (H⁻¹) are then defined by

$$B = \frac{\phi}{A} \quad (2.6)$$

$$\phi = \frac{\mathcal{F}_{mmf}}{\mathcal{R}} = \frac{Ni}{\mathcal{R}} \quad (2.7)$$

where \mathcal{F}_{mmf} is the magnetomotive force (MMF), N is the number of winding turns per stator pole/tooth, and ϕ is the magnetic flux.

The value of \bar{B} depends on the design of the motor's magnetic circuit which is constructed by the stator and rotor poles [46]. There are several competing parameters at play which lead to direct trade-offs and an opportunity for optimization[46]. It is desirable to maximize the cross-sectional area of the slots to maximize the amount of copper winding turns N . However, the trade-off for doing so forces the stator teeth to be thinner. Thinner stator teeth are undesirable because the cross-sectional area of the magnetic path will decrease causing an increase in magnetic reluctance \mathcal{R} seen by equation 2.8.

$$\mathcal{R}(x) = \mathcal{R}_{fe} + \mathcal{R}_{gap} = \frac{l}{\mu_r \mu_0 A_{tooth}} + \frac{x}{\mu_0 A_{gap}} \quad (2.8)$$

where μ_0 is the permeability of vacuum, equal to $4\pi \times 10^{-7} \text{H/m}$, μ_r is the relative magnetic permeability of the material, A_{tooth} is the cross-sectional area of the stator tooth about which the winding is coiled around, and x can be approximated as the perpendicular distance between the center of

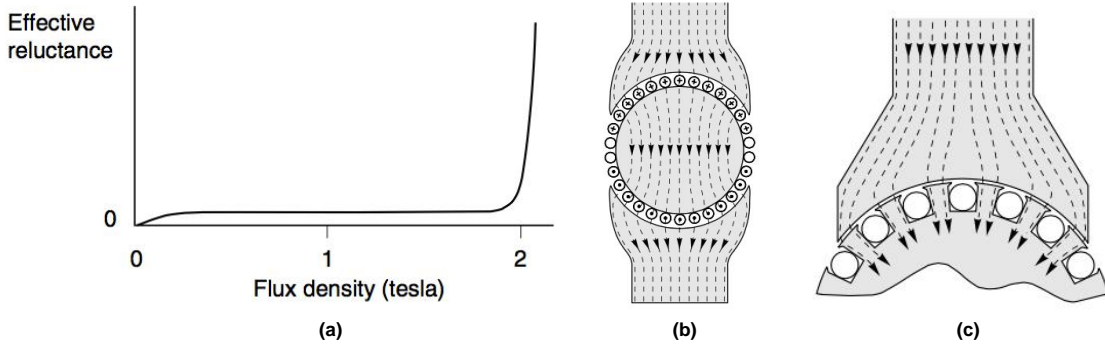


Figure 2.4: (a) Flux density in steel saturates at around 2 Tesla where flux densities any higher than 2 T produce rapidly increasing reluctance and the core loses ability to conduct flux. (b) Minimizing the air gap decreases magnetic reluctance which increases flux and flux density. (c) Using teeth and slots in the stator allows magnetic force on the winding coils to be transferred more effectively to rotor torque while reducing the air gap. Figure Source: [46].

the stator tooth and the center of the permanent magnet pole. A_{gap} is the cross sectional area of the air gap between the stator and the rotor.

Increasing reluctance will cause the magnetic flux in the stator teeth and iron core to saturate at a lower flux, thus limiting torque production as seen in Fig. 2.4 [46]. Similarly, increasing slot depth forces a decrease in the center region of the rotor which is responsible for transferring flux between adjacent poles, and thus increasing the reluctance of this portion of the magnetic circuit by decreasing the cross-sectional area will also lead to saturation at lower flux values [46]. Therefore, maximizing torque and torque density of brushless DC motors can be done by optimizing over the parameters of stator geometry and by intelligent material selection of the windings and core.

The value of \bar{A} plays an important role in motor design and is influenced by material properties of the core (iron/steel for higher flux) and the windings (copper for low resistance to current flow). \bar{A} can be increased by effectively sinking or removing heat from the windings to reduce heat losses and increase current capacity. The highest practical current density is typically between 2 and 8 $\frac{A}{mm^2}$ [46].

Additionally, from equation 2.4 a motor's torque is proportional to the volume of the rotor, $R_{gap}^2 L$ [46]. R_{gap} is **squared** in equation 2.4 because R_{gap} influences **two** parameters which are both linearly proportional to torque. The first contributing parameter is the moment arm R_{gap} at which the tangential component of the magnetic force is applied as seen in equation 2.2. The second contributing parameter is in the tangential component of the magnetic force⁴ which is dependent on the surface area of the rotor A_{RS} . A_{RS} is defined by the circumference of the rotor $2\pi R_{gap}$ multiplied by the rotor length L . Therefore from equation 2.3 the tangential component of the magnetic force is linearly related to the gap radius of the rotor. Since both the **tangential magnetic force** and the

⁴the component that acts to generate torque (not the radial component which pushes/pulls the rotor radially)

moment arm are linearly related to torque and multiplied together in equation 2.2 the influence of R_{gap} on torque is quadratic. This is in contrast to the axial length L of the rotor which is only linearly related to **tangential magnetic force** (and not moment arm) thus the influence of axial length on torque is only linear.

Rearranging equation 2.4 to

$$T_m = 2(\bar{B}\bar{A})(\pi R_{gap}^2 L) = 2(\bar{B}\bar{A})V \quad (2.9)$$

where V is the rotor volume indicates that volume specific torque is invariant of motor geometry [46]. This means that for a given rotor volume the torque production will be constant regardless of whether the rotor is short with a large radius or long with a small radius. While this is true mass specific torque (i.e. torque density) is not invariant to motor geometry because while mass scales linearly for both R_{gap} and L , torque scales quadratically with R_{gap} and linearly with L .

Assuming all other parameters held constant (stator thickness, axial length L , stator/rotor materials \bar{B} and \bar{A} , etc.), the torque density, T_d , or mass specific torque has the following relation:

$$T_d = \frac{T}{m} \sim \frac{V}{m} = \frac{2\pi L R_{gap}^2}{2\pi L R_{gap}} = R_{gap} \quad (2.10)$$

where torque density increases linearly with the motor's gap radius R_{gap} and is independent of it's axial length [9]. This relationship between torque density and R_{gap} is proven empirically in [9]. As the motor's gap radius R_{gap} increases the torque increases quadratically while motor mass increases only linearly indicating the torque density is linearly related to the gap radius (eq. 2.10). Mass only increases linearly because the majority of the motor mass lies in the stator windings which grows in mass in proportion to the motor's circumference, $2\pi R_{gap}$. Conversely, as the axial length of the motor increases, both the torque and motor mass increase linearly, indicating that torque density is not a function of axial length [9]. Therefore to maximize torque density in direct-drive applications a motor geometry with a large gap radius and short axial length should be chosen for a given actuator mass budget.

Although increasing gap radius benefits torque density, rotor inertia is also dependent on the gap or rotor radius by mR_{rotor}^2 . Therefore, a larger rotor inertia inhibits a motor's ability to accelerate which results in a longer mechanical time constant⁵ [50]. Increasing gap radius to achieve a desired torque has practical limits as legged robots typically have size constraints and interference with other components on the robot limit the actuators maximum radial size. Additionally, as axial length is reduced, a greater percent of the total coil on each stator tooth is consumed by copper wire which does not contribute to torque production.

⁵a motor's time constant is defined as the time required for rotor speed to reach 63% of the no load speed

Motor Core Design, Winding Configuration, and Permanent Magnet (PM) Rotor Poles

Additional design parameters which have influence on torque are the material and associated magnetic field strength of the permanent magnet as well as the winding configuration [46]. To maximize magnetic flux density (B) which is linearly related to torque production, strong rare-Earth neodymium magnets should be used. Neodymium magnets can have a magnetic field strength of 1.4 teslas as compared to ferrite or ceramic magnets which exhibit magnetic fields of 0.5 to 1 tesla [46].

Winding configuration is also influential on torque production as the windings are responsible for creating the magnetomotive force ($\mathcal{F}_{mmf} = Ni$) and thus magnetic flux (ϕ). From the equation for magnetomotive force and flux, a desired magnetic flux can be attained any practical combination of current and winding loops. Thicker wire can handle higher current but takes more space in the winding and thus can have less loops around a stator tooth. Conversely, thinner wire can handle less current but more loops can fit around a stator tooth with the same clearance.

Additionally, high current draw (thicker wires with lower resistance) requires expensive thermal dissipating infrastructure and considerations in heat sinking of the electronics and motor windings. High current also imposes constraints on the power supply that can be used (i.e. battery with high current discharge rates or super capacitors [48][49]). Thinner winding wires have higher electrical resistances and thus operate at higher supply voltages with a higher number of turns per pole and lower current ($V = IR$) for a given power rating ($P = IV$). Therefore, because motor torque is controlled by motor current ($\tau_m = k_m I$), motor's with thinner winding wire (higher resistance) and more turns have a higher specific torque than thicker wires (lower resistance) and less turns for a given total winding volume. Because voltage is cheap — meaning no additional infrastructure is needed to use higher voltages (to a limit) — and current is expensive, it is advantageous to use a higher supply voltage and lower current to achieve a given motor power [50].

Winding connections for brushless DC motors can be broken down into two types: wye and delta. Wye configurations are advantageous as the theoretical torque constant is greater by a factor of $\sqrt{3}$ (i.e. divide eq. 2.11 by $\sqrt{3}$ for delta connected winding phases) and does not suffer from the possibility of recirculating current if winding currents do not sum to zero as is the case for the Delta connection.

A brushless DC motor's torque constant k_m can be calculated by the first-order analysis presented in [47]

$$k_t = \frac{\tau}{I} = 2NBLR_{gap} \quad (2.11)$$

$$B_{eff} \approx B_m \frac{t}{t+g} \quad (2.12)$$

$$N = n_l n_a \quad (2.13)$$

where k_t is a function of the magnetic flux density B , the active length L , the gap radius R_{gap} , and the total number of active turns in the motor N [47].

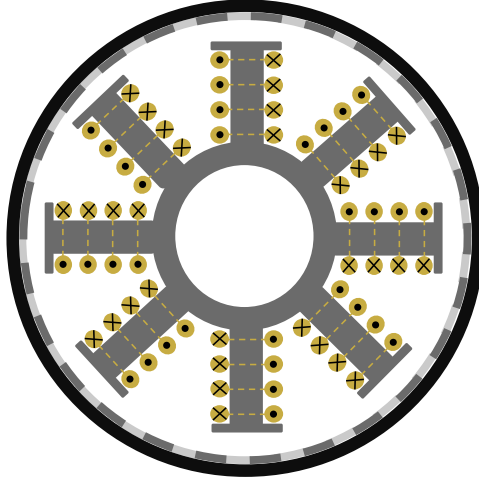


Figure 2.5: Simplified brushless DC motor cross-section. The copper winding coils are shown by the gold dots and x's indicating wire traveling out-of and into the page respectively. The dotted lines represent the end-turn segments of the coils which do not contribute to magnetic interaction forces.

The effective air gap magnetic flux density B_{eff} can be approximated by the flux density of the permanent magnets (1.4 T for neodymium magnets) multiplied by the ratio of magnet thickness t to the total effective air-gap which accounts for magnet thickness (t) and air gap (g) [47]. The active length L for a slotted stator is the length of the stator lamination stack. The active length does not include the length of end-turns (end-turns shown by dotted lines in Fig. 2.5)⁶ which do not contribute to the magnetic interaction force responsible for generating torque [47]. The torque contribution of the active length leads to another design trade-off analysis regarding the extra copper due to the end-effect of windings. As the axial length of a motor is decreased and gap radius is increased (to increase torque density as shown earlier) the percent of total copper winding wire length making up the ends of each loop of wire grows. This means that a larger percent of the copper in the windings does not contribute to torque production but adds ‘dead’ or ‘un-utilized’ mass to the motor.

Active turns are determined by the number turns (or coil loops) per pole n_l multiplied by the number of poles per energized phase n_a at any given time. In the case of 6-step commutation only 2 of the three phases are energized at a time so N would be 2 times the number of turns per pole times the number of poles per active phase [47].

Lithium polymer (LiPo) batteries offer high discharge rates indicated by a battery’s C-rating⁷. Thus, it is important to consider a motor’s current draw given the available selection of power sources for a particular application.

The electrical to mechanical power conversion of DC motors is described by

⁶an end turn is the length or portion of each loop of winding wire running perpendicular to the motor axle at the ends (front and back) of each stator tooth.

⁷A battery’s C-rating corresponds to the maximum safe discharge rate (Amps) for continuous and burst conditions which is found by multiplying the rated C value by the battery’s capacity in Amp-hours.

$$P_e = IV_s = IV_{emf} + I^2 R \quad (2.14)$$

$$P_m = \tau\omega + \text{friction_losses} \quad (2.15)$$

$$P_e = P_m \quad (2.16)$$

where IV_{emf} is the mechanical output power, IV_s is the electrical input power, and $I^2 R$ is the copper loss due to Joule heating. Therefore, as most motors use high-end ball bearings to couple the rotor to the stator, friction losses become negligible⁸ signifying the main source of energy loss is Joule heating.

Other motor characteristics worth consideration in motor selection are core vs. core-less motors. A motor with an iron core increases magnetic flux density, decreases air gap distance, and decreases eddy current losses for a given current. However, the trade-off for having a slotted or cored motor is higher cogging as compared to an iron-less core [47]. However, as the pole count and stator slot count increases, cogging and torque ripple⁹ effects decrease and torque production at low speeds increases. Another approach to reducing torque ripple is to arrange the rotor and stator poles in an 'allo-periodic' configuration [26]. In this configuration the motor is designed to have a different amount of rotor poles and stator slots to prevent all the rotor-stator poles from being aligned [26].

Three phase windings have been used traditionally because of simplicity and over time it has become the industry standard. However, using windings with an increased number of phases will reduce torque ripple further and increase motor efficiency [46]. Currently, a custom 8-phase brushless motor is being developed for the MIT Cheetah that will have significantly higher torque density, reduced torque ripple, and higher efficiency in the low-speed, high-torque operating regime as compared to COTS motors [51].

Field Oriented Control

In addition to motor geometry, the appropriate commutation and motor drive can increase torque output and decrease wasted energy and Joule heating. Using high frequency field-oriented control (FOC) or vector control commutation maximizes torque output at every electrical rotor angle which minimizes the effects of cogging and torque ripple effects [54]. FOC commutation also enables the motor to more efficiently and effectively produce torque over the entire range of operating speeds which includes producing large torques at zero speed and large torque at high speed. Section 3.5.3 provides a more in-depth description of FOC and the mathematical transformations used to implement this method of optimal brushless motor commutation.

⁸friction losses are negligible at low speeds until speeds approach the motor's no load speed

⁹Torque ripple is defined as the ratio of torque deviation to the average output torque. Ripple should be minimized because torque fluctuations prevent smooth motions at low speed.

Over-drive Methods for Performance Boost in Electromagnetic Actuators

Robots rely on high performance actuators to perform both static and dynamic maneuvers. As such its important to consider methods to safely extract as much performance as possible from each actuator. Brushless motor performance is thermally limiting. The continuous current rating and thermal limitations of motors are related directly to the windings' thermal insulation rating. For class F insulation the maximum permissible temperature rise from ambient is 100k.

The time t for a 100k temperature rise is

$$t = \frac{100k * C}{3 * I^2 R_e} \quad (2.17)$$

$$C = m_s c_{p,s} + m_c c_{p,c} \quad (2.18)$$

where C is the total heat capacity, m_s and m_c are the respective steel core and copper wire masses, $c_{p,s} = 460 \frac{J}{kg-K}$ and $c_{p,c} = 384 \frac{J}{kg-K}$ are the respective steel and copper mass specific heat capacity, and R_e is the electrical resistance of each winding phase [47]. The factor 3 accounts for heat produced by current running through all 3 phase windings. Therefore, this analysis shows yet another trade-off in which the time for 100k rise is proportional to total motor's heat capacity which itself is proportional to the total motor mass¹⁰ which suggests that adding mass will increase thermal performance.

In gear-motor (GM) applications the motor load is attenuated by the reduction ratio (n) of the gear-train, but in DD and QDD applications the continuous load on the motor is much higher which leads to overheating; thus, thermal management is needed [26]. To safely overdrive the motor while prevent winding burnout several methods can be employed [46].

One method employs a PID controller which uses a 2-resistor thermal model and feedback from a thermocouple mounted on the motor housing to estimate winding temperature and saturate current when the windings approach their thermal limits [48]. From the two-resistor model temperature can be solved for using the following equations taken from [48]

$$C_1 \frac{dT_1}{dt} = P - \frac{T_1 - T_2}{R_1} \quad (2.19)$$

$$C_2 \frac{dT_2}{dt} = \frac{T_1 - T_a}{R_2} \quad (2.20)$$

where C_1 is the thermal capacitance of the motor core, C_2 is the thermal capacitance of the motor housing, R_1 is the thermal resistance between the motor core and the motor housing, and R_2 is the resistance between the motor housing and the ambient air. T_a is the ambient temperature which is assumed to be constant, T_1 is the motor core temperature, T_2 is the motor housing temperature, and $P = I(V - K_v \omega)$ is the input power to the motor [48].

This online estimation of winding temperature allows the motor controller to fully exploit the

¹⁰assuming the materials used for the core and windings are steel and copper, respectively

motor's power envelope beyond the continuous current ratings.

An alternative method over-drives the motor temporarily at currents multiple times the max continuous current rating while monitoring the RMS current and ensuring that it does not exceed the max continuous current [9].

$$I_{RMS} = \sqrt{\frac{1}{T} \sum_{j=1}^f i_j^2 dt_j} \leq I_{cont} \quad (2.21)$$

where $T = \sum dt_j$ is the duty cycle period, dt_j is the time between each sample, and i_j is the current draw at time j . Rearranging this equation to solve for the next allowable current command which maintains an RMS current within the continuous current limit yields equation 2.22. If the present time step's current command is less than the max permissible current the motor controller will command that current; otherwise the motor controller will saturate the current command at the max permissible current calculated below.

$$[I_{j+1}]_{max} = \sqrt{\frac{1}{dt_{j+1}} \left(I_{cont}^2 T - \sum_{j=1}^f i_j^2 dt_j \right)} \quad (2.22)$$

Motor over-drive is an important consideration in legged robots where transient dynamics in running and jumping require large impulse forces with short duty cycles around 20% [9]. A motor's thermal time constant indicates the duration of time a motor can be over-driven safely, without overheating. Power of electric motors recommended by manufacturers are set by thermal failure limits and assumes no sensing of coil temperatures [9]. With a current controlled system, coil temperature can be estimated using thermal models and current can be limited by a PID controller to prevent demagnetization of the permanent magnets or more commonly winding damage caused by melting in the coil insulation (100° C rise). With a thermal model and within continuous current limits motors can generate much higher power than manufacturer ratings with a fixed voltage limit suggest. Typical rules of thumb suggest that at 2 and 3 times the continuous rated current, the motor can safely operate for a duration of 5 and 0.6 times the thermal time constant, respectively [50]. Other efforts to increase motor power by increasing the rate of heat dissipation include using passive finned heat sinks or active cooling by forced convection via fan or circulated fluids as done with the HRP3La-JSK robot in [49]. HRP3La-JSK uses custom high current (80 A continuous) motor drivers — powered by a large 100V, 13.5 F capacitor (8.9 kg) — which drive liquid cooled 200 W Maxon motors at a peak of 138 A (19 times the rated current of the motor) while maintaining winding and motor core temperatures within their 155 °C thermal limits [49]. Therefore, assuming the motors being used are thermally limited only and magnetic flux in the core is not saturating, the continuous torque of the motor can be increased by several times and enormous amounts of additional short-term power can be utilized from the motor by actively cooling it [49]. This of course comes with the cost of the added infrastructure needed to cool and circulate fluid through

all the motor sleeves.

Additionally, using FOC commutation ensures that while Joule heating from current is inevitable, the component of current which does not contribute to the production of torque will be eliminated. Therefore, all current used will contribute to generating torque, ensuring that for a given amount of joule heating, which is a function of current, motor torque will be maximized by eliminating wasted current.

2.3.2 Proprioceptive Actuation and Sensing

By now it is well understood that eliminating gear trains and transmissions from an actuator reduces mechanical impedance which results in increased force transparency and thus increased proprioceptive force sensing for superior force control [26][17]. However, this comes at the sacrifice of torque density which is the limiting resource in dynamic legged machines [12]. Therefore, alternative approaches have been taken to mitigate the nonlinear effects of gears through control.

One method is to use series-elastic actuators which decouples the gear train from the output load by a series-spring. This has the advantage of protecting the gears from large impulses and shock loading by temporary energy storage via spring deflection. SEAs also offer stable force control, energy storage, and mechanical compliance [21]. However, for actuation requiring high force bandwidth there is a fundamental trade-off when using a series-spring. As the spring stiffness is increased the actuator's control and sensing bandwidth is increased but the torque resolution and mechanical compliance decreases. Conversely, as the stiffness is decreased the spring acts as a mechanical low-pass filter on the actuation bandwidth, limiting the speed of force production [21]. This is shown experimentally in section 2.4.2 of this thesis.

Another alternative approach to torque sensing through a gear train and series-spring proposes to treat the motor as a velocity source rather than a torque source [52]. This has the advantage of using motor velocity ω_m , a parameter not affected by gear stiction and backlash, as a control target to regulate load torque τ_l using the following transfer function [52]:

$$\omega_m = \tau_l \left(\frac{1}{J_l s} + \frac{s}{k_s} \right) \quad (2.23)$$

where J_L is the inertia of the load and k_s is the stiffness of the series-elastic spring element [52]. In this approach gear dynamics between the motor and spring become irrelevant since the actuator's output velocity (after the transmission) corresponds directly to motor velocity which means the velocity loop automatically compensates for transmission losses without additional tuning [53].

Implementation of this method on legged robots may pose challenges, however, as estimating load inertia J_l is difficult because load dynamics vary with leg position and gait phase [53]. Schepelmann and Geyer propose a solution to this challenge by reformulating torque as a velocity-based controller. They do so by making motor position a function of motor velocity [52]

$$\tau_1 = -k_s(\theta_l - \theta_m) \quad (2.24)$$

$$\omega_m = \frac{\tau_l}{k_s s} + \theta_l s \quad (2.25)$$

where $(\theta_l - \theta_m)$ is the spring deflection, $\theta_m = \omega_m/s$, and the load inertia J_l is eliminated and does not need to be known because of the feed-forward compensation of eq. 2.25 [53].

2.3.3 Mechanical Robustness

Transmissions add yet another layer of complexity and components which make an actuator susceptible to additional failure modes. Gears must be rated for high impact loads which are pervasive in jumping and running robots. For gears to be robust in the application of legged machines they must be capable of handling these large impulses and short duty cycles which typically means they must be thicker, have larger teeth, higher friction and higher backlash all of which result in added weight and undesirable control complexities [17]. This is not an issue in direct-drive applications where large impulses are transmitted through the leg structure and into the body frame through the air gap of the motor¹¹. However, it is not always possible to completely remove transmission mechanisms and use direct drive for a plethora of reasons. Transmission mechanisms capable of withstanding high impulse load without failing are friction drives and v-belt drives. These transmissions may slip but will prevent failure or damage to the transmission. Other efforts to mitigate the issues of transmission robustness include the use of series-elastic actuators (SEAs). SEAs can protect the gear train by passively absorbing large, high frequency, impulses from ground contact during running and jumping by elastic spring deformation and energy storage. This is another contributing factor in understanding why legged robots like ATRIAS and StarLETH use series-elastic actuators and series compliance [10][11].

While transmissions are susceptible to mechanical failure under large loads, another trade-off becomes apparent when considering that direct-drive motors are susceptible to overheating under high continuous current/torque loading. This source of failure in DD actuators can be mitigated by the use of a reduction transmission such that the load applied to the motor is decreased by a factor of the reduction n .

2.3.4 Energy Efficiency

For direct-drive actuators to generate sufficient torque in legged robots the motors must operate in the high torque, low speed regime whereas an electromagnetic motor has peak electrical to mechanical power conversion efficiency in the low torque, high speed regime (near the no load speed) [50]. Therefore, the production of high torques at low speed requires high current as torque is directly

¹¹In direct-drive it is assumed that the rotor is coupled to the leg and stator is fixed to the body and forces are transferred from rotor to stator through the motor bearing and air gap

proportional to motor current ($\tau = k_t i$) through the torque constant k_t . Joule heating expressed as, $I^2 R$, is the dominant source of energy loss in this operating regime and in electrically actuated direct-drive legged robot systems in general. Therefore, by using a single stage transmission the motor can produce the same torques using a fraction of the current thereby reducing Joule heating losses quadratically. To this end, we argue for energy efficiency purposes that a savings of $\mu I^2 R$ power, where μ is the percent decrease in current, I , required to produce a given torque, is worth the $\approx 3-5\%$ transmission losses and the nearly-negligible added control complexity of a single stage planetary gear train. Section 2.4.2 of this thesis experimentally validates the positive performance of QDD actuators. Similarly, the quasi-direct-drive approach is used in the MIT Cheetah where a custom 5.8:1 planetary gear reduction is used and proprioceptive torque sensing is maintained to less than 5% error [30].

Summary

By selecting and designing actuators using these principles the torque density of a DD or QDD motor can be greatly improved to meet the needs of dynamic legged machines as demonstrated in [12]. Additionally, intelligent choice of leg topology can harness the actuator's torque more effectively, thereby enabling the use of DD or QDD actuation paradigms by reducing the torque requirements of each actuator while maintaining low actuator impedance and inertia. Specifically, a leg topology, such as the 3-RSR, which combines actuators in parallel minimizes actuator effort by distributing foot loads across multiple actuators. Therefore, the QDD paradigm is best suited with a parallel topology for achieving high end-effector force vectoring and high fidelity proprioceptive force sensing.

2.4 Actuator Comparison

2.4.1 DD v. QDD v. GM v. SEA

This section surveys and elaborates on actuator design principles for dynamic legged robots which attempt to achieve an optimal balance of torque density, force transparency, mechanical robustness, and energy efficiency. The advantages and disadvantages of direct-drive (DD), quasi-direct-drive (QDD), gear motors (GM), and series-elastic actuators (SEAs) are compared with respect to dynamic performance and agility in legged robots. A web graph, Fig. 2.6, is used to graphically highlight the strengths and weaknesses of each actuator type with respect to five types of robots: 1) Dynamic Legged Robots, 2) Human-Robot Interaction, 3) Industrial or Manufacturing Robots, 4) Aerial robots/drone, and 5) wheeled robots. An optimal actuator for a specific application can theoretically be chosen by maximizing the enclosed area by the polygon in the weighted web graph.

As the following actuator analysis will show, Direct-drive and *quasi* direct-drive actuation offers

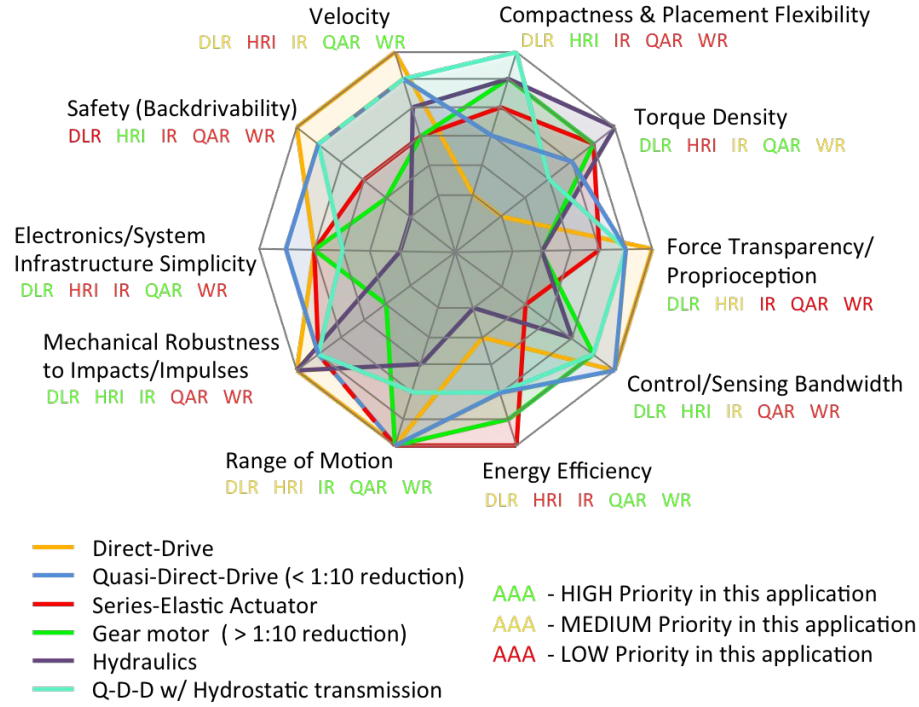


Figure 2.6: Comparison of actuation strategies with respect to meeting the requirements of various robot applications including: Dynamic Legged Robots (DLR), Human-Robot Interaction (HRI), Industrial Robots (IR), Quadrotors/Aerial Robots (QAR), and Wheeled Robots (WR). An optimal actuator could be determined by maximizing the area enclosed by the polygon of a weighted web graph.

several benefits as compared to geared or series-elastic counterparts with respect to the performance and control of dynamic legged machines. These benefits include high force transparency (low impedance), mechanical robustness to large impacts, and high force control bandwidth. Using direct-drive actuators also presents a few disadvantages which include drastically lower thermal specific torques and lower operating efficiencies during high torque motions [26].

Gearmotor (GM)

While augmenting an actuator with a gearbox can increase the actuator's torque density by orders of magnitude it does so at the cost of added control complexities, increased reflected inertia, efficiency losses and reduced mechanical robustness [26]. Control complexities are derived from the difficulty in modeling the non-linearities associated with backlash, internal stresses, coulomb and viscous friction, and stiction in the gear train — all of which hinder current-based torque sensing. These non-linear effects 'hide' forces acting at the output from being sensed by the motor causing motor current to be a poor indicator of output torque. Only in specific circumstances — when the load and the rate

of change of the load are in the same direction, and the output velocity is above a certain threshold and is not changing sign — was current sensing observed to be a reliable indicator of output torque on actuators with high gear reductions [55]. The poor motor-current based sensing of gearmotors is attributed to backlash — which occurs when there is a change in the sign of velocity — and static friction, which is prevalent when velocity is near zero.

By using higher-end more complex gear trains, backlash can be nearly eliminated and the number of stages can decrease to one. Harmonic gears offer zero backlash, a lightweight and compact form factor, and have the greatest torque density per stage but their high reduction ratios introduce large reflected inertias. Similarly, cycloidal drives offer high gear reduction ratios (high reflected inertia) in a small form factor with good shock overload capacity but are difficult to manufacture¹², suffer from poor back-drivability (transparency) and lower efficiencies ($\approx 75\text{-}85\%$ per stage) due to high sliding contact [50].

Friction, stiction and reflected inertia in transmissions increase an actuator's mechanical impedance and decrease total system bandwidth [17]. In order to track and command faster force trajectories, the closed-loop bandwidth must be increased by both the actuator and leg design. Therefore, a high transparency and highly backdrivable actuator — where all force at the output can be sensed at the input — is optimal for high fidelity and thus high bandwidth proprioceptive force control [17]. High fidelity proprioceptive force control is desirable for the the control of dynamic legged machines because it is necessary for effectively producing virtual leg compliance upon impacts and can be a very high-bandwidth indicator of gait state transitions (i.e. flight to stance phase). The effect of the transmission ratio n and its corresponding reflected inertia on system bandwidth is theoretically quantified for a simple 1-DoF actuator shown in Fig. 2.7(b) using equations 2.34-2.35. In this analysis of actuator bandwidth, k_s the series stiffness, can be set to 10^6 N-m for stiff gear trains and transmissions without an elastic element.

In addition to the effect gear reductions have on reducing bandwidth, transmissions also undesirably increase inertia. For any mechanical system with a reduction transmission, the effective mass moment of inertia seen by the input motor for a given output load with inertia I_l is derived by a conservation of energy formulation done in [57]. For a loss-less, ideal gearbox (i.e. negligent internal gear inertia) at steady-state

$$\tau_{in}\omega_{in} = \tau_{out}\omega_{out} \quad (2.26)$$

where a reduction gearing would increase torque and decrease speed such that

$$\omega_{out} = \frac{1}{n} \omega_{in} \quad (2.27)$$

$$\tau_{out} = n\tau_{in} \quad (2.28)$$

Solving for the required output torque by Newton's 2nd law gives

¹² manufacturing of cycloidal drivers are difficult due to very tight tolerances required for the cams

$$\tau_{out} = I_l \dot{\omega}_{out} \quad (2.29)$$

Plugging in equations 2.27 and 2.28 into 2.29 the effective inertia becomes

$$n \tau_{in} = \frac{1}{n} I_l \dot{\omega}_{in} \quad (2.30)$$

$$\tau_{in} = \frac{1}{n^2} I_l \dot{\omega}_{in} \quad (2.31)$$

Therefore, as seen from the motor input, the load accelerates in response to the input torque as if the gearbox had been replaced with an output link with a moment of inertia equal to $\frac{I_l}{n^2}$ [57]. This increased effective moment of inertia due to the transmission is referred to as reflected inertia and it scales by n^2 .

Gears are also inherently prone to being damaged by large impulses which cause tooth shearing. This is especially true in spur gear trains where the impulse load and impact force is being transferred over one to two gear teeth as opposed to planetary gears which distribute the load over multiple planet gears and thus multiple teeth. Because the cross sectional area of a single tooth is very small the shear stress defined by

$$\tau_{shear} = \frac{F_{impact}}{A_{c/s}} \quad (2.32)$$

becomes very large for even relatively moderate forces and thus heavy, high strength materials, such as hardened steel are usually required for high torque applications.

Series Elastic Actuators

In the mid 1990's Gill Pratt introduced a concept in which a mechanically compliant or 'elastic' element was configured in series with the motor shaft and transmission output. He coined this configuration a Series-Elastic Actuator (SEA) [58]. Since then many robots, both for manipulation and legged locomotion, have implemented custom SEAs. A few notable robots utilizing SEAs include StarlETH, ATRIAS, NASA JSC's Valkyrie [59], Rethink Robotics' Baxter, and the CMU Biorobotics SEA-Snake [24].

Series-elastic actuators have been further developed to mitigate negative gear train effects and regain torque sensing accuracy while maintaining torque density offered by the gear train. SEAs also offer improved efficiency and mechanical robustness by using elastic energy storage via spring deflection to passively dampen impulse energy at the actuator's output from reaching the gear train or for recycling energy from step-to-step in gaits cycles. However, as a consequence, SEAs mechanically filter out high frequency dynamics and thus actuation bandwidth is inherently reduced as shown in Fig. 2.8 by the following analysis described by the model in Fig. 2.7(a).

SEAs employ a variety of spring elements with attempts at maximizing spring linearity, energy storage, specific energy, passive compliance, or torque sensitivity [24]. Common materials used as

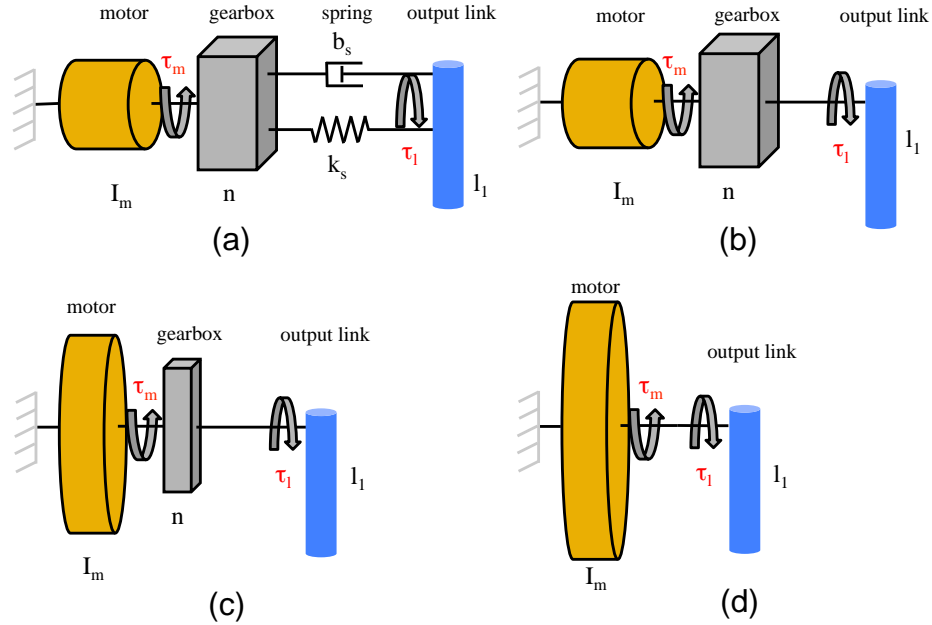


Figure 2.7: (a) Model of a series elastic actuator with series spring stiffness k_s , spring dampening b_s , gear reduction n , and motor rotor inertia I_m , (b) is a model of a stiff gear motor, (c) is a model of a quasi-direct-drive actuator, (d) is a model of a direct-drive actuator. τ_m and τ_l are the motor and load torques for a fixed input and output.

the mechanically elastic element include rubber, fiberglass, and steel in torsional, linear, leaf, and compliant mechanism configurations [24].

A big application of SEAs is in the use of robots that require force control to interact precisely with the environment and with nearby humans. A big advantage of SEAs is that they can offer torque sensing on heavily geared motors that is far more accurate than motor-current based methods. Torque sensing using SEAs is accomplished with Hooke's law. This requires using some form of an encoder to measure spring deflection θ with knowledge of the spring constant k_s

$$\tau = k_s \theta \quad (2.33)$$

Additional benefits of SEAs are the elastic strain energy storage and delivery capabilities, decreased reflected inertia for high reduction transmissions, and inherent shock energy absorption to protect the gear train from large impulses.

Energy storage and increased mechanical robustness are perhaps most advantageous for hopping robots which cyclically store energy in the series-spring upon touch-down impacts and re-deliver it as thrust energy for take-off in the following cycle. This energy recycling has benefits in energy efficiency as less input energy is required from the robot's actuators in each cycle. For example, ATRIAS stores around 40 J of energy by in each of its 3500 Nm/rad springs during stance of a slow

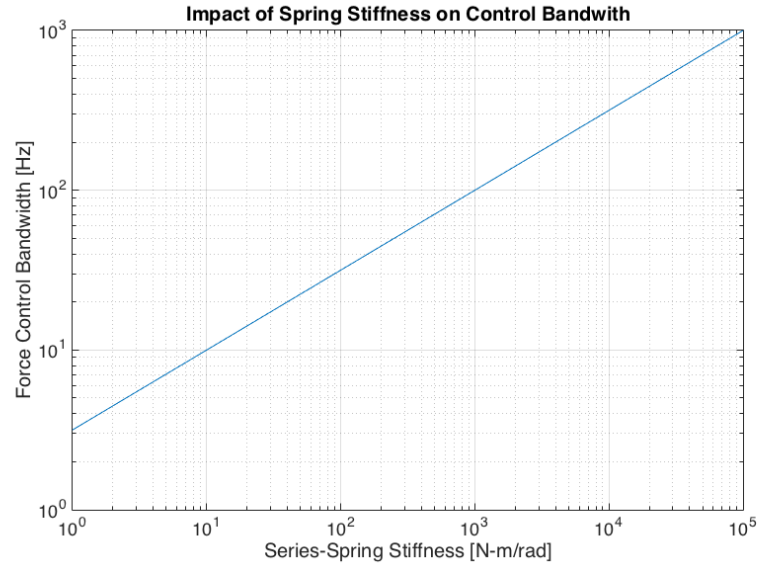


Figure 2.8: Impact of spring stiffness on control bandwidth for series elastic actuators.

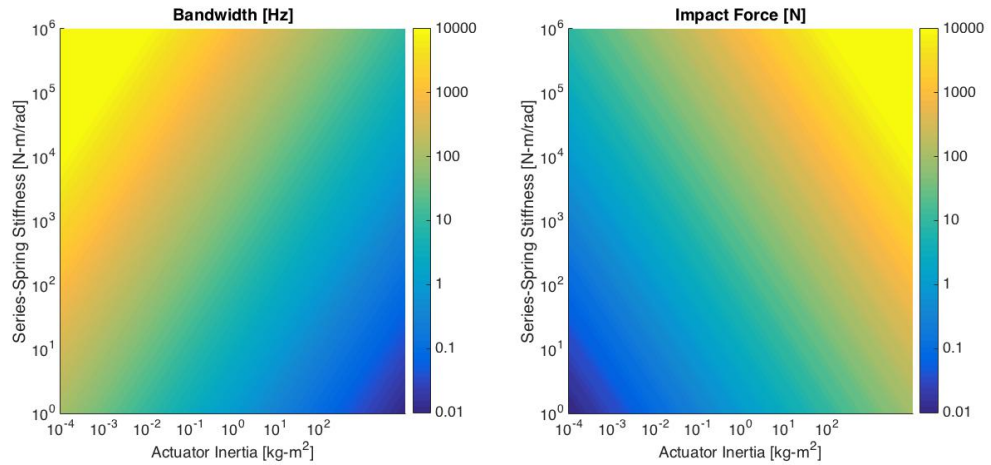


Figure 2.9: Relationship between actuator inertia and spring stiffness on control bandwidth and impact force.

running gait [10]. This corresponds to a 0.15 radian max spring deflection for that particular gait. Furthermore, smaller power requirements allow actuators to be sized smaller and thus reduce robot weight and payload.

While SEAs offer stable proprioceptive force sensing, enhanced mechanical robustness and impact mitigation, passive disturbance rejection, reduced impedance, and compliant position control they do so at the cost of increased control complexity. The increased complexity arises from the need to model compliance accurately for inverse dynamics and torque control.

The series-spring is a second order mechanical low-pass filter on high frequency dynamics. Thus, the spring dampens high frequency impacts upon foot touch-down which can be desirable but it is also responsible for a reduction in actuation bandwidth which is critical for very dynamic machines attempting to produce transfer force rapidly. The stiffness of the series-spring determines the maximum frequencies to which the actuator can command force and position trajectories. Using a simple SEA model, the theoretical bandwidth can be determined by finding the natural frequency of the system dynamics. The bandwidth of the actuator is a function of the transmission's reduction ratio n , the spring stiffness k_s , and the motor's rotor inertia I_m represented by

$$\omega_n = B = \sqrt{\frac{k_s}{n^2 I_m}} \quad (2.34)$$

Similarly, the impact force felt by the actuator is

$$F_{impact} = \sqrt{(k_s + k_g)n^2 I_m} \quad (2.35)$$

where k_g is the effective stiffness of the contact point in the environment [17].

Direct-Drive and Quasi-Direct-Drive

Using a larger direct-drive actuator to achieve a required torque without gear reduction increases the volume and weight of the actuator as compared to geared counterparts but it preserves the high transparency and low impedance that are crucial to high bandwidth proprioceptive force control. Additionally, the mechanical robustness and structural integrity of direct-drive systems are higher as compared to geared systems because there are fewer components to protect from large impulses ubiquitous in running, jumping and landing behaviors [26][12].

For a direct-drive system, the impulse forces at the foot are transmitted to the body through the leg Jacobian directly through the motors air gap [12]. This minimizes components in the load path that are susceptible to failure making for a more robust and resilient machine.

Should a transmission stage be used to achieve the required application torque I argue and show in the following analysis and experimental actuator comparison that an ideal actuator configuration for high speed running and jumping robots when considering efficiency is a single-stage planetary gear train with a reduction of at most 1:10. Single-stage planetary gears with reductions greater than 1:10 are not possible because pinion (sun) gears can only be made so small and as the reduction



Figure 2.10: The ideal configuration for maximizing reduction of a single-stage planetary gear is to fix the ring gear, couple the sun gear to the motor input, and the planet carrier to the output. Circles represent the gear's pitch radius so teeth are not shown.

ratio increases for a given ring size the sun gear pitch radius decreases and the planet gear pitch radii increase [60]. This leads to a design trade-off in which high reduction ratios produce higher torque outputs but as higher ratios are designed less planet gears can geometrically fit without interference, meaning impulse loads are distributed over less planet gears (and less individual gear teeth) which decreases overall resiliency/robustness of the gear-train. Planetaries with lower reduction ratios can have 4 to 5 planet gears for improved load rating while higher reductions of 1:10 can only have 2 planet gears. Other gear trains such as a harmonic and cycloidal drives, with a typical reduction of 1:100, will have reflected joint inertias ($\frac{I}{N^2}$) that approach the inertia of the robot's mass [21]. I refer to this actuator design as *quasi*-direct-drive (QDD) for its proximity to properties of true direct-drive systems. Quasi-direct-drive actuators preserve force transparency for accurate proprioceptive sensing while offering torque magnification for only marginal sacrifices in added impedance, reflected inertia and mechanical robustness. Planetary gears are compact, low profile, low weight, low cost, backdrivable, distribute loads over multiple planet gears (30-50% greater load capacity than spur gears), have minimal backlash (typically less than 13 arc-min or 0.21°), and high efficiencies (≈ 95 -97% per stage), while offering reduction ratios up to 10:1 for a single stage.

2.4.2 Experimental Validation of Actuator Properties

To experimentally verify the results of the theoretical analysis and comparison of DD, QDD, GM, and SEA actuators a series of experiments was conducted. The experimental force bandwidth, rise time, settling time, peak time, overshoot, and proprioceptive torque sensing accuracy and error are

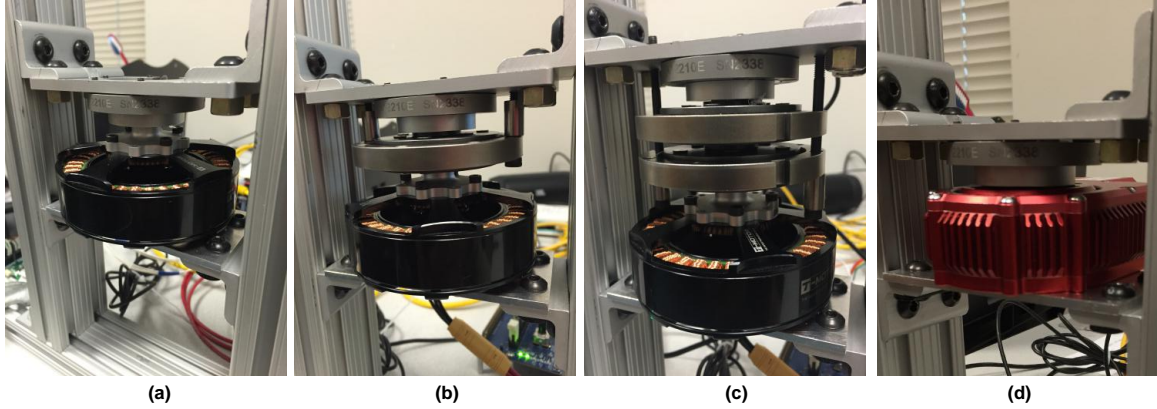


Figure 2.11: Actuators configured as (a) Direct drive, (b) quasi-direct-drive (1-stage planetary), (c) gear motor (2-stage planetary), and (d) Hebi X-5 SEA module in the torque testing rig. The motor back is fixed directly to a mounting plate and the output of the actuator is coupled to the 1-axis load cell whose housing is also bolted to the rig.

calculated and shown by the following plots in Fig. 2.12-2.16.

Fig. 2.11 shows the test rig used to conduct all the experiments whose results are shown in Table 2.4.2. The DD actuator is a T-motor U10 with no transmission. Single planetary gear stages were added to the direct-drive T-motor to test QDD (1 added stage) and GM (2 added stages). Each added gear stage is a COTS Matex 75-7MLD (7:1) planetary gear. Rather than arduously designing a custom SEA for the sole purpose of this testing, an available COTS SEA (Hebi X5-1 module) was chosen to match the continuous torque rating of the DD actuator. Therefore, For DD, QDD, and GM a T-motor U10 was the driving motor, while a much smaller Maxon EC-Max 16, 5W motor with a 272:1 gear reduction was used in the SEA. The different motor's have an effect on system inertia but the bandwidth trends validated in this test hold true regardless of the fact that different motors were used. All tests on all four actuators were done on the same test rig using a single axis SRI M2210E torque load cell.

Bandwidth

Each of the actuators was tested by commanding sinusoidal torque trajectories of increasing frequency until the actuator could no longer following the trajectory with adequate accuracy. The sinusoidal torque frequencies ranged from 1 Hz to the 100 Hz. The following bandwidth plots for each actuator show (a) a stable frequency, (c) max frequency with adequate trajectory following or actuator bandwidth, and (b) a frequency in between. For reference and comparison purposes, the MIT Cheetah (QDD), HyQ (hydraulic), and StarLETH (SEA) actuators have maximum force control bandwidths of 103 Hz [9], 15-20 Hz [8], 11-28 Hz, and [11]. Humans and animals on the other hand have a control bandwidth of only 4-8 Hz which implies that the majority of the dynamics in

running and jumping occur passively in muscles and tendons [21].

The direct drive actuator in Fig. 2.12 shows frequencies of 20, 70 and 100 Hz. The DD actuator was capable of following torque trajectories with an amplitude of 1.5 N-m accurately up to 70 Hz although at 70 Hz there is nearly a 180° phase while the torque amplitude remains accurate. The direct drive actuator demonstrated a bandwidth of up to 250 Hz for small, same-sign, torque variations on the order of 0.1 to 0.5 N-m in Fig. 4.6. The quasi-direct-drive actuator in Fig. 2.13 shows response at 20, 30, and 40 Hz. A phase offset close to 180° can be seen at 20 Hz but the actuator is still able to exert torque at commanded amplitude at 20 Hz and higher frequencies without significant loss of fidelity in torque profile or shape response. The maximum achievable frequency with adequate trajectory following for the QDD was determined to be 40 Hz, therefore this is the systems force bandwidth. The gear motor in Fig. 2.14 shows tests of 10, 20, and 40 Hz. While the trajectory amplitude is not followed very closely the frequency is maintained up to nearly 40 Hz. However, 40 Hz should not be considered as the system bandwidth because the torque amplitude has significant error over 100%. This can be due to the gear-trains relatively large backlash attenuating over 2 stages. The backlash was significant enough such that the motor could actually spin $\pm 360^\circ$ when coupled to the load cell which would not allow for any motion if the actuator had zero backlash. Comparatively, in the QDD actuator the input motor rotor was able to rotate about $\pm 45^\circ$ which is also relatively significant. The DD actuator was not able to rotate at all which makes sense as there is zero backlash as the rotor is directly bolted to the load cell without any transmission where backlash can accrue. Therefore, the system bandwidth for this particular gear motor (GM) actuator is approximated at around 25-30 Hz. The final actuator tested was the series elastic actuator which is a Hebi Robotics X5-1 module which uses a series-spring with 70Nm/rad stiffness, a 272:1 spur gear reduction over 3 stages and is manufacturer rated at 0.25° of backlash. Fig. 2.15 shows that the Hebi X5-1 module is rather accurate in tracking torque trajectories by measuring the spring deformation of their natural rubber series-springs. The response begins to diminish in amplitude tracking at around 25 Hz and reaches a phase offset of 180° at 30 Hz. Therefore, the experimentally determined bandwidth of the system is approximated at 25-30Hz.

Thus, it is clear that direct-drive is far superior nearly doubling the bandwidth of the alternative actuator configurations. However, since a stock, COTS, Matex planetary gear is used with a significant 1.2° rated backlash, the bandwidth can reasonably be expected to be lower than that of an actuator using a custom, application-optimized, planetary gear designed to minimize backlash, maximize load rating, and minimize weight as done in [9]. Since budget was a factor in these experiments these cheap \$75 gear trains were sufficient to understanding the general influence gear trains had on actuator bandwidth.

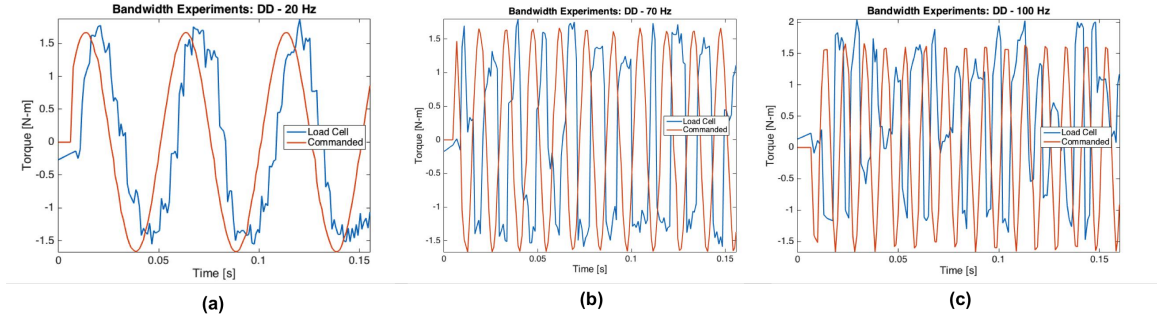


Figure 2.12: Experimental torque bandwidth testing for a direct-drive T-motor commanded sinusoidal torque trajectories at 20, 70 and 100 Hz.

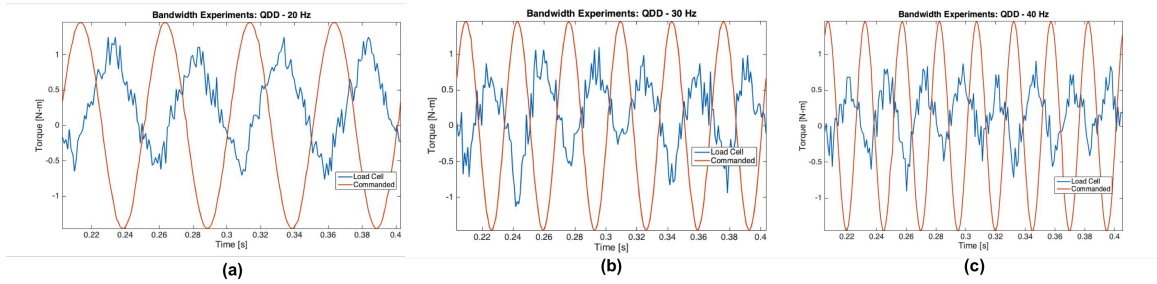


Figure 2.13: Experimental torque bandwidth testing for a QDD (T-motor with a 1-stage planetary gear train) commanded sinusoidal torque trajectories at 20, 30 and 40 Hz

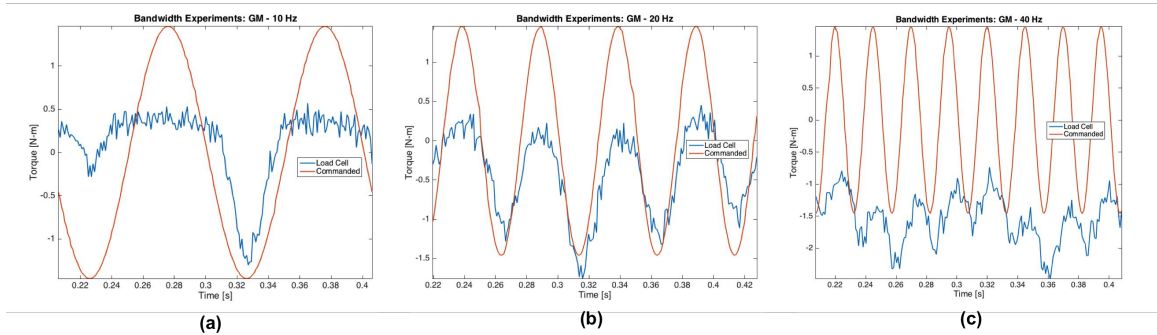


Figure 2.14: Experimental torque bandwidth testing for a GM (T-motor with a 2-stage planetary gear train) commanded sinusoidal torque trajectories at 10, 20 and 40 Hz

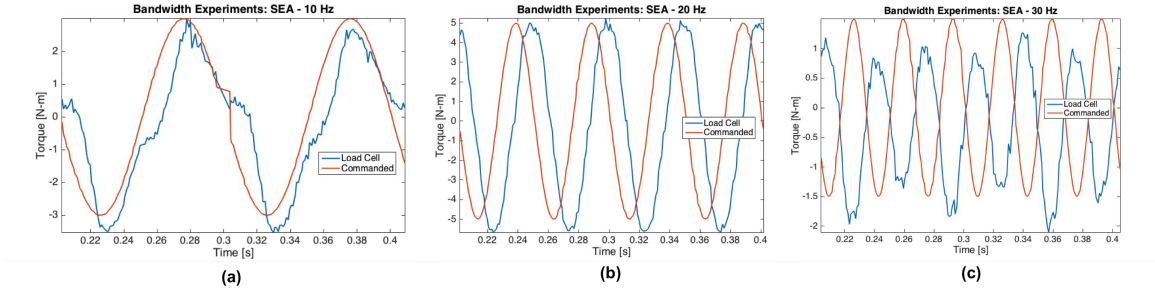


Figure 2.15: Experimental torque bandwidth testing for a SEA (Hebi X5-1) commanded sinusoidal torque trajectories at 10, 20 and 30 Hz.

Proprioceptive Torque Sensing and Rise Time

Because proprioceptive sensing is also of utmost importance in addition to sufficient actuator bandwidth a series of tests were done to measure proprioceptive torque sensing and control accuracy in addition to other traditional actuator performance metrics such as rise time, settling time, overshoot, etc. These results for the 4 actuator types are shown in Fig. 2.16 and the measured performance metrics are all summarized in Table 2.4.2. Fig. 2.16 indicates that DD and QDD actuators have very accurate proprioceptive torque control and sensing to within 0.05 and 0.4 N-m accuracy which corresponds to 12 and 5.4 percent error, respectively. Proprioceptive sensing for GM and SEA configurations are less ideal where errors reach 24 and 28 percent, respectively. It is important to also note that rise time — an important metric for measuring how fast an actuator can generate torque from rest or change torque in a step response — from DD to QDD only differs by 5.8 ms. However, by adding just one more planetary gear stage to the QDD to get the 2-stage GM configuration the rise time differs by a much larger 116.9 ms. Therefore, the advantages of direct-drive are for the most part proven to be preserved by the addition of only a single stage planetary gear stage. Additionally, with the use of a custom designed single stage gear train or a higher-end COTS planetary gear the performance of QDD can be expected to increase and further converge on the desirable performance of the direct-drive approach.

Table 2.4.2 summarizes the series of experiments conducted on the four discussed actuator types: DD, QDD, GM, and SEA. The quantitative results match expected theoretical analysis and relative performance as compared to one another. With a priority on achieving high agility and virtual compliance the specifications of most interest again are accurate, high bandwidth torque sensing and actuation and high force/speed while considering energy efficiency and mechanical robustness factors. Therefore, in this regard and with the mentioned priorities the QDD actuator seems to be the ideal actuator for the particular application of dynamic legged robots.

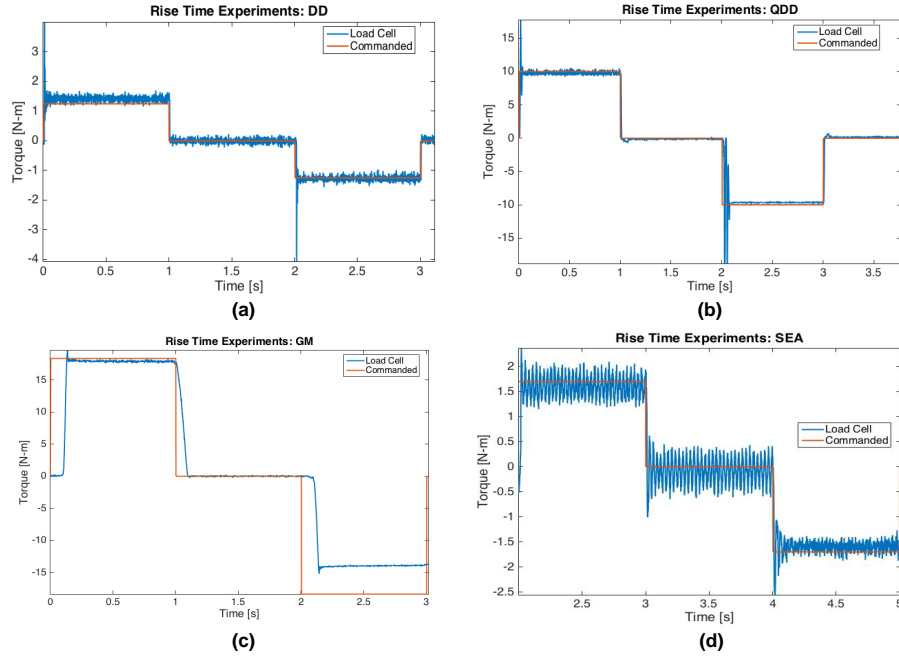


Figure 2.16: (a) DD, (b) QDD, (c) GM, (d) SEA. Rise time, settling time, peak time, overshoot, and proprioceptive torque sensing accuracy and error are calculated using the following step response experiments shown here.

Summary

There are countless design trade-offs and competing design goals when considering actuator design and synthesis of leg topologies to achieve desired performance. It is important to choose a leg topology and actuation scheme which compliment one another to achieve the design specifications for maximum dynamic legged mobility! The following flow charts in Fig. 2.17 and 2.18 show the design methodology and trade-offs for each type of actuator and the resulting robots (or examples of robots) that are produced. The design methodology starts with an unmodified electric brushless DC motor where torque is the limiting resource. Hydraulics, electro-hydraulics, and pneumatics were ruled out of consideration in this thesis because of the large overhead infrastructure (heat exchangers, pumps, internal combustion engines, hydraulic pressure units, etc.), inefficiency (mainly hydraulics), and high impedance of these actuator types.

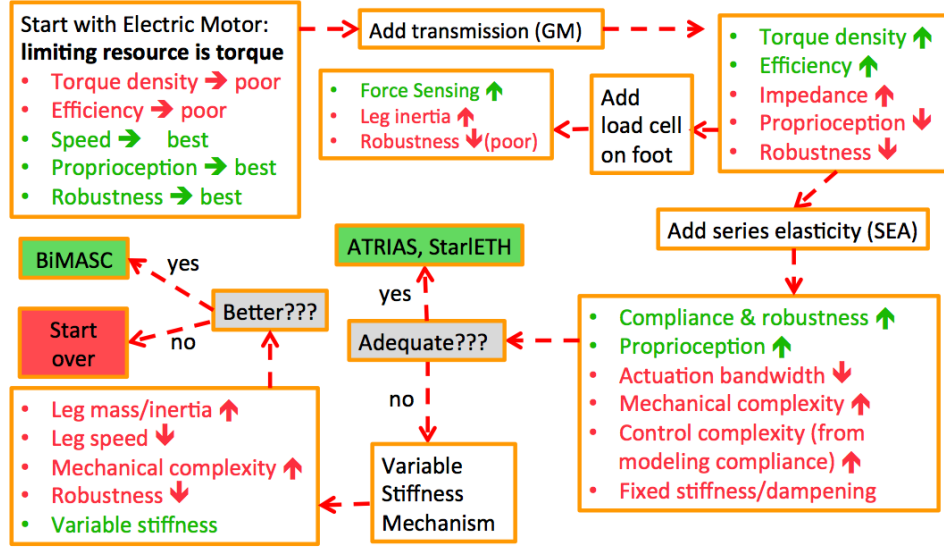


Figure 2.17: Methodology for actuator selection and design starting from the basic, unmodified electric motor where torque is the limiting resource. This specific methodology flow results in robots like StarlETH [11], ATRIAS [10], and BiMASC [21].

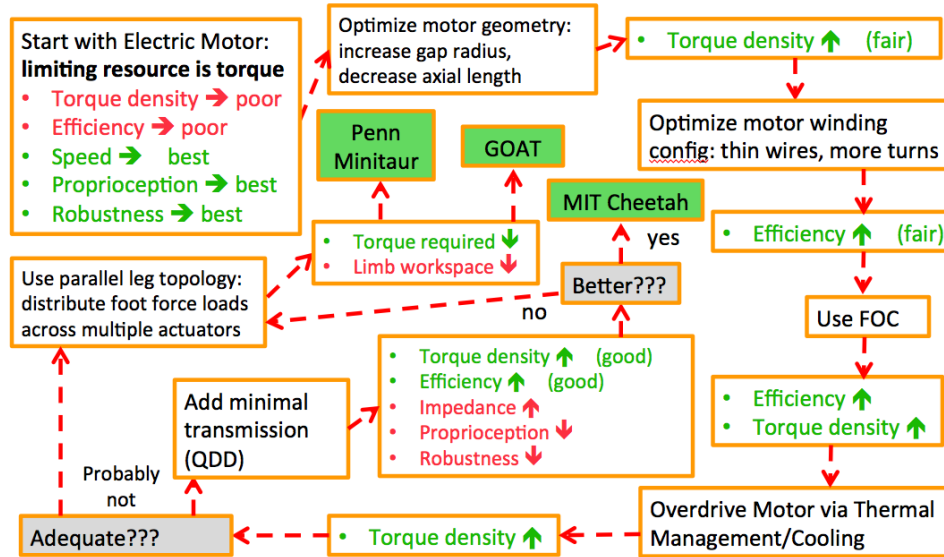


Figure 2.18: Methodology for actuator selection and design starting from the basic, unmodified electric motor where torque is the limiting resource. This specific methodology flow results in robots like MIT Cheetah [9], Penn Minitaur [12], and GOAT, the robot introduced in this thesis.

Actuator Specifications	Units	DD	QDD	GM	SEA
motor manufacturer	-	T-motor	T-motor	T-motor	Maxon
motor model	-	U10	U10	U10	EC-max 16
mass	kg	0.4	0.665	0.93	0.315
peak torque	N-m	6.5	28	196	2.5
continuous torque	N-m	1.45	10.15	71.1	1.3
continuous power	W	111	111	111	19.2
torque density	N-m/kg	3.63	15.26	76.34	4.13
max speed	rpm	4000	570	80	90
static friction	N-m	0.048	0.054	0.061	0.36
gear ratio	-	n/a	7	49	272
reflected inertia	kg-m ²	0.0001	0.0049	0.2401	0.00316
gear stages	-	n/a	1	2	3
gear type	-	n/a	planetary	planetary	spur
spring stiffness	N-m/rad	n/a	n/a	n/a	70
backlash	°	0	1.2	8.4	0.25
torque sensing accuracy	N-m	0.15	0.4	4.4	0.5
torque sensing max error	%	12	5.4	24	28
$\Delta\tau > .5\text{N}$ torque bandwidth	Hz	70	40	20	30
$\Delta\tau < .5\text{N}$ torque bandwidth*	Hz	250	90	40	60
rise time	ms	4.3	10.1	127	11.0
peak time	ms	10.0	15.1	133	17
settling time	ms	33.4	37.3	137	113
overshoot	%	273	77	6.6	51

*Bandwidth of same sign torque changes: $0.75 + .25 \sin(2\pi * f * t)$ Nm.

Table 2.1: Results for a series of actuation tests on 4 types of actuators. All tests were done using a single axis SRI M2210E torque load cell and all actuators were commanded at control frequencies of 1kHz. Gear motor bandwidth is especially poor which is most likely attributed to the large amount of backlash present in the gear train. Higher end gearmotors with lower backlash can be expected to perform much better than results obtained here and with a higher bandwidth than SEAs as suggested by theory and other literature.

Chapter 3

Leg Design for 3D Agility

In this chapter I introduce **GOAT**, the **G**earless **O**mn-directional **A**cceleration-vectoring **T**opology, as a novel leg aimed at surpassing all current leg designs in terms of 3D agility. The GOAT leg, or GOAT, is modular in that it can be configured with various drive motors and gear-trains for either DD or QDD. Additionally, the leg can be used in various legged robot morphologies including monopod, biped, tripod and quadruped. In this dissertation a monopod is the main focus but a CAD rendering of a viable quadruped is shown in Fig. 3.1 and the road is paved to expand to experiments using biped and quadruped morphologies of the same leg topology in the future.

The first truly dynamic legged robots utilizing the direct-drive and quasi-direct-drive approach are the Penn Minitaur (Gavin Kenneally et. al. in [12]) and the MIT Cheetah (Sangbae Kim et. al. in [9]). Much of my work in this thesis is inspired by these two groups and their work with the DD and QDD actuation schemes for dynamic legged robots.

3.1 A Novel 3-RSR Leg Topology

Current dynamically capable legged robots utilize variations of prismatic, series articulated, parallel, or 4-bar linkage leg configurations. While each of these designs has associated advantages and disadvantages, all share a commonality of a sagittally-focused leg Jacobian. This constraint extends to the physical realization and structure of these leg mechanisms which are typically prone to failure modes resulting from out-of-plane loading and impulses [9][10][30]. Therefore, to address the current limitations in sagittally constrained, *2.5D* dynamic robots, I propose a new leg topology with an omni-directional leg Jacobian capable of vectoring large forces at high speeds along any direction in the robot’s frontal plane. The 3-RSR topology (schematic shown in Fig. 3.5(c)) is synthesized as a 3-DOF parallel mechanism which uses coupled actuation to distribute foot loads over three actuators, thus increasing leg thrust for dynamic jumping and reducing individual actuator effort, size, and mass. This is in contrast to the other leg topologies which have decoupled actuators relying on a

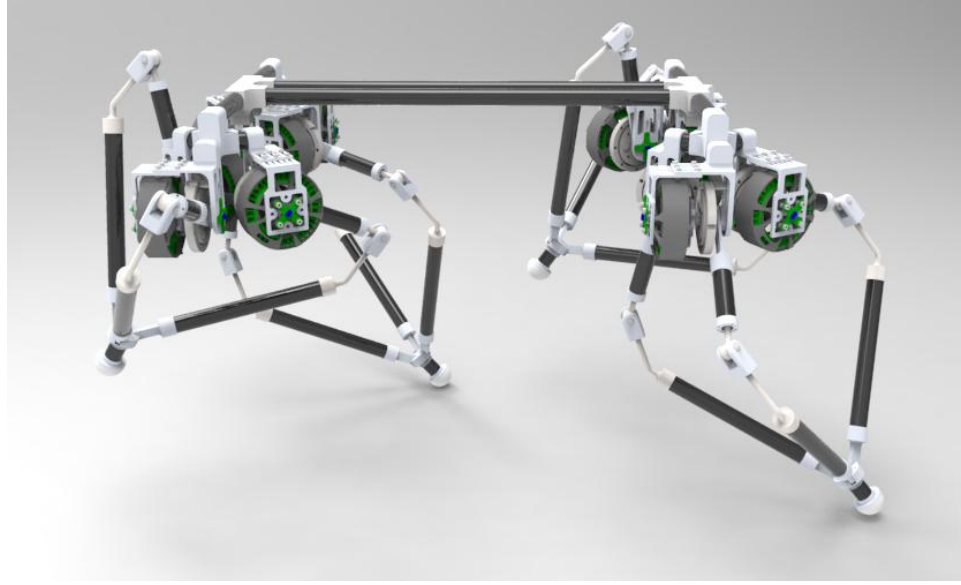


Figure 3.1: CAD Rendering of a viable quadruped using the GOAT leg topology.

single actuator for producing sagittal plane thrust forces and another actuator for producing dorsal plane forces. I describe the kinematics of the 3-DOF, 3-RSR parallel linkage and follow up with an optimization of the mechanism parameters to maximize omni-directional workspace and force map/envelope. Finally, I detail the mechanical design and physical realization of the mechanism.

3.1.1 Kinematics

Forward and Inverse Kinematics

It is well known that the forward kinematics for spatial parallel linkages can be difficult and sometimes impossible to solve analytically. Therefore, to avoid the complexity in determining a closed form solution, the 3-RSR's forward and inverse kinematics are solved using MATLAB's *lsqnonlin()* function and mexxed to C++ for real time constrained optimization. Nine constraint equations construct the cost function for the forward and inverse kinematics optimization. A binary term in the cost function constrains the z-component of foot plate normal to be negative. For the forward kinematics each knee position k_i is known as a function of θ , the actuated joint R_1 at the hip from Fig. 3.2. The constraint eqs. used to solved the kinematics are

$$0 = w_1 \left((a_{x,i} - k_{x,i})^2 + (a_{y,i} - k_{y,i})^2 + (a_{z,i} - k_{z,i})^2 - l_2^2 \right) \quad (3.1)$$

$$0 = w_2 \left((a_{x,i} - a_{x,i+1})^2 + (a_{y,i} - a_{y,i+1})^2 + (a_{z,i} - a_{z,i+1})^2 - f^2 \right) \quad (3.2)$$

$$0 = w_3 \left(\mathbf{n}_b \cdot \mathbf{n}_{k,i} \right) \quad (3.3)$$

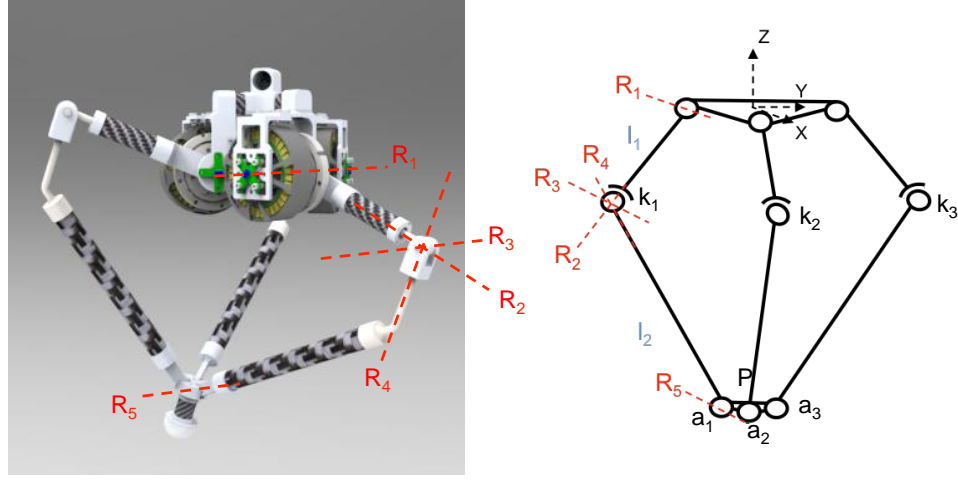


Figure 3.2: the 3-RSR leg topology decomposed into the individual joints at the hip R_1 , knee R_2, R_3, R_4 , and ankle R_5 . Although the mechanism is a 3-RSR the physical realization of the topology is achieved using a 3-RRRRR where the three knee R-joints intersect at a single point for an effective mobility equal to that of a spherical joint.

where,

$$\mathbf{n}_b = \frac{(\mathbf{a}_1 - \mathbf{a}_2) \times (\mathbf{a}_2 - \mathbf{a}_3)}{\|(\mathbf{a}_1 - \mathbf{a}_2) \times (\mathbf{a}_2 - \mathbf{a}_3)\|}$$

$$\mathbf{n}_{k,i} = \frac{(\mathbf{k}_i - \mathbf{a}_i) \times (\mathbf{a}_i - \mathbf{P})}{\|(\mathbf{k}_i - \mathbf{a}_i) \times (\mathbf{a}_i - \mathbf{P})\|}$$

where, $i = 1, 2, 3$ represents each chain of the 3-RSR, w_i is the weight for each constraint in the cost function, \mathbf{P} is the $[x, y, z]^T$ position of the foot center, \mathbf{a}_i is the $[x, y, z]^T$ position of each chain's 'ankle' revolute (R-joint), f is the fixed perpendicular distance between each ankle R-joint, and \mathbf{k}_i represents the $[x, y, z]^T$ position of each chain's spherical 'knee' joint calculated by

$$\mathbf{k}_i = \mathbf{h}_i * \mathbf{T}_{h2k} = [\mathbf{R}_{R_1}(\theta_i), l_1]$$

In Fig. 3.5c The 'ankle' joints are the 3 R-joints (denoted R_5) at the distal foot plate, the 'knee' joints is the point where R_2, R_3 , and R_4 intersect, and the hip joints are attached the top hip plate and denoted by R_1 . The first set of 3 constraint equations (eq. 3.1) constrains the distance between the the knee and corresponding ankle joints to be equal to the length of link 1 (l_2). The second set of constraint equations (eq. 3.2) constrains the distance between adjacent ankle joints to be equal to f . The third set of constraints (eq. 3.3) forces each of the 3 link 2s (l_2) in the 3-RSR to be orthogonal to the foot plate normal because the ankle joint is a 1-DoF revolute joint.

The MEXed MATLAB code compiles and executes the constraint equations in C through each iteration in the MATLAB optimization. Real-time optimization can be achieved at 100 Hz using this method. However, to achieve high fidelity virtual compliance (which is the ultimate goal) the

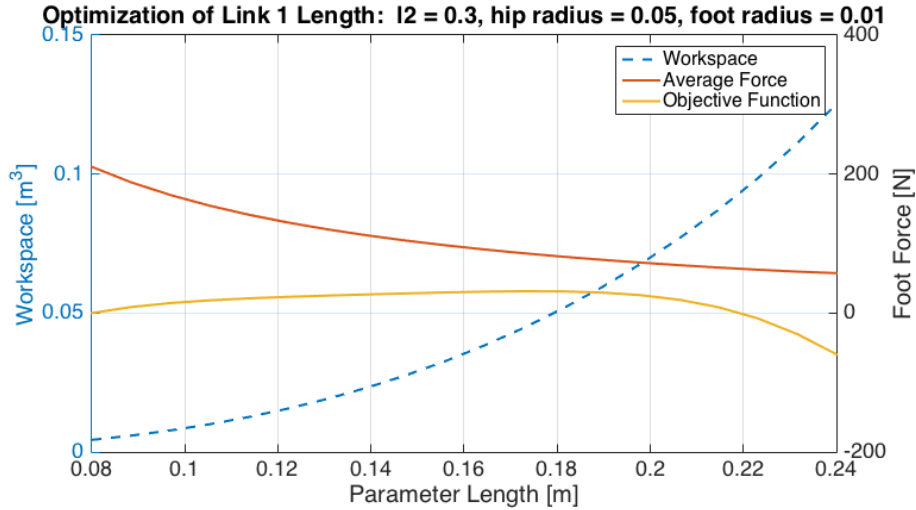


Figure 3.3: Optimization of link 1 length, l_1 , for maximum workspace and force production based on the objective function in eq. 3.5. Here the objective function is scaled to fit the left y-axis.

required control frequency must be close to 1 kHz. Thus, a look-up table for the forward and inverse kinematics is created to meet the control frequency operating constraint. Using the look-up table, and a MEXed look-up search function, solutions to the kinematics can be obtained at greater than 1 kHz rate.

The 3-RSR form factor and workspace appear similar to that of a Delta robot arm which is a purely translational 3-DoF mechanism (unlike the 3-RSR). By removing the parallelism (translation only) constraint, advantageous for rapid pick-and-place operations, the kinematic workspace of the end-effector is increased and the mechanism becomes lighter and structurally more robust¹ Traditional Delta Arms have a limited payload and thus are not structurally robust in withstanding or delivering large environmental forces. Additionally, the Delta robot utilizes a 4-bar linkage as its second link which adds complexity, parts, inertia, and failure modes.

Jacobian

Because the primary control mode for this leg will be force control employing virtual model control through the use of virtual spring and damper components the Jacobian — which is a transformation of infinitesimal kinematics between joint velocity/torques to end-effector velocity/force-torque-wrench — is needed. Like the forward and inverse kinematics the Jacobian is solved numerically by differentiating the forward kinematics transformation matrix with $\epsilon = 10^{-6}$ for adequate numerical

¹The Delta Robot arm is kinematically equivalent to a 3-RUU but uses 3 parallel planar 4-bar linkages to connect the ‘knee’ joints to the ‘foot’ plate or end-effector. The parallel 4-bar constrains the top and bottom plates to be parallel but adds design complexity, weight, and inertia to distal portions of the leg.

accuracy. For the 3-RSR leg, the Jacobian is a 6 by 3 matrix² where each column in the matrix describes each of the 3 actuators contribution to the 6-axis force-torque wrench at the end-effector (i.e. foot). The Jacobian is constructed as follows

$$\mathbf{J}_{6 \times 3}(\boldsymbol{\theta}) = \begin{bmatrix} \mathbf{T}_{3 \times 3} \\ \boldsymbol{\Omega}_{3 \times 3} \end{bmatrix} \quad (3.4)$$

$$\mathbf{T}_{3 \times 3} = \frac{1}{\epsilon} \begin{bmatrix} \mathbf{b}_{t,1} - \mathbf{a}_{t,1} & \mathbf{b}_{t,2} - \mathbf{a}_{t,2} & \mathbf{b}_{t,3} - \mathbf{a}_{t,3} \end{bmatrix}$$

$$\boldsymbol{\Omega}_{3 \times 3} = \frac{\mathbf{A}_{R,i}}{2\epsilon} \begin{bmatrix} \mathbf{W}_{32} - \mathbf{W}_{23} & \mathbf{W}_{13} - \mathbf{W}_{31} & \mathbf{W}_{21} - \mathbf{W}_{12} \end{bmatrix}^T$$

where $\mathbf{W} = \mathbf{A}_R^T \mathbf{B}_R$ and $\mathbf{B}_i = \mathbf{T}_{h2f}(\boldsymbol{\theta} + \epsilon) = [\mathbf{B}_{R,i}, \mathbf{b}_{t,i}]$, $\mathbf{A}_i = \mathbf{T}_{h2f}(\boldsymbol{\theta}) = [\mathbf{A}_{R,i}, \mathbf{a}_{t,i}]$ are transformations from the hip to the foot \mathbf{T}_{h2f} , for chain i , with input hip angles $\boldsymbol{\theta} + \epsilon$ and $\boldsymbol{\theta}$, respectively.

Parameter Optimization

To maximize workspace and average force production throughout the workspace an optimization, shown in Fig. 3.3, was conducted to determine the leg link lengths, l_1 and l_2 , and hip/foot radii, r_h and r_f respectively, over a range of physically tractable dimensions. The optimization maximized the following objective function O over the parameters: $\mathbf{q} = [l_1, l_2, r_h, r_f]$

$$O(\mathbf{q}) = \left(c_1(\mathbf{q}) * c_2(\mathbf{q}) \right) \cdot \left(c_1(\mathbf{q}) + c_2(\mathbf{q}) \right) \quad (3.5)$$

where, $c_1 = w_1 * V_{ws}$ is the normalized volume of the mechanism's workspace and $c_2 = w_2 * F_{avg}$ is the mean force produced throughout the usable workspace. This optimization yields link lengths of $l_1 = 0.165$, $l_2 = .3$, $r_h = .05$, and $r_f = .01$, where r_h and r_f are the respective radii from the hip and foot plate center to R-joints R_1 and R_5 from Fig. 3.5(c). This optimization yields a kinematic workspace with two leg configurations (knee-above-the-hip and knee-below-the-hip shown in Fig. 3.30) where the transition between configurations does not pass through a singularity similar to the simpler 2-DoF planar parallel Minitaur leg [12]. Having both configurations available nearly doubles the usable workspace of the limb to a volume of $0.0285m^3$ as compared to traditional parallel linkages which only use knee-below-hip configuration in which case the workspace volume with identical leg parameters would be $0.0151m^3$. Using the entire workspace allows the leg to deliver 1.68 times more kinetic energy to the body while decreasing energy losses due to landing collisions, as seen in Fig. 3.30. The kinetic energy delivered to the body is calculated by

$$E = \int_{\theta_0}^{\theta_f} \left(F(\tau, \theta) \cdot d(\theta) \cos(\phi) \right) d\theta \quad (3.6)$$

²the size of the Jacobian is 6 by 3 because the force-torque wrench is a 6x1 vector and the number of driven actuators is 3 or a 1x3 vector.

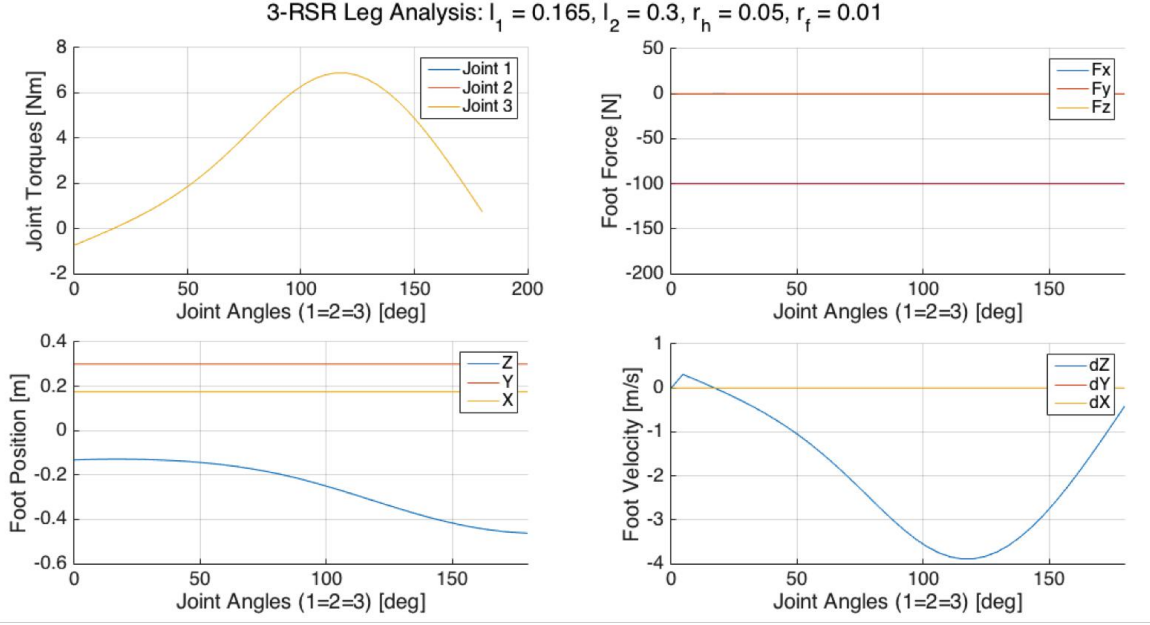


Figure 3.4: Characterization of the joint torques, foot position, foot velocity, and foot force for a vertical jump. The foot force plot shows force produced by constant hip joint torques of 5 N-m for an example vertical foot trajectory where all 3 hip angles are the same due to symmetry. The joint torque plot shows the actuator torques required to produce a constant 100N for downwards at the foot. For a vertical leg trajectory all 3 joint angles are the same for each point in the trajectory since the mechanism is symmetric. For omni-directional force vectoring the joint angles and torques will not be the same.

where $\theta_0 = 0^\circ$ for the full workspace while $\theta_0 = 90^\circ$ for traditional knee-below-hip only configuration. F is the foot force, d is the traveled foot distance, and ϕ is the angle between F and d . $\theta_f = 180^\circ$ for both configurations. The mechanical realization of the 3-RSR linkage has a slightly smaller input angle range due to physical interference constraints (30 - 150° as opposed to 0 - 180°). With the physically tractable joint ranges this linkage is capable of transferring 27.0 J of energy to the body per jump per leg whereas the traditional knee-below-hip design only delivers 19.1 J of energy to the body.

Additionally, the inherent symmetry of the leg enables omni-directional force and body-acceleration vectoring. Because the actuators for leg motion in the sagittal and dorsal planes are directly coupled, the leg distributes foot loads over all 3 actuators to produce foot forces in the sagittal plane, dorsal plane, or a force vector with components in both the sagittal and dorsal planes (i.e. any vector in the frontal plane)³.

Fig. 3.4 characterizes the kinematic relationship between the applied hip-joint torques, foot forces, foot position and velocity for an example vertical foot trajectory. Using the transpose of

³SE(n) refers to the Special Euclidean group where degrees of freedom for SE(n) is $n(n+1)/2$, which gives 3 (x, y, θ) when $n = 2$, and 6 $(x, y, z, \alpha, \beta, \gamma)$ when $n = 3$.

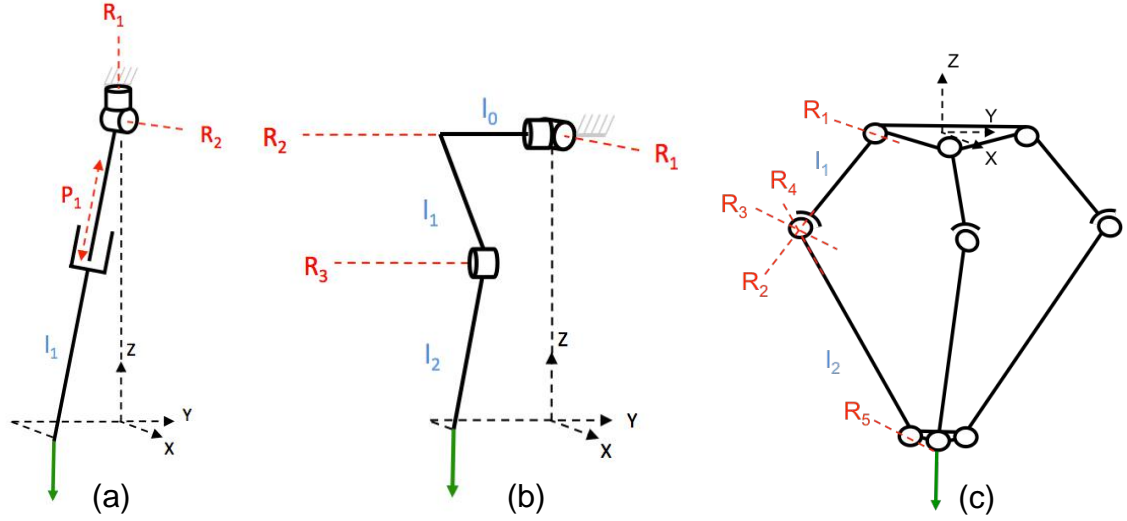


Figure 3.5: Kinematic diagrams showing leg parameters (Table 3.1 and joint axes for (a) 3-DoF prismatic, (b) 3-DoF series-articulated, and (c) 3-DoF 3-RSR Parallel Spatial topologies.

the leg Jacobian, the joint torques required to produce a force-torque wrench at the foot with a z -component of $-100N$ can be calculated. Similarly, the entire omni-directional force envelope is quantitatively determined and plotted in Figs. 3.6 and 3.7. The relatively large workspace and force envelope of this mechanism, as compared to traditional parallel linkages, shows potential for enhanced jumping by utilizing the two regions of maximum force production — located at the proximal and distal regions of the workspace — and high foot speeds in the middle of the workspace.

3.2 Comparison of 3-DoF Leg Topologies

Here I show that the 3-RSR leg topology is advantageous over other, more common, leg topologies for proprioceptive sensing and explosive omni-directional jumping maneuvers (i.e. 3D agility). In Figs. 3.6, 3.7, and 3.8 and Table 3.2 I compare the 3-RSR leg against conventional series-articulated leg designs (MIT Cheetah, StarLETH, SpotMini) and prismatic legs (Raibert Hopper, simplified SCHAFT 2016) in end-effector workspace and force envelope.

I define four measures of legged 3D agility listed in Table 3.2 as the energy delivered by leg thrust (E); the force envelope volume (Ψ) which describes how much force can be exerted over the limb's workspace; the foot force to leg mass ratio, or limb acceleration (Λ); and the proprioceptive force sensitivity (Π) which is a metric of the minimal joint torque resolution required to measure a change in foot force f to $f + \epsilon$ at foot position i within the limbs workspace, where ϵ is arbitrarily small (1 N in this study). These measures are normalized by assuming all leg topologies have an identical set of 3 equally sized and performing actuators.

$$E = F_{avg} (d_{foot})_{max} \quad (3.7)$$

$$\Psi = F_{avg} \cdot V_{ws} \quad (3.8)$$

$$\Lambda = \frac{F_{avg}}{m_l} \quad (3.9)$$

$$\Pi = \frac{1}{n} \sum_{i=1}^n |J_i^T F(f) - J_i^T F(f + \epsilon)| \quad (3.10)$$

where F_{avg} is the average foot force along a foot trajectory, m_l is the unsprung leg mass, and $(d_{foot})_{max}$ is the maximum distance traveled by the foot along a linearly extending trajectory as shown by example in Fig. 3.7(c) by the black line. $(d_{foot})_{max}$ is a function of the limbs workspace V_{ws} .

Topology	Leg Parameters						
	[kg]	[m, m, m]			[deg, deg, deg]		
	m_l	l_0	l_1	l_2	J_1	J_2	J_3
Prismatic	.91	n/a	.254	n/a	360	56	.25m
Series	.46	.05	.225	.225	40	150	107
3-RSR	.63	.05*	.165	.3	120	120	120

Refer to Fig. 3.5 for parameter definitions. Parameters for prismatic & series articulated topologies are taken from the Raibert Hopper & MIT Cheetah legs [6][38].

Note:* Indicates dimension of the 3-RSR's hip radius which is not a moving link.

Table 3.1: Comparison of leg parameters for three different 3-DoF leg topologies.

3.2.1 Force Envelope Analysis

Figures 3.7, 3.6 show that to produce a force-torque wrench, F_{foot} , as defined in eq. 3.12 the required joint torques are smaller for the 3-RSR leg than for the other topologies. The plots are generated using a quasi-static force analysis in which joint torques are solved using the Jacobian transpose method

$$\tau_m = J^T F_{foot} \quad (3.11)$$

$$F_{foot} = f[-\sin \phi \sin \theta, -\sin \phi \cos \theta, \cos \phi, 0, 0, 0]^T \quad (3.12)$$

where $f = -100$ N, $\phi = \tan^{-1}(\frac{step\ length}{step\ height})$, and θ is the direction or heading in the frontal plane ($\theta = 0^\circ$ points in direction of +Y).

The 3-RSR parallel leg topology shows advantages over series-articulated legs by allowing all actuators to be placed in the hip/body maintaining a very low inertia, and thus high speed, limb. The MIT cheetah minimizes this effect in its serial-articulated limb by locating the hip and knee

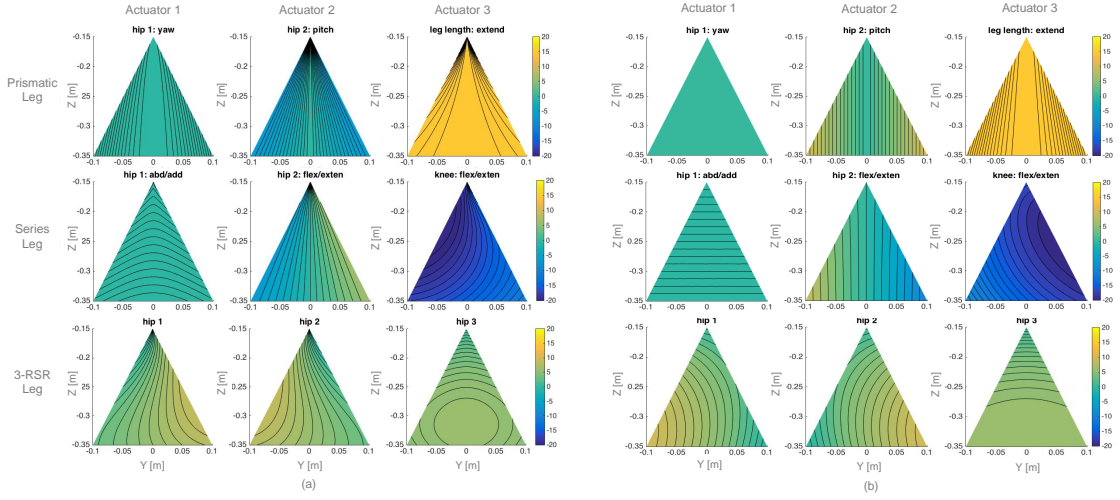


Figure 3.6: Sagittal-plane force envelope comparison. The y and z axes correspond to the coordinates of the foot in the leg frame. The color contour represents the required torque from each actuator to produce the defined force wrench at that coordinate (i.e. position) in the workspace. (a) and (b) represent forces identical to those described in fig. 3.7.

motors co-axially at the hip and using a parallel 4-bar linkage to actuate the knee joint from the hip. However, this design still requires the hip joint actuator to rotate the mass of the knee actuator, thus the knee-actuator mass is not decoupled from the leg inertia [9].

Additionally the 3-RSR linkage uses its actuators in parallel similar to ATRIAS but with a larger 3D workspace (normalized by leg length), due to the two available configurations. This parallel topology allows the actuators to share the load at the foot, generating multiple times the jumping force as compared to the traditional series-articulated and prismatic limb topologies which decouple the leg actuators to control leg angle and leg length separately, relying solely on the knee actuator to produce the majority of the thrust force. The 3-RSR allows all 3 actuators to be fully utilized in sharing the fast and large loads of jumping.

Figs. 3.7 and 3.6 show that for the MIT Cheetah to rival 3-RSR Goat's jumping capability for a given robot mass, their knee-joint actuator must be roughly 2.5 times as powerful as one of GOAT's actuators in addition to still requiring its other two motors for hip flexion/extension and hip abduction/adduction used for out-of-sagittal plane force production. Fig. 3.7 shows that for the series-leg to produce omni-directional force the hip abduction actuator must have 1.2 times more torque than any actuator on the 3-RSR while the hip flexion/extension actuator must produce roughly the same amount of torque as any actuator on the 3-RSR. Additionally, the 3-RSR limb inertia and unsprung mass can be kept very low because all actuators are co-located in the hip.

Designing the leg to be symmetrical about its vertical axis ⁴ allows foot forces to act through

⁴the vertical axis is the intersection between the dorsal & sagittal planes

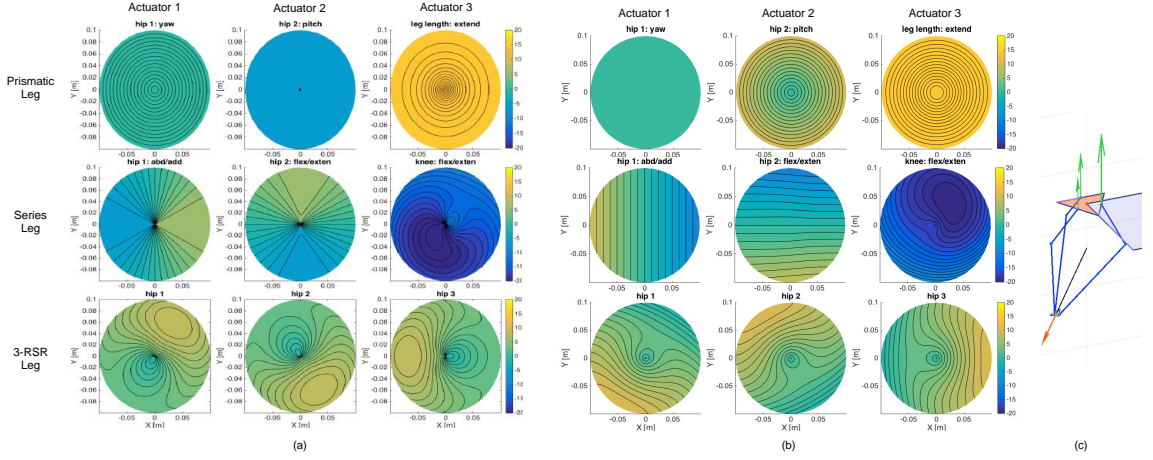


Figure 3.7: Frontal-plane force envelope of the 3-RSR leg as compared to the series-articulated and prismatic legs. The x and y axes correspond to the coordinates of the foot in the leg frame. The color contour represents the required torque from each actuator to produce the defined force wrench at that foot coordinate in the workspace. In (a) the force generated at the foot follows eq. 3.12, while the foot force in (b) is always -100 N in the z -direction. (c) shows a simulation of the 3-RSR leg producing a force vectored in the direction indicated by the orange arrow. The green arrows indicate relative magnitude of the 3 actuator torques required to produce the desired foot force. For a vertical foot trajectory & force the 3 green arrows will be equal.

the hip which is ideal for anchoring simple SLIP model-based controllers [61]. This symmetry also enables the leg to apply equal forces at the foot to jump forward and backward as it can to jump sideways or diagonally in arbitrary directions. Therefore, with equal jumping forces at each leg the 3-RSR quadruped, GOAT, can jump vertically upwards. Alternatively by using differential forces in the legs effective force and acceleration vectoring can be achieved to induce rotational moments and omni-directional jumps. Thus, for a given set of actuators the 3-RSR leg topology exceeds the force production capabilities of currently existing legged robots with respect to dynamic agility and full-body motions in the full space of $SE(3)$.

Additionally, it's worth noting that both the MIT Cheetah and ATRIAS robots suffer from structural failures in their limbs due primarily to out-of-sagittal-plane loads [38][10]. This is because both robots use planar leg mechanisms and only extend them into the third dimension by adding an abduction/adduction joint which rotates the entire leg but does not address structural integrity to forces out of the leg frame's sagittal plane. The 3-RSR leg was designed to deliver omni-directional force and thus by Newton's 3rd law be robust to equal and opposite omni-directional structural loading.

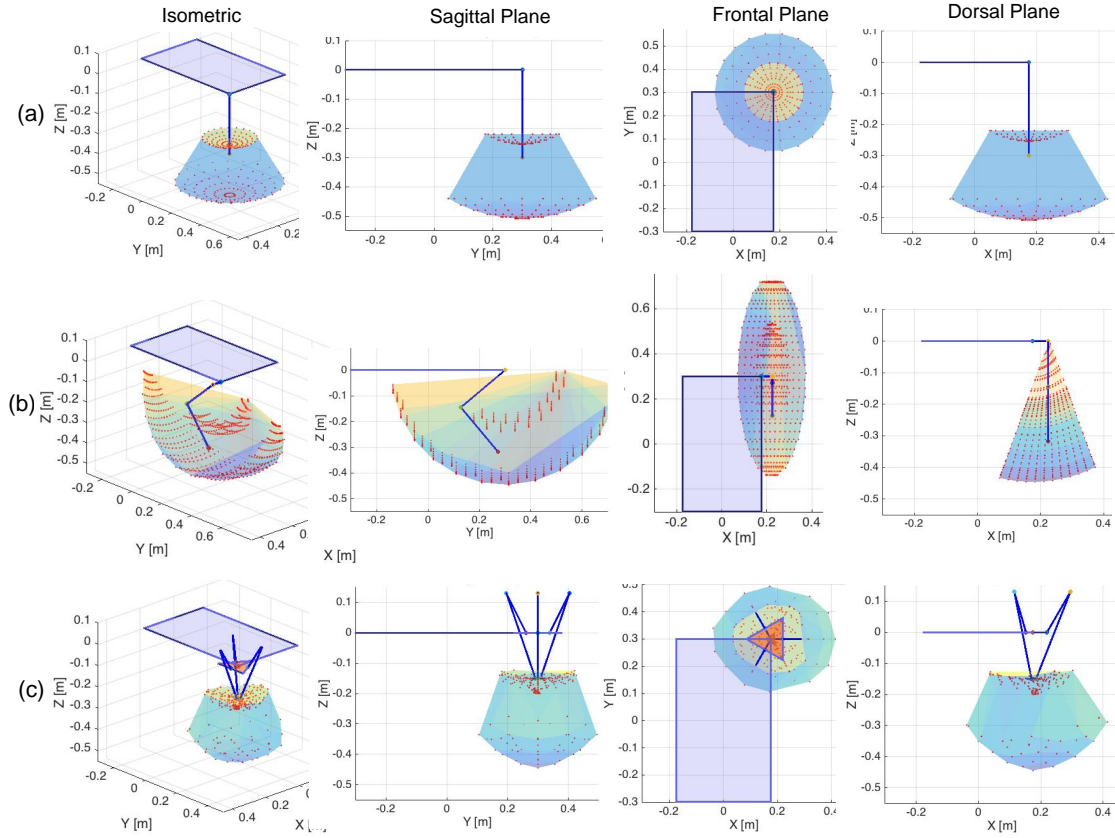


Figure 3.8: Workspace volume for the (a) prismatic, (b) series-articulated, & (c) 3-RSR topologies shown on a quadruped body hiding all but 1 leg. Joint limits used for series-articulated & prismatic legs are based on the joint limits of the MIT Cheetah & the Raibert Hopper.

3.2.2 Workspace Analysis

Figure 3.8 shows the available workspace for each of the leg topologies. I highlight that although the 3-RSR has a smaller limb workspace than series-articulated legs, this sacrifice is reasonable considering the subset of the entire workspace of legged robots which is actually used in practice to walk, run, or jump is not excessively large and is for the most part contained within the 3-RSR's workspace. Tasks involving manipulation using limbs or climbing steep terrains may be less optimal with the 3-RSR topology where both the mechanism volume and smaller relative workspace may hinder mobility. Compared to conventional parallel mechanisms the 3-RSR has superior workspace which can be attributed to the dual configuration of the knee joint where each configuration can be smoothly reached without forcing the mechanism to pass through a singularity

The workspace analysis indicates that the prismatic limb topology has the smallest usable workspace of all considered configurations. This is due to the smaller joint space or range of motion

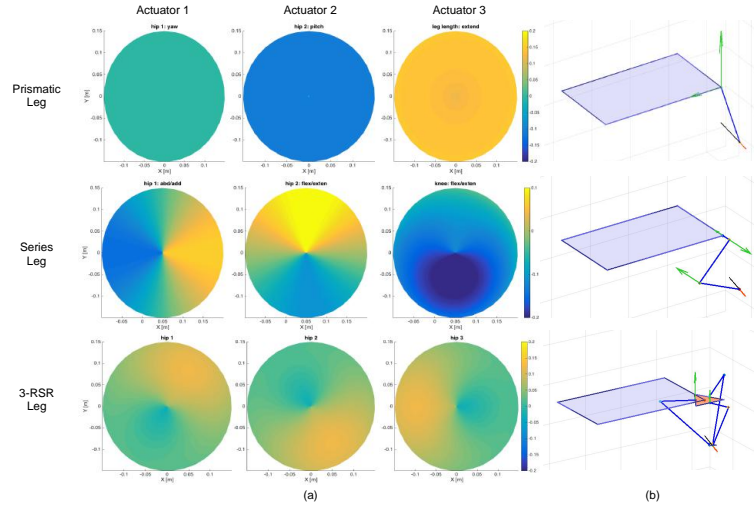


Figure 3.9: (a) Top view of frontal plane for each leg topology. The contour plot indicates by color what the proprioceptive sensitivity (i.e. torque in N-m) of each actuator is to a 1 N force acting on the foot. The coordinate on the plot corresponds to the $\{x,y\}$ position of the foot. (b) Matlab kinematic simulation of each foot topology vectoring force in an arbitrary direction.

of pressure-based linear actuators taken from the specifications of the original Raibert Hopper [6]. Rotary to linear mechanisms such as the crank-slider, rack and pinion, and ball-screws can allow for electromagnetic rotary actuator use but these mechanisms introduce transmission losses and extra linkages which increase actuator impedance, leg inertia, weight, and volume. The full quantitative analysis of workspace is summarized in Table 3.2

3.2.3 Proprioceptive Force Sensitivity Analysis

A major theme in the synthesis of the 3-RSR leg was design for simple, high fidelity, virtual model control which would ultimately enable virtual compliance. To achieve such performance an important criteria is the ability to

1. rapidly change actuator torques to emulate the bandwidth of a mechanical spring-damper
2. accurately sense and deliver foot forces using joint torques through the leg Jacobian.

From the second criterion, it is evident that the force transparency of the entire leg system must be maximized to ensure accuracy in forces being sensed and delivered to mimic mechanical compliance at kHz time scales. Proprioceptive sensing accuracy, by means of measuring motor current, is hindered by mechanical impedance in the load path. Therefore, total leg impedance must be minimized. Mechanically, this can be addressed by eliminating or minimizing all sources of friction, stiction, and backlash.

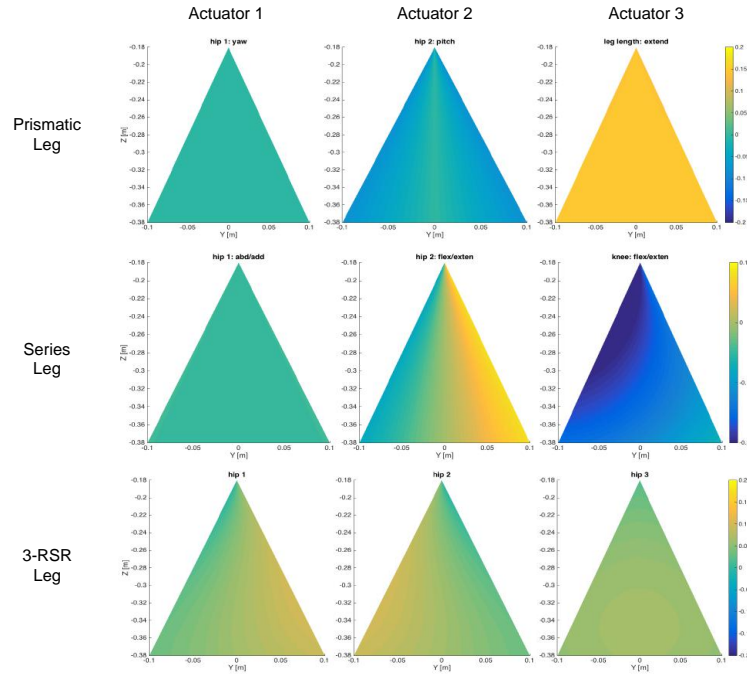


Figure 3.10: Side view of the sagittal plane for each leg topology. The contour plot indicates by color what the proprioceptive sensitivity (i.e. torque in N-m) of each actuator is to a 1 N force acting on the foot. The coordinate on the plot corresponds to the y,z position of the foot.

Proprioceptive sensing is also dependent strongly on leg topology which determines the Jacobian. Because the transpose of the leg Jacobian relates foot forces and joint torques, an ideal leg topology for accurate proprioceptive sensing will have a leg Jacobian with a high sensitivity in joint torques to changes in foot force. This design insight, in combination with minimizing mechanical impedance is needed to design limbs with adequate proprioceptive force sensitivity for virtual compliance.

Figs. 3.9 and 3.10 show — for every foot position in the each limb’s workspace (prismatic, series-articulated, 3-RSR) — the proprioceptive force sensitivity Π . The contour plot’s color represents the value of Π , the minimum torque resolution needed to sense a 1N force change at the foot in the position designated by the (x,y) or (y,z) coordinate of plots 3.9 and 3.10, respectively.

3.2.4 Energy Transfer

Energy delivery is an important metric for legged robots planning to jump explosively or run at high speeds. During running in humans and animals leg swing speed can reach greater than 1080 degrees per second and leg forces can reach 3 times the weight of the body. Therefore, maximizing energy delivery and power, defined by leg velocity times leg force is an important metric to consider

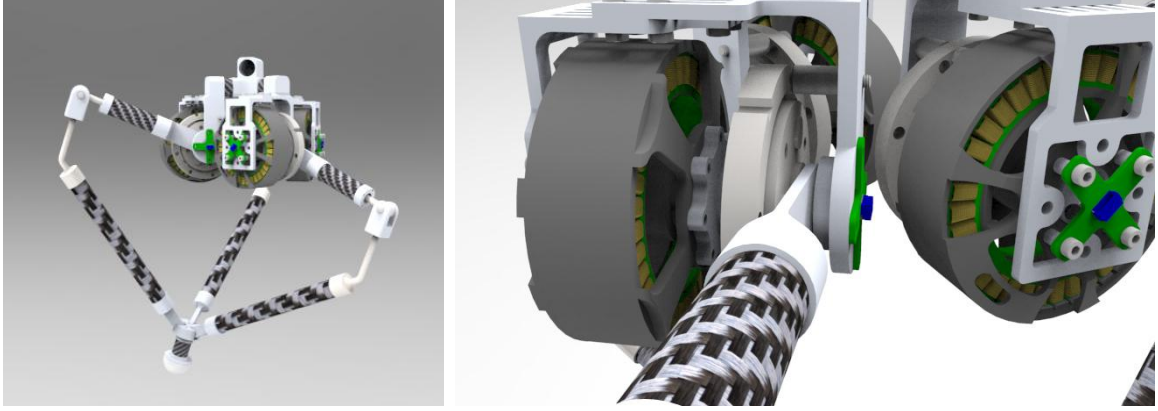


Figure 3.11: Renderings of CAD models for the 3-RSR leg design and actuator modules.

when design for high jumping and running. Table 3.2 summarizes the comparison in performance and required actuation torque for each of the discussed leg topologies.

3.2.5 Summary

The design of the 3-RSR attempted to balance and optimize many metrics associated with legged agility and proprioceptive force control. Table 3.2 provides a summary and comparison of the 3-RSR's performance metrics as compared to the series-articulated and prismatic leg topologies.

Topology	Max Actuator Torque [N-m]			Work Space [m ³]	Leg Volume [m ³]	Foot Force [N]	Foot Speed [m/s]	Limb Inertia [kg-m ²]	E [J]	Ψ [N-m ³]	Λ [m/s ²]	Π [N-m]
	1	2	3									
Prismatic	0.6	9.1	15.0	.0283	.0006	33.3	2.82	0.111	6.7	.94	37	0.0226
Series	11.2	6.7	22.5	.0395	.0030	36.4	9.65	0.058	7.3	1.44	79	0.0667
3-RSR	9.5	9.5	9.5	.0285	.0171	131.5	2.65	0.015	27.0	3.75	209	0.0506

Note: Max Actuator Torque refers to the maximum torque required to produce the wrench in eq. 3.12 at every point in a vertical foot trajectory. Leg Volume is the max (worst-case) volume the mechanism can consume. Foot Forces and Velocities are the average over a vertical leg trajectory. The prismatic leg uses a rotary to linear mechanism with a reduction of 1:6.7. Ψ is the value of the workspace volume multiplied by the average foot force in that workspace.

Table 3.2: Comparison of performance measures for 3-DoF leg topologies.

3.3 Mechanical Design of the 3-RSR

The 3-RSR is mechanically constructed of a hip plate, foot plate and 3 identical legs consisting of two links that connect the hip to the foot. The kinematic configuration of the leg is shown in Fig. 3.2 where the physical realization of the mechanism is a 3-R-RRR-R or 3-5R, where each R-joint

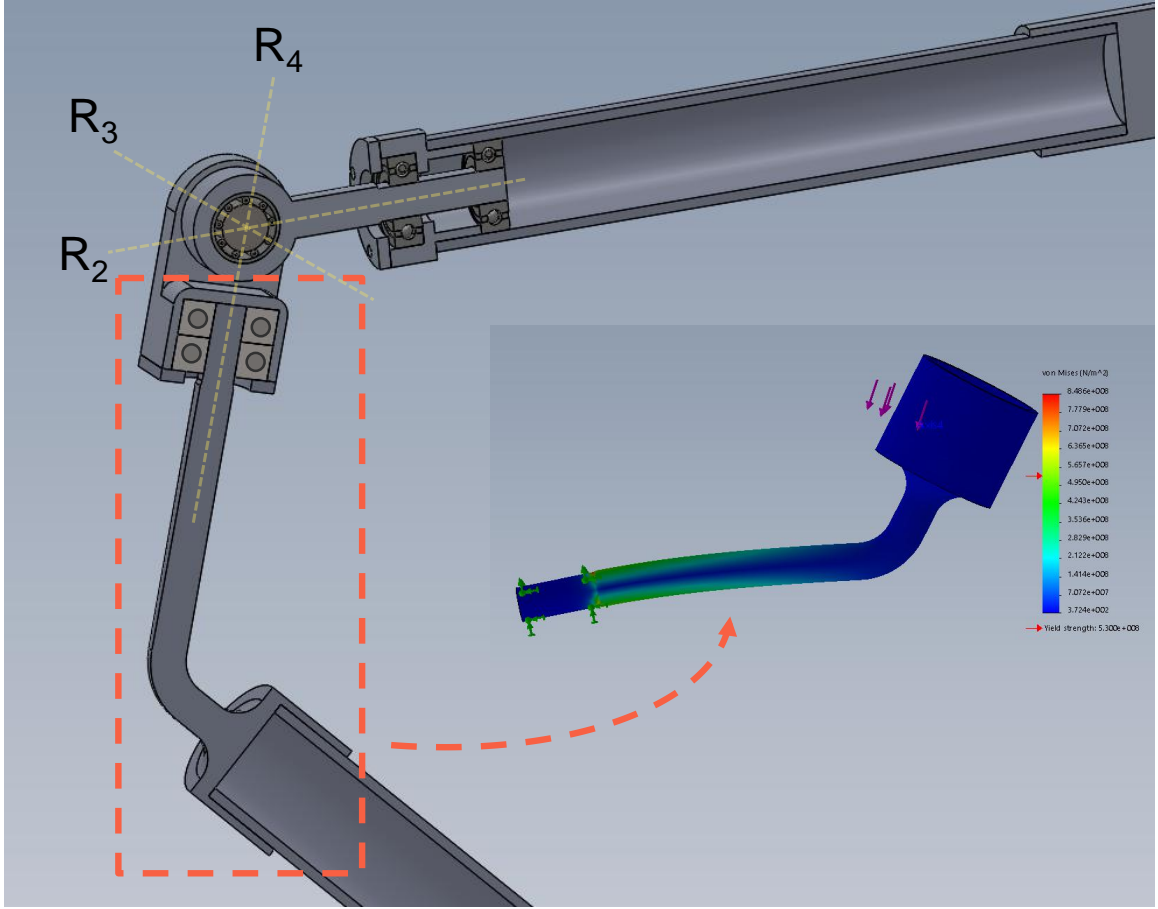


Figure 3.12: Knee joint design showing the 3 revolute joints with intersecting axes. Solidworks FEA results indicate that stresses as high as 123 ksi are present at the bearing support shaft of the distal knee segment with a conservative applied force of 300 N and safety factor of 4. Therefore, this component is machined from medium carbon steel with 125 ksi yield strength in contrast to most of the other components which are machined from 7075 Aluminum with 73 ksi yield strength.

denotes a 1-DoF revolute joint. The three motors are coupled directly to their corresponding first link or through a single stage planetary transmission in the case of QDD actuation. The motor stator is bolted to the hip structure which is adjustable to accommodate different actuator configurations (DD or QDD). Link 1 (l_1) is double supported by bearings on each side to increase moment loading capacity. l_1 has one rotational degree of freedom about revolute joint axis 1 (R_1) in Fig. 3.2 where the axes of the three hip joints are parallel to the hip plane but phased 120° apart to evenly space the 3 legs of the 3-RSR.

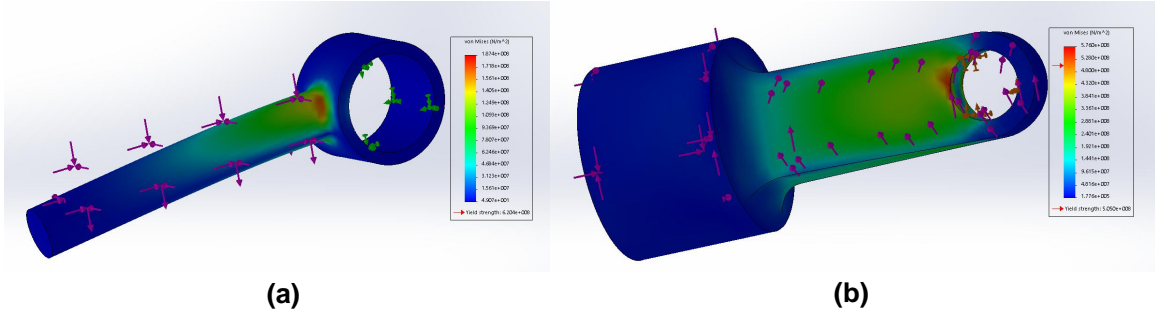


Figure 3.13: FEA was conducted on each component and the two other critical components were determined to be (a) the other extended shaft in the knee (R_2) and (b) the ankle link which connects the foot to the carbon fiber l_2 rod. A static analysis was used to determine the maximum expected force each part could see and those forces ranging from 75N to 200N were applied in the FEA.

3.3.1 Spherical Knee Joint Design

The knee joint consists of three, 1-DOF revolute joints whose rotation axis intersect at one point as shown in Fig 3.12. This configuration achieves the mobility of a spherical joint however the range of rotation about each of the three axis is much larger than that found in typical COTS ball-in-socket spherical joints. The range of motion for joints R_2 and R_4 is 360° while the range for R_3 is $\pm 90^\circ$. A typical COTS ball joint will have one axis with full 360° range of rotation while the other two axis will have $\pm 35^\circ$ of rotation [66]. Therefore the use of this RRR knee joint enables a significantly larger limb workspace that would not have been possible with a commercially available ball joint. The extended range of motion of the RRR joint allows for the leg to pass through its two configurations: knee-above-hip and knee-below-hip as shown in Fig. 3.30.

To avoid interference between l_1 and l_2 , and l_2 and the motor, an offset was integrated into the distal knee segment with a fixed angle. Although this fixed-angle offset addresses interference issues, the trade-off is an increase in bending moment loads, higher stresses, and re-locating the leg's point of singularity to occur when the foot is in the middle of it's workspace as opposed to having the singularity sit at the distal edge of the workspace (as is the case when the fixed angle is 0°). The singularity occurs when the foot is in a position that causes the axes of R_2 and R_4 to align and become coincident — essentially removing a degree of freedom in the knee. When the leg passes through this singularity at high speeds, vibrations propagate through the mechanism and peak stresses are generated. This singularity can however be re-positioned to different, less utilized, regions of the workspace by modifying the fixed angle in the knee offset. Fig. 3.14 shows the relationship between the fixed knee angle and total angular joint range of the driven link, l_1 which is directly correlated to the volume of the workspace. The optimization plot indicated that to maximize the range of motion for the hip (driven) joint which would allow for a greater workspace and more energy delivered, the knee joint should have a fixed angle of 130° .

FEA analysis showed that the knee joint as the most stress critical element of the design and

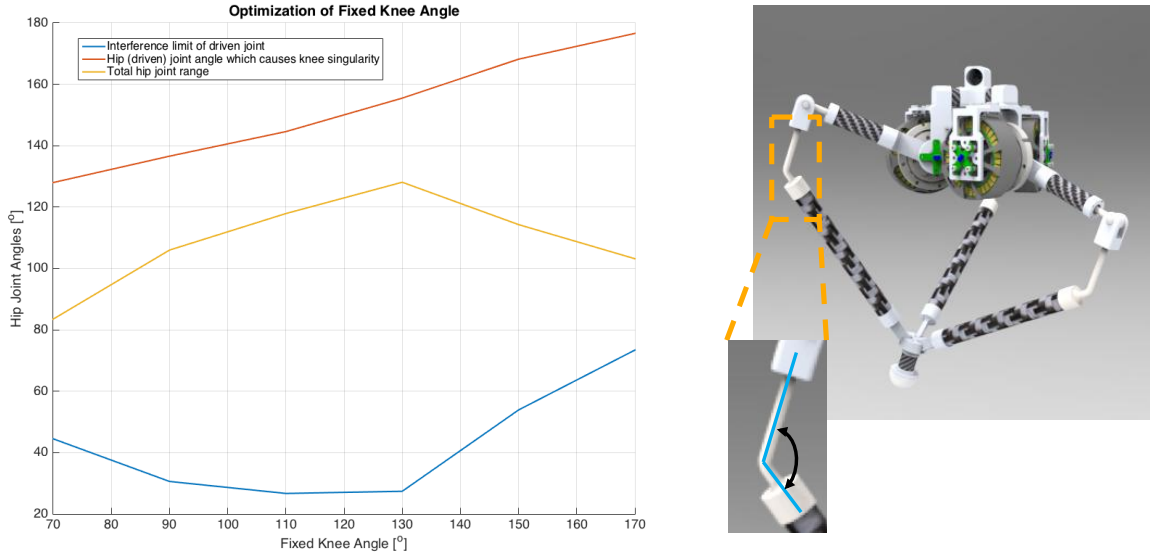


Figure 3.14: Optimization plot showing the relationship between the fixed knee angle and total hip joint range.

thus most prone to failure modes. The FEA on the most distal knee segment (with the fixed angle offset) showed that peak Von-Mises stresses exceeded the yield strength of aluminum during the most critical loading period which occurs during jumping and landing. Therefore, a medium carbon steel (McMaster C300 or 1144 steel) with yield strength of 110-125 ksi and high impact resistance is used to increase resiliency to impact loads reaching 300 N.

To minimize the mechanical impedance of the leg mechanism with force transparency in mind, a large effort was made to reduce and eliminate all sources of friction in the 15 joints on each 3-RSR leg. Therefore, rather than the more cost effective use of bushings, each of the 15 joints utilize one or more bearings to reduce friction while being rated to handle large radial and moment loads seen at the respective joints. For the knee joint two ball-bearings are housed within the hollow carbon fiber l_1 tube 20mm apart and constrain the shaft of R_2 as shown in Fig. 3.12. The middle R-joint R_3 , is a clevis joint constructed from a needle roller bearing used to support large radial loads. R_3 is always orthogonal to both R_2 and R_4 . The bearing has minimal to no thrust loading so the shaft is press fit into one side of the clevis and 0.005" delrin (also known as polyoxymethylene or acetal) shims are used to reduce friction between the inner surfaces of the clevis and pin's housing. The large moment loads created by the knee offset also must be reacted by the bearings and the clevis housing. Therefore, the distal knee R-joint, R_4 is designed using two angular contact bearings arranged back-to-back in an O-configuration to increase the effective fulcrum, and thus moment load rating, of the bearings. Links l_1 and l_2 are made from 0.76" diameter (.068" wall thickness) high modulus carbon fiber tubes (45558-HM Rockwest Composites) to maximize the strength-to-weight



Figure 3.15: Various mechanical components of the 3-RSR leg including foot, knee, and driven link l_1 .

ratio of the links while ensuring leg inertia and mass is kept low.

3.3.2 Hip Design and Actuator Placement

The hip is constructed from two parts that are bolted together during assembly. The two parts have aligned bolt slots to allow actuators and motors of various width and size to fit within the structure and drive the leg. The hip was made adjustable so that the leg could be tested using direct-drive, quasi-direct drive, and series elastic actuators without having to fabricate three separate hip mounting brackets for each different actuator configuration which would account for 9 relatively costly components. Instead the two parts can be slid to the desired dimensions and bolted together to maintain that dimension when assembled on the leg. Several slots are made so that many bolts can be used to hold the two brackets together under large loads.

3.3.3 Foot Design

The sole of the foot is made of molded urethane rubber from SmoothOn. The rubber acts as a mechanical damper and shock absorber to filter out very high frequency ($> 500 \text{ Hz} \approx \omega_n$ the natural frequency of the rubber foot) impulse forces during landing from reaching the planetary-gears.

3.3.4 Mass Budgeting

The 3-RSR was mechanically designed to maximize strength-to-weight ratio of the unsprung mass and to minimize leg inertia. The 3-RSR has a total leg mass (hip and actuators included) of 2.5 kg (DD) or 3.1 kg (QDD) not including battery and electronics. The leg has an unsprung leg mass (m_l) of 0.63 kg, and a leg inertia of 0.015 kg-m². Each of the three actuators is composed of a 0.4 kg T-Motor U10 with a 0.2 kg Matex 1:7 single-stage planetary gear reduction in the QDD configuration (DD does not have the Matex gear). The QDD actuator mass budget (i.e. the ratio of actuator mass to total mass) is 48% (DD) and 58%(QDD), compared to Penn Minitaur's 40%, MIT Cheetah's 24%, where higher ratios are ideal for inducing dynamic behaviors [12].

Rather than using fasteners to join all 15 joints to their corresponding links, adhesive bonding was used to reduce component count and minimize inertia of the unsprung-mass. Joining between the aluminum and steel joints at the hip, knee, and foot is accomplished via adhesive bonding using Loctite Hysol E-120HP.

For proper carbon-fiber to aluminum adhesion, surface treatment on the metal is required and the finish of the carbon fiber must be cleaned and sanded to a fit with tolerance of 0.005" to 0.01". Surface treatment by means of abrading and applying an Alodine conversion coating is necessary to increase the surface energy of aluminum which is hindered by the oxide layer. Bond line thickness control is also critical as variations in thickness through the bond generates varying strain with higher peak stresses and thus premature failure. Once the aluminum surfaces are abraded the adhesive must be applied within minutes before an outer oxidation layer forms and reduces surface energy again. The Loctite Hysol E-120HP cures within 24 hours but can be heated to accelerate the curing.

3.3.5 Finite Element Analysis (FEA)

A finite element analysis (FEA) is conducted to determine the appropriate materials for each component in the leg. The carbon fiber tubes were chosen to maximize the strength to weight ratio. Carbon fiber is extremely resilient to bending moments and compression which are the primary loads acting on the leg segments. Due to the complexity and high cost of fabricating custom carbon fiber parts the legs joints were chosen to be metal and fabricated using CNC machining. The FEA results in Fig. 3.12 show that with applied normal force of 300 N in the direction indicated by the purple arrows, stresses as high as 123 ksi are present at the bearing support shaft. This indicates a safety factor of 4 in the case of a monopod hopper or of 1.2 in the case of a quadruped landing from a fall of 3 feet on a single leg. Similarly the most proximal segment of the knee joint also sees large stresses as a result of a straight offset also added for clearance purposes. The FEA for this component is shown in Fig. 3.13(a). This part is also chosen to be made from medium-carbon steel. The last component that was calculated to see high loads was the ankle link, in Fig. 3.13(b). To decrease stress the cross section of the beam extending from the carbon fiber tube of link 2 l_2 was

made larger. This allowed the material component to be made of aluminum which has a density of 2712 kg/m^3 which is roughly a third of the density and therefore mass of steel (7850 kg/m^3) [67].

3.4 Actuator Requirements for Omni-Directional Jumping

To select the appropriate combination of motor and single stage reduction, the required torque for desired static and dynamic motions must be determined. The required foot force for statically supporting the weight of the body indefinitely in stance is first calculated by

$$F_{stance} = \frac{mg}{n_{legs}} \quad (3.13)$$

where n_{legs} is the number of legs in stance.

The foot forces required to produce a vertical jump with desired peak height h_{peak} can be determined by first calculating the take-off velocity and then determining the leg and body CoM acceleration required to achieve the necessary take-off velocity.

$$E_k = \frac{1}{2}mv_{to}^2 = mgh_{peak} = E_p \quad (3.14)$$

where m is the robot's mass, g is acceleration due to gravity, and h_{peak} is the apex height reached during a jump. Solving for the initial take-off velocity v_{to} to achieve a desired jump height h_{peak} ,

$$v_{to} = \sqrt{2gh_{peak}} \quad (3.15)$$

Given a take-off velocity v_{to} to achieve a peak vertical height of h_{peak} the leg and COM acceleration a_{foot} can now be solved.

$$a_{foot} = \frac{v_{to}^2 - v_i^2}{2\delta z} \quad (3.16)$$

where $v_i = 0$ is the starting velocity of the foot which is assumed to be at rest, and δz is the leg extension range which is dependent on the vertical workspace of the leg topology. To calculate $\delta z = \delta l_{ext}$ I start at the fully contracted leg joint angle limits and end the jumping trajectory 50° before reaching the joint limits on the fully extended side. This provides a range of motion in the actuators of 130° and a vertical leg extension of $\delta l_{ext} = 0.3$ meters.

Finally, given a leg Jacobian J^T , calculate the required foot force and individual joint torques for jumping

$$F_{foot} = \frac{m(a_{foot} + g)}{n_{legs}} \quad (3.17)$$

$$\tau = J^T F_{foot} \quad (3.18)$$

where the Jacobian can be taken at the leg topology's position of weakest foot-force production. With the calculated joint torques required for jumping to a max height of h_{peak} , the appropriate

actuator design can ensue.

3.5 Quasi-Direct-Drive Actuator

An ideal actuator for dynamic legged locomotion that balances force transparency, torque density, high speed, energy efficiency, and mechanical robustness was determined by analysis in this thesis to be the quasi-direct-drive (QDD) actuator. This section describes the mechanical and electrical design in addition to the low and high level motor controllers developed for GOAT's custom DD and QDD actuator. Although DD is employed for GOAT, I argue that QDD is more optimal for purposes of energy efficiency and real world feasibility of legged robots at the marginal cost of slightly lower force control bandwidth and proprioceptive sensing accuracy.

3.5.1 Mechanical Design

The custom QDD used on GOAT consists of 4 major components: a Tiger U10 brushless DC motor, a variable motor bracket/housing which allows different Tiger motors and gearboxes to be used, a single-stage planetary gear box, and ball-bearings on the motor's output for double support to handle large radial and moment loads acting on the rotor.

Although QDD offers advantages in energy efficiency by conserving a factor of n^2 power for a given torque production, the GOAT actuator was designed to be configured as QDD or DD in which no gearbox is used. Performance tests on the T-motor U10 indicated that these motors in direct-drive mode are capable of producing sufficient torque at speed (i.e. power) to induce explosive jumping given the minimized weight and inertia of the leg design. Therefore, both DD and QDD actuation schemes will be experimentally tested on the GOAT leg.

Motor

Motor selection to drive the QDD or DD actuator was based on maximizing thermal specific torque. It was determined in [12] that the T-motor U8, and more generally the U-Power Series, had superior torque density as compared to other commercial off-the-shelf (COTS) motors. The Maxon EC-90 Flat was considered because of the convenience in using a Maxon based motor driver but the torque density of this motor, due mostly to added mass from a fully enclosed stator housing/frame, was not sufficient. Therefore, a Tiger motor U10 was chosen.

Transmission

To increase the torque density of the GOAT leg's actuators, a single stage gear stage can be placed between the motor and the drive hip link. In previous sections it was shown that adding a single stage gear transmission, specifically a single-stage planetary, would decrease energy requirements for



Figure 3.16: The Tiger Motor U10 shown here has a large 40 mm gap radius and a lightweight frame. The T-motor U8, U10, and U12 were determined to have one of the highest thermal specific torques of any COTS motor ($0.42 \frac{Nm}{kgC^\circ}$ at $r_{gap} = 40 \text{ mm}$) [43]. For reference the custom MIT cheetah motors have a thermal specific torque of $0.71 \frac{Nm}{kgC^\circ}$ at $r_{gap} = 49 \text{ mm}$ [9].

generating a desired torque by allowing the motor to operate in a more efficient regime with lower current and thus lower Joule heating losses and less saturation from thermal management or RMS limiting. A single stage planetary transmission was shown to mitigate many of the common negative effects of geared transmissions as it is able to maintain a bandwidth of 40 Hz and proprioceptive torque sensing within 6% error.

Housing

The adjustable housing of the actuator also serves as part of the hip structure in the 3-RSR leg design. The 2-piece actuator mounting brackets can be seen in Fig. 3.17. The housing consists of two components which allow the motor to be bolted on to one end while the link 1 bearings are press fit into the other end. This design allows the motor rotor and link 1 to be double support (o.e. support from both sides) for higher radial load rating.

3.5.2 Electrical Design

Three printed circuit boards are used for the total actuator module. The module includes a motor driver board based off a TI Piccolo TMS320F28069M MCU and a DRV8301 Bridge Driver which drives 6 N-channel Vishay SUM110N06-05L 60 V MOSFETs with 175°C temperature limit. This board is responsible for running the low level motor commutation and PID controllers for separate position, velocity, and torque control at 10 kHz. The board has a built in AMS AS5048A magnetic encoder which senses the change in magnetic field from a diametrically polarized magnet connected

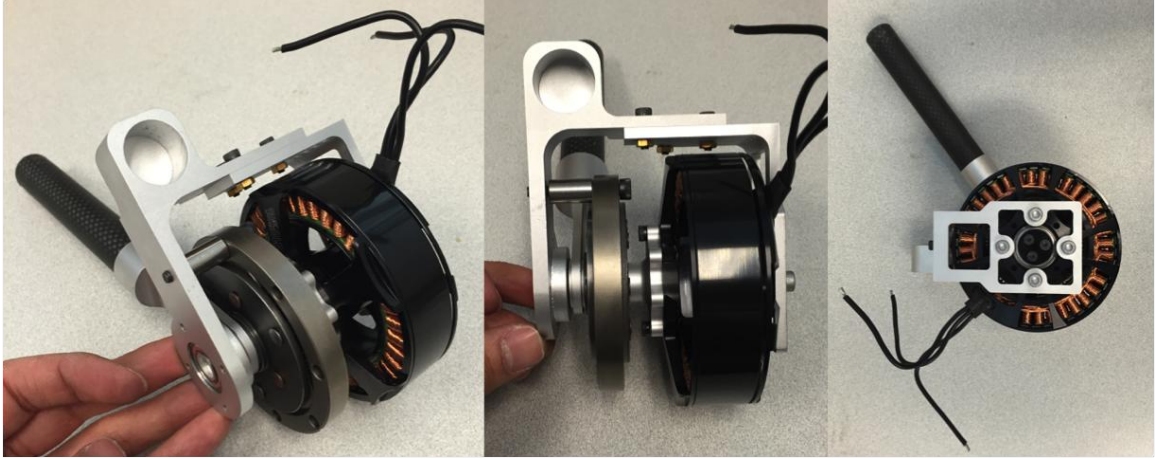


Figure 3.17: The quasi-direct-drive actuator module driven by a T-motor U10 with a single stage Matex 1:7 planetary gear stage.

to the axle of the rotor. The second custom board is currently a modified Hebi prototyping I/O board with various input/output channels including SPI, I2C, Serial, and Ethernet. This board is designated for communications and data transfer/exchange between the motor controller board and a main computer sending high-level commands. The third board is a small encoder board placed on the output side of the actuator to measure absolute output angle using the same AMS AS5048A magnetic encoder and sensing the magnetic field of a permanent magnet in the shaft of the driven output link 1. This is needed when the actuator is configured in QDD mode to have knowledge of absolute output position after the gear stage.

The power electronics are capable of energy regeneration to convert work done on the leg back into battery potential for added efficiency. The exact mechanical to electrical energy conversion was not measured but for reference the MIT Cheetah’s custom electronics achieve 63% energy efficiency during this conversion [9].

3.5.3 Actuator Control

Optimal Motor Commutation: Field Oriented Control

A custom motor controller was required for the desired control of the brushless DC Tiger U10 motor. COTS electronic speed controllers used to power similar motors for quadrotors use back-EMF or hall effect sensors to electronically commutate the motor and cyclically energize the motor windings. These off-the-shelf ESC’s are designed for velocity control and driving brushless motors at high speeds in a single direction. They are inadequate for direct-drive application requiring precise position and torque control over the entire spectrum of rotor velocities.

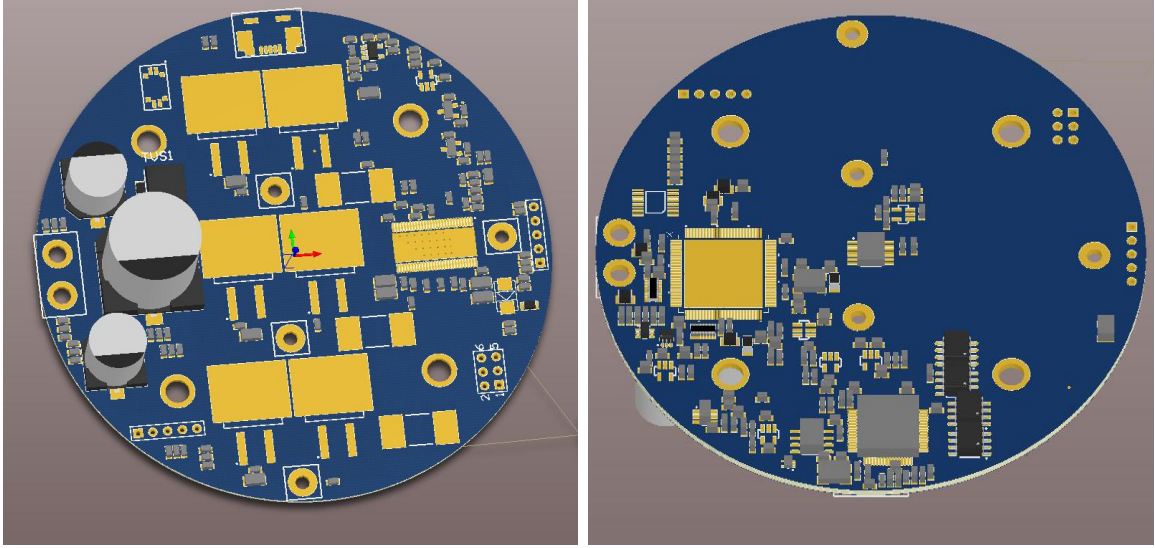


Figure 3.18: Custom GOAT motor driver configured with a Piccolo TMS320F28069M MCU and a DRV8301 Bridge Driver which drives 6 N-channel Vishay SUM110N06-05L 60 V MOSFETs with 175°C temperature limit.

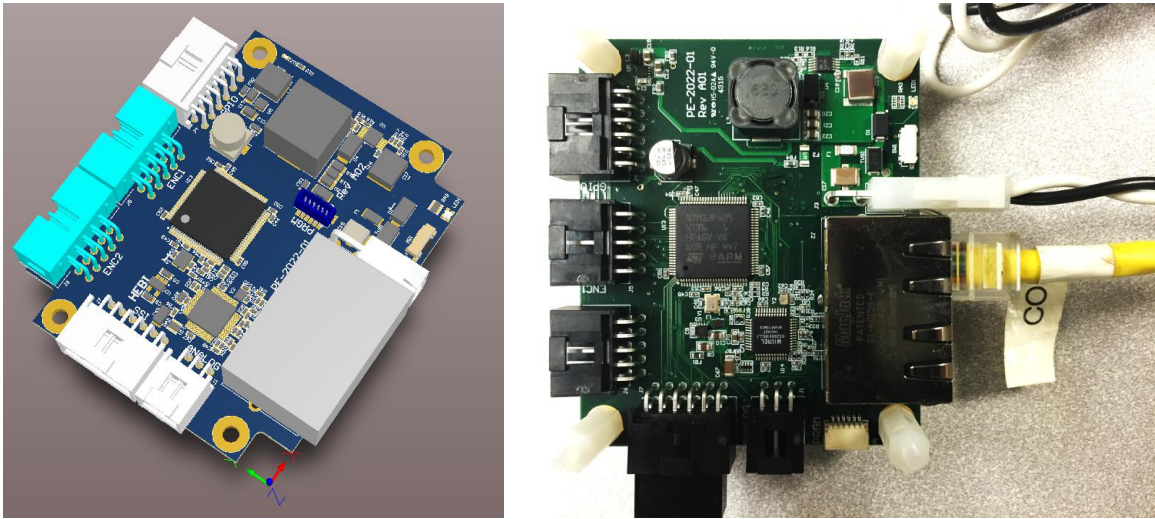


Figure 3.19: The custom Hebi Robotics communications board outfitted with a 32-bit ARM Cortex processor, Ethernet switch, and SPI port among other I/O ports for prototyping.

The main methods of brushless motor commutation are 6-step square wave, sinusoidal, and field-oriented control. Of these three, 6-step square wave is the simplest – using only a look-up table based on feedback from 3 hall effect sensors placed on the stator used to determine the rotor position sextant. Based on the electrical angle of the rotor six hall effect states can exist, in which one phase winding sources current, one sinks current, and one is neutral. Each hall-effect state corresponds to

Electrical Angle [$^\circ$]	Hall Effect State	Phase A	Phase B	Phase C
0-60	{0,0,1}	+	-	neutral
60-120	{0,1,1}	+	neutral	-
120-180	{0,1,0}	neutral	+	-
240-300	{1,1,0}	-	+	neutral
180-240	{1,0,0}	-	neutral	+
300-360	{1,0,1}	neutral	-	+

Table 3.3: Lookup table for six-step square commutation [47].

a specific energizing state for the three phase windings according to Table 3.5.3 [47].

Alternatively, sinusoidal commutation energizes the 3 windings with 3 identical sinusoidal waves phase shifted apart from one another by 120° electrical. Each sinusoidal phase current is generated by pulse width modulation (PWM) from the motor controller. This creates a N/S electromagnetic field that rotates within the motor core. Sinusoidal commutation reduces torque ripple and cogging as compared to 6-step square wave but it requires finer angular position feedback of the rotor for direct-drive position controlled applications. Therefore, an encoder is needed to get precise rotor angle feedback. Sinusoidal commutation would theoretically produce maximum torque at every rotor angle without ripple or cogging if current was in phase with voltage.

Field-oriented control (FOC) or vector control is the most complex commutation method and it closes the feedback loop on motor current rather than voltage to address the issue of current lagging being the commanded phase voltages which is an inherent effect of the motor's inductance. This is explained by a simple motor model which is composed of a speed dependent voltage source (i.e. back-emf) in series with a resistor and inductor. For a 3-phase motor the resistance is the resistance of each phase winding and the inductor is the inductance caused by the winding coils which naturally opposes change in current and thus causes a phase-shift between commanded voltage sinusoid and the current response.

Because a magnetic field is generated by current flowing through a coil (not voltage), and current is out-of-phase with voltage in AC circuits, the torque (via current) is out-of-phase from the voltage will be less than optimal at any given rotor angle.

Fig. 3.20 from [56] shows the magnetic force and torque production for three different phase alignments of the rotor's permanent magnet and the stator's electromagnetic fields. In the non-optimal case the magnetic force is made up of two components of which only one is acting to produce torque. The larger the phase shift between the voltage and current, the larger the component of the magnetic force that pulls outward (direct current) in comparison to the component which produces torque (quadrature or Torque current). This phase-shift not only decreases torque but wastes power and increases torque ripple.

Therefore, FOC measures the two components of current, direct I_d and quadrature I_q , and

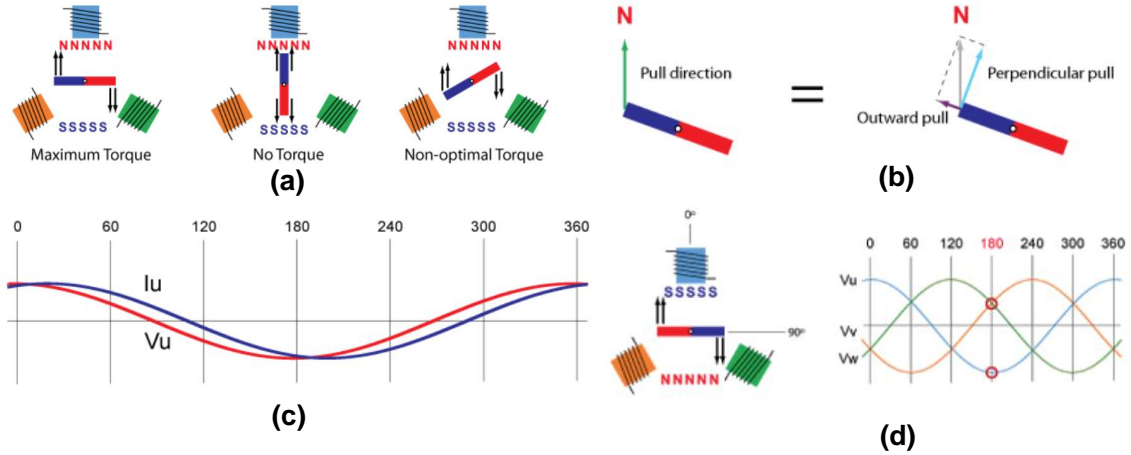


Figure 3.20: (a) is a simple motor model showing torque production for three different phase alignments of the rotor’s permanent magnet and stator’s electromagnetic fields. (b) shows a decomposition of magnetic force or pull direction into two components: one that produces torque and one that pulls outward and wastes energy. The purpose of FOC is to continuously apply a magnetic field in the stator windings which converts all the magnetic force into the component that produces torque. (c) shows the phase-shift that exists between phase winding voltage and phase current, which is around 20° here. (d) shows the commanded voltage sinusoids vs. electrical angle and the corresponding magnetic field produced by the energized windings. Figure source: [56].

adjusts the voltage phase to minimize I_d and maximize I_q for maximum torque production. This control is achieved by closing the loop on current via sensing of the AC current on two of the three phase windings⁵. The three AC phase currents are then transformed using the Clarke and Park transformations with encoder feedback to measure the direct and quadrature current, I_d and I_q , in the rotors rotating frame. Transforming AC phase currents i_a , i_b , and i_c into DC I_d and I_q simplifies the PI control around current because the DC currents have significantly less time-variation and aren’t cyclic and sinusoidal [56]. Two PI controllers then modulate the phase and voltage applied to each phase winding so the commanded I_d and I_q current are achieved. For the GOAT actuator I_q is set to zero to maximize the torque production of the motor at low speeds. I_q is sometimes increased from zero in order to reach very high operating speeds. Fig. 3.21 from [56] is a simplified schematic of how the PI controller modulates the PWM voltage signal so that direct current is eliminated and quadrature current is maximized to reach the desired torque. In addition to maximizing torque output, FOC minimizes torque ripple, cogging, energy loss, and Joule heating due to flux current used to pull the rotor outward rather than produce torque.

A step by step algorithm on how to implement the well known FOC method is now briefly described according to [68]. The algorithm references variables found in Fig. 3.22.

⁵the third phase current is calculated from Kirchoff’s current law (KCL) for wye-configured windings

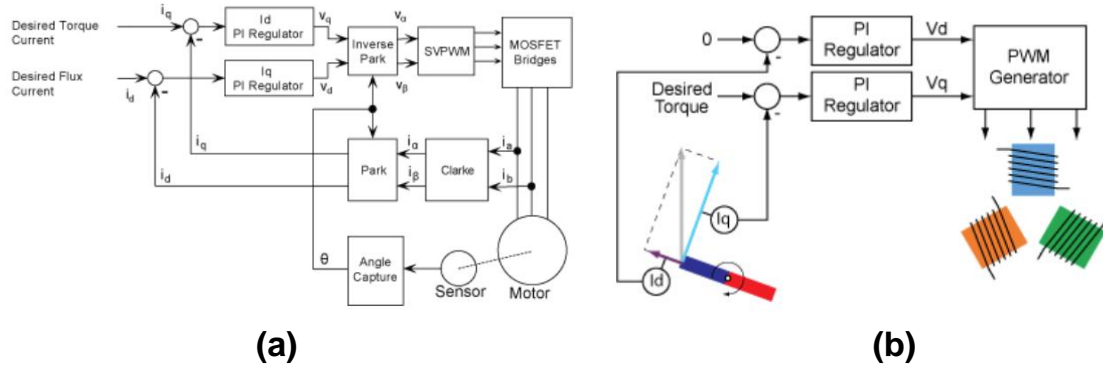


Figure 3.21: (a) is a flow chart showing the FOC commutation. (b) is the control strategy which minimizes I_d and maximizes I_q . Figure source: [56].

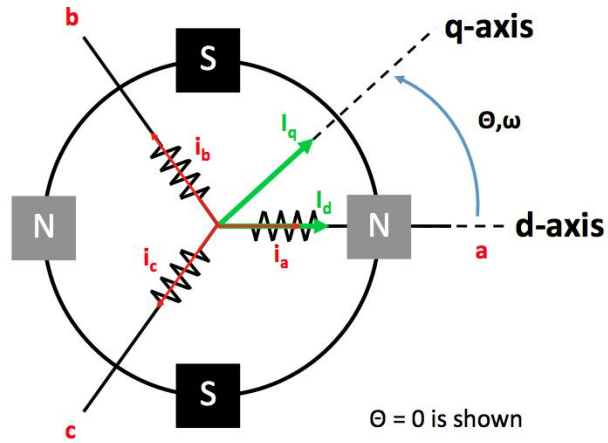


Figure 3.22: Representation the input (a, b, c) winding reference frame and the rotating $d-q$ frame for a 4-pole brushless motor.

Algorithm 1: Field Oriented Control [68]

-
- 1: **procedure** FOC($I_{q,cmd}, I_{d,cmd}$)
 - 2: Measure the 3 stator phase currents convert them to complex state space vector (a,b,c) coordinate system
 - 3: Current vector is converted to (α, β) 2-axis **stationary** coordinate frame using **Clarke Transform** where i_a, i_b, i_c are the time varying AC currents of each stator winding.
-

$$\mathbf{I}_{\alpha,\beta,\gamma}(t) = T i_{a,b,c}(t) = \frac{2}{3} \begin{bmatrix} 1 & -\frac{1}{2} & -\frac{1}{2} \\ 0 & \frac{\sqrt{3}}{2} & -\frac{\sqrt{3}}{2} \\ \frac{1}{2} & \frac{1}{2} & \frac{1}{2} \end{bmatrix} \begin{bmatrix} i_a \\ i_b \\ i_c \end{bmatrix} \quad (3.19)$$

and if i_a is superimposed and aligned with I_α and a wye winding configuration is used such that $i_a + i_b + i_c = 0$ then the transform is simplified to

$$I_\alpha = i_a \quad (3.20)$$

$$I_\beta = \frac{1}{\sqrt{3}}(i_a + 2i_b) \quad (3.21)$$

- 4: Use the **Park Transform** to transform the (α, β) **stationary** reference frame to (d, q) , the **rotating** reference frame. The coordinate frame is aligned such that the d-axis passes through a north rotor PM pole and the q-axis is 90° electrical (defined by PM poles) in the direction of rotation or applied torque. For example a 2 pole motor the q-axis is displaced 90° mechanical from the d-axis of the rotor; for a 4 pole motor it is displaced 45° mechanical from the d-axis.

$$I_d = I_\alpha \cos \theta + I_\beta \sin \theta \quad (3.22)$$

$$I_q = I_\beta \cos \theta - I_\alpha \sin \theta \quad (3.23)$$

where I_d is the flux/outward pull component of current and I_q is the torque producing component of current.

- 5: Run a PI controller on the commanded currents $I_{q,cmd}, I_{d,cmd}$ in this d-q rotating frame.
- 6: The PI controller modulates the voltage components in the d-q rotating reference frame, therefore it must be converted back to reference voltage wave forms in the stationary (a, b, c) frame. First use the **Inverse Park Transform** to transform d-q currents to the stationary $\alpha - \beta$ reference frame by

$$V_\alpha = V_d \cos \theta - V_q \sin \theta \quad (3.24)$$

$$V_\beta = V_q \cos \theta + V_d \sin \theta \quad (3.25)$$

- 7: Penultimately use the **Inverse Clarke Transform** to convert back from orthogonal 2-axis frame (α, β) to 3-phase stator frame (a, b, c) .

$$V_a = V_\alpha \quad (3.26)$$

$$V_b = \frac{1}{2}(-V_\alpha + \sqrt{3}V_\beta) \quad (3.27)$$

$$V_c = \frac{1}{2}(-V_\alpha - \sqrt{3}V_\beta) \quad (3.28)$$

- 8: Finally, using PWM apply the 3-phase voltages (V_a, V_b, V_c) to generate the commanded currents and thus torque while accounting for the voltage-current phase-lag due to motor inductance.
-

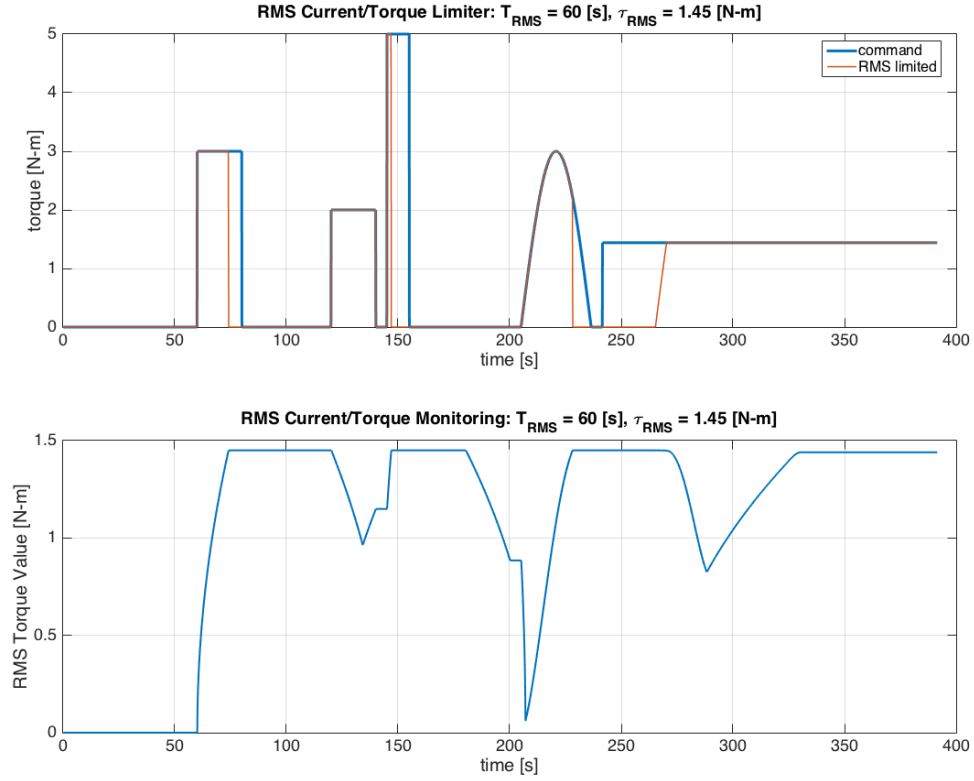


Figure 3.23: Output of the RMS current limiter which monitors the RMS current and saturates the commanded output torque when necessary to remain within the motor winding's thermal limits.

Thermal Management and Control

The current system was experimentally determined to be thermally limited by the thermally limiting hardware on the bridge driver board which saturates the FETs at 150°C. Once the FETs reach their thermal limits the bridge driver saturates current to the phase windings. With the current hardware the bridge driver reaches higher temperatures than the motor windings. The future, custom designed, motor driver board will integrate a finned heat sink on each FET to increase surface area for unforced convection which will dissipate heat faster. Additionally an aluminum plate can be added to the underside of the board to sink heat from both sides.

To maximize performance yield from the T-motor the motors are not limited by voltage but rather by an RMS current monitor which tracks the RMS value of the current history and saturates the current output commanded to the motor if the RMS value exceed the continuous rated current. The RMS current limiter ensures in a round about way that thermal limits of the windings are not exceeded. While thermal modeling and feedback using a thermocouple on the stator winding

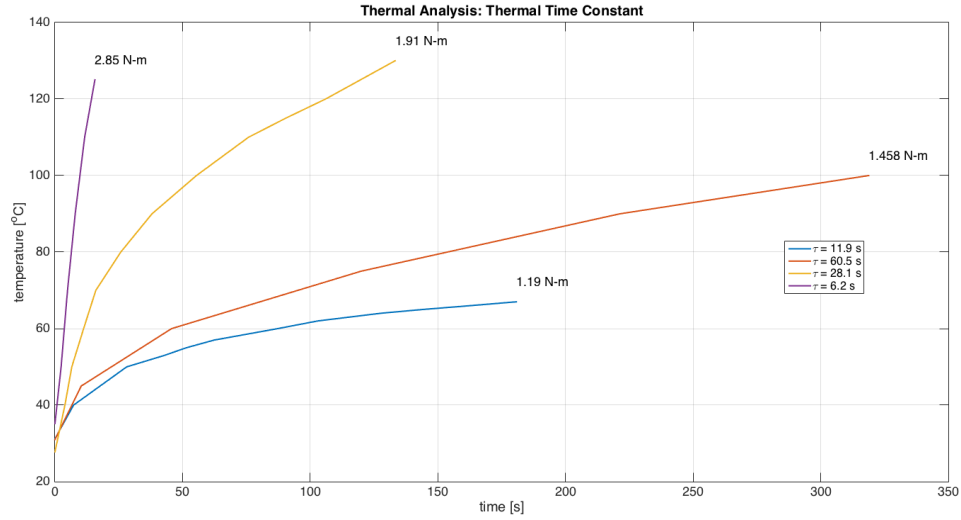


Figure 3.24: Thermal analysis showing the time response in winding temperature to 4 commanded torques ranging from 1.19 N-m to 2.85 N-m with associated thermal time constants. Thermal time constant was calculated by 63% of the time taken to reach steady-state. If steady state was not reached the maximum temperature was used. A FLIR E40 Infrared Thermal Imaging Camera was used to collect real-time temperature data on the windings.

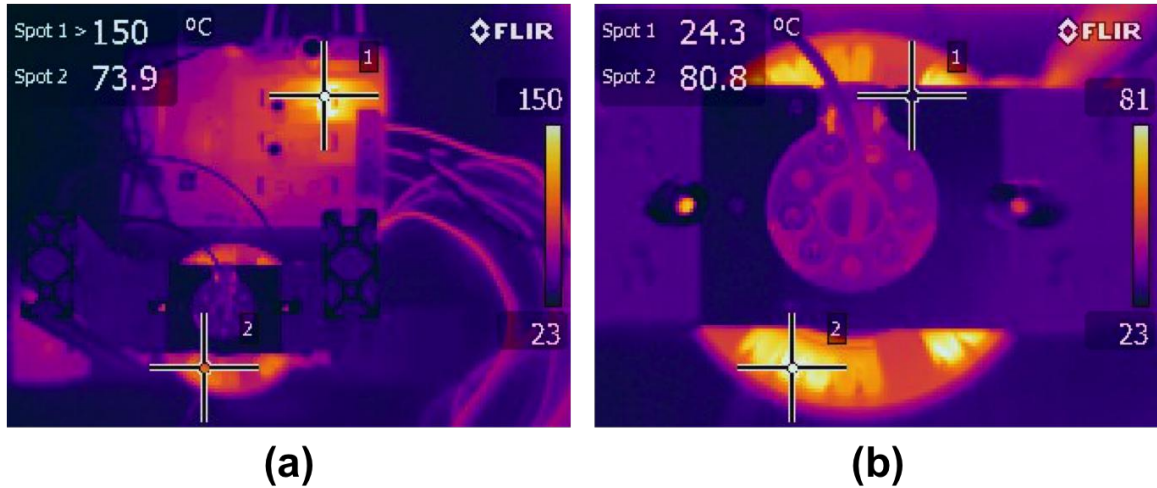


Figure 3.25: A FLIR E40 Infrared Thermal Imaging Camera was used to observe the temperature gradient over the motor windings and the PCB containing the motor driver FET bridges. (a) is a top-view IR image of the torque test rig with the motor driver PCB (cursor 1) and the T-motor (cursor 2). (b) shows a closer view of the T-motor U10. The thermal image depicts which stator winding poles are being energized and the temperature at those windings.

would be more accurate, it is also more complex and requires outfitting the motor with additional

sensors and ensuring those sensors remain operational. RMS current limiting requires not additional sensors beyond current sensing which is already needed for motor commutation. Additionally, for thermal modeling multiple temperature sensors placed around the stator windings must be used to accurately measure max winding temperature as some windings may be highly energized while other are not (as seen in Fig. 3.25) which may lead cause the thermal management system to fail in saturating current when necessary.

A thermal analysis was conducted to measure the time response in winding temperature to 4 commanded torques ranging from 1.19 N-m to 2.85 N-m from which the associated thermal time constants were determined. Thermal time constant was calculated by 63% of the time taken to reach steady-state. If steady state was not reached the maximum temperature was used. A FLIR E40 Infrared Thermal Imaging Camera was used to collect real-time temperature data on the windings. The thermal time constant for 1.3 times and 2 times the continuous rated current was determined to be 28.1 and 6.2 seconds respectively. Therefore, to match the thermal profile of the T-motor the RMS current limiter was set to have a history window or period of 60 seconds and a continuous rated current of 1.45 N-m. The time window over which RMS is calculated (60 s) was chosen based on thermal tests using thermal camera, Fig. 3.25, and watching how long it took the windings to reach their thermal limits at different constant torque values. The RMS period was calculated so that it matched the thermal time constant and would saturate the signal right before the windings reached their thermal limits. If the RMS period is set to be too long there is a risk of burning out the motor due to excessive Joule heating which melts the winding insulation. The T-motor uses class F insulation which is rated at 100°C rise from ambient or an absolute operating temperature of 155°C.

Communications

The T-motor DD and QDD actuator module run custom low level firmware for FOC commutation at 25 kHz and the PID loops for separate position, velocity, and torque control at 10 kHz all on board a TI Piccolo TMS320F28069M micro-controller unit (MCU).

The schematic in Fig. 3.26 shows the communications layout of the hardware. High level commands and the motion planner are computed in real-time on a lap-top computer using MATLAB. Position, velocity, and torque commands and associated gains are sent at 1 kHz over 100 Mbps Ethernet using TCP/IP to a communications board. The communications board manages data transfer between the lap-top and the Motor Driver board. The comm board uses a 32-bit ARM Cortex processor to handle Ethernet communications and SPI transfer. The SPI protocol is used to communicate between the Comm board and the TI motor driver. This data transfer line passes commands and sensor feedback between the TI motor controller and the laptop. The motor driver is a TI 3-phase brushless DC motor driver running on a Piccolo MCU with a DRV8301 bridge driver. Custom firmware is uploaded onto this board to drive the T-motor using position, velocity, and

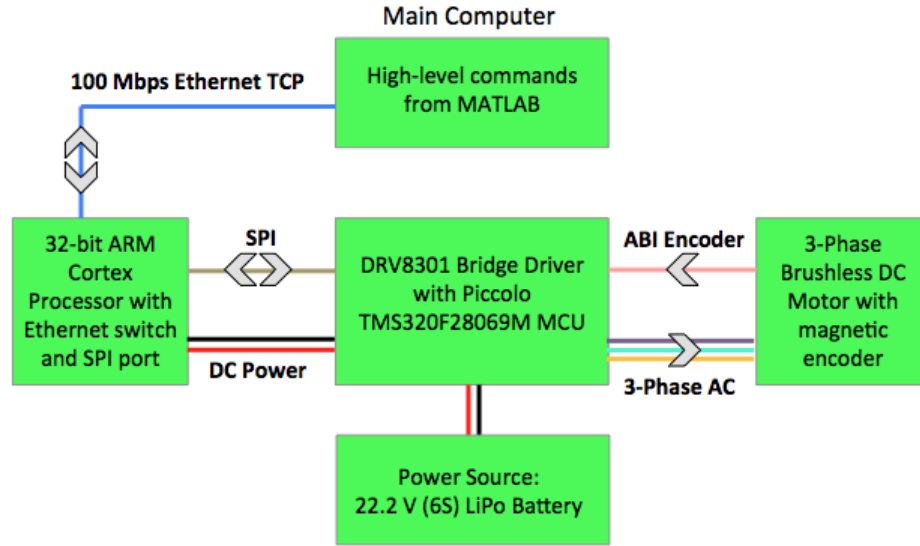


Figure 3.26: Schematic wiring diagram of the electronics for a single GOAT actuator.

torque commands. The motor driver then inverts the DC power into an AC power which is sent to the 3-phase motor. A custom PCB with integrated magnetic encoder reads a diametrically polarized permanent magnet coupled to the rotor and relays this feedback to the TI board over ABI.

Calibration

Calibration of the T-motor was accomplished using the same 1-axis SRI M2210E torque load cell. From the calibration the motor's torque constant was determined as well as the control constant which is an internal value in the custom created Matlab API for commanding the motor.

Figure 3.27 shows a torque vs current plot of the motor the torque constant to be $0.072 \frac{N-m}{A}$. The magnetic flux in the motor core begins to saturate at 70 A and the thermal limits of the motor driver half-bridges reach their thermal limits between 75-80 A. The shaded color zones indicate allowable duty time and duration of holding torque. The green region indicates infinite holding as this region is within the continuous current and thermal limits of the motor; green-yellow corresponds to duty times ranging from 5 minutes to 20 seconds; yellow indicates short duty cycles of up to a few seconds; orange indicates duty cycles less than 1 second; and red indicates peak instantaneous torques with a duty cycle of a few milliseconds.

The calibration with the MATLAB API motor controller was found to be $0.103 [N-m/Unit]$ using data from the plot in Fig. 3.28. The colored regions in Fig. 3.28 correspond to the same operating regimes as those described for Fig. 3.27.

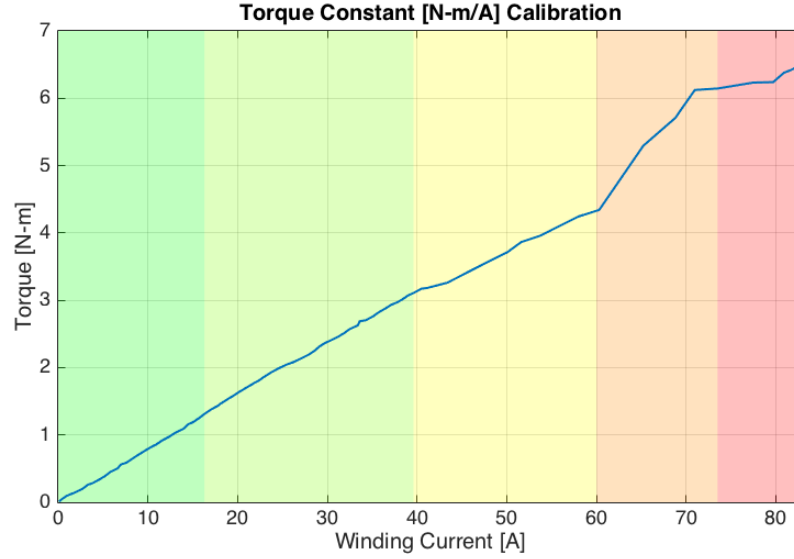


Figure 3.27: A torque vs current plot of the motor shows the torque constant to be $0.072 \frac{N-m}{A}$. The magnetic flux in the motor core begins to saturate at 70 A and the thermal limits of the motor driver half-bridges reach their thermal limits between 75-80 A. The shaded color zones indicate allowable duty time and duration of holding torque. The green region indicates infinite holding as this region is within the continuous current and thermal limits of the motor; green-yellow corresponds to duty times ranging from 5 minutes to 20 seconds; yellow indicates short duty cycles of up to a few seconds; orange indicates duty cycles less than 1 second; and red indicates peak instantaneous torques with a duty cycle of a few milliseconds.

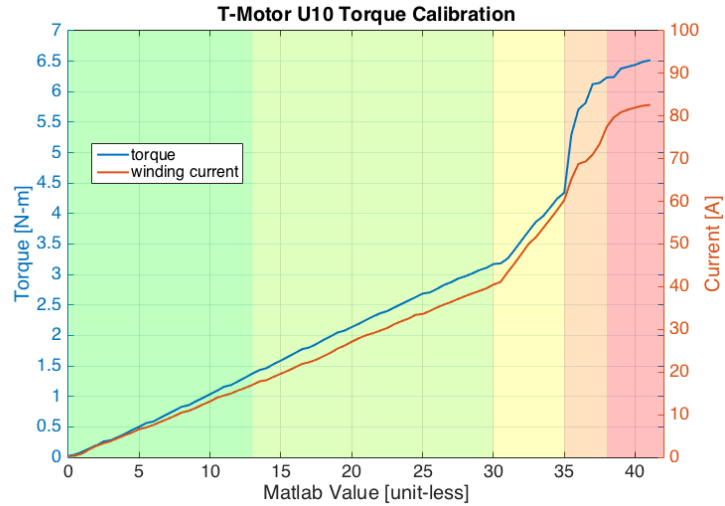


Figure 3.28: Torque calibration to determine the relationship between the commanded value in the custom motor-controller Matlab API.

3.6 Sensing

Beyond motor current sensing there are six 14-bit on axis magnetic rotary position encoders (Austria Microsystems AS5047P) mounted on a custom PCB of which three are used for motor commutation and mounted to the back of the T-motor U10 stator frame. The AMS AS5047P magnetic encoder chip is able to operate within close proximity to the motor (considering the strong time-varying magnetic field generated by the motor) by canceling out all external magnetic fields (where 'external' refers to any magnetic field not created by the diametrically polarized magnet fixed to the rotor shaft) by built-in magnetic immunity. This immunity is achieved by using 4 hall sensors within the encoder chip with software that uses two pairs of differential measurements to calculate the magnetic field of the encoder magnet which relates to rotor angular position. Therefore, any external magnetic fields existing are canceled by the differential measurement using the reasonable assumption that any external fields will have the same field strength on all 4 hall sensors which are very closely spaced in comparison to the size of the motor [69].

The other 3 are placed on the actuator housing and measure the angular position of the output shaft in the case a gearbox is used. The output of the actuators are rigidly coupled to their respective link 1's l_1 . The encoders used for motor commutation are placed 2mm axially from the diametrically polarized permanent magnet which is mounted to the rotor axle. Similarly, three diametrically polarized permanent magnets are embedded in link 1 (l_1) on the motor output axis at a distance of 2 mm from the encoder located on the output side of the actuator housing. The encoder has a resolution of 0.08 degrees ($\frac{360}{2^{14}}$), communicates over SPI to an Arduino which uses an Ethernet shield to transfer data to Matlab environment with real time feedback at 1 kHz.

3.7 Experiments

3.7.1 Complete System

For preliminary testing the GOAT leg is constrained to a 1-DoF test rig using a 15.5 mm wide linear bearing and guide rail. This setup only allows the leg to move in the vertical direction. All electronics and power are mounted off-board currently, although the custom electronics described previously are currently being developed for on-board mounting. The electronics and battery are expected to add a mass of 1 kg (0.75 kg for battery and 0.25 kg for electronics). Figs. 3.31 and 3.32 show the complete GOAT leg mounted on the 1-DoF test rig. A video of preliminary experiments introducing the GOAT leg demonstrating virtual compliance, hopping, explosive jumping, and omni-directional running trajectories can be found here: <https://www.youtube.com/watch?v=n319xVomJTQ>.

The full leg mechanism was tested to determine the mechanical friction present in the system. Equal joint torques were commanded at each of the three hip actuators starting at zero and increasing until motion in the leg was seen. The torque at each actuator was found to be around 0.063 N-m

when the leg began to move. This is compared to the static friction in each motor of around 0.048 N-m indicating minimal added friction in the actual mechanism. This can be attributed to the high quality bearings composing each of the 15 joints and the use of shims between all surfaces with any sliding contact. This equates to approximately a 1 N force at the foot which means that forces less than 1 N would be difficult to measure using proprioception through motor current. There is however some backlash in the mechanism – in the clevis joint and in the ankle joints — which could not be easily removed even with the use of shims between sliding surfaces. Although this can be most likely be improved by higher machining tolerances, the sub-1-mm backlash in the system seems negligible in terms of its effect on the performance of jumping and landing using virtual compliance.

3.7.2 Omni-Directional Force Vectoring with Force Plate

In section 3.2 the 3-RSR topology was shown to be superior in terms of requiring the least amount of joint torque per actuator to generate omni-directional force-torque wrenches. To experimentally validate that the 3-RSR could, in fact, deliver force equally well in all vectors in the frontal plane as it could in the sagittal plane a test which commanded the leg to generate 18 force-torque wrenches defined by eq. 3.12 where θ ranged from 0 to 360 in increments of 20 degrees while on a 1-DoF test rig. The resulting data, Fig. 3.29, collected by a 6-axis AMTI OR6-7-2000 force-torque plate show that the magnitude of force produced in the x direction is equal to the magnitude of foot force produce in the y direction. This indicates that the 3-RSR is capable of generating foot forces out of the sagittal plane equally as well as it can generate force in the sagittal plane. This is done using less torque in the 3-RSR leg than in other topologies while also demonstrating enhanced experimental mechanical robustness in delivering out-of-sagittal plane forces.

3.7.3 Omni-Directional Running

To test omni-directional running and walking ability, the GOAT leg was fixed on a 1-DoF test rig so that the foot could not touch the ground. The foot was then commanded through a minimum jerk spline trajectory for omni-directional running. The leg was able to reach high running speeds with a stride length of 0.25 m at 2.4 Hz. A video showing seamless changes in running direction as well as high speed running trajectories can be found here: <https://www.youtube.com/watch?v=n319xVomJTQ>.

3.8 Summary and Design Insights of the GOAT leg

This section highlights and summarizes the key design insights and advantages that the novel 3-RSR GOAT leg offers with respect to other, more common, leg topologies. The GOAT leg

1. **seems (from preliminary experimentation) to be relatively mechanically robust to large 3D forces and even large falls. The leg was never broken during any of the**

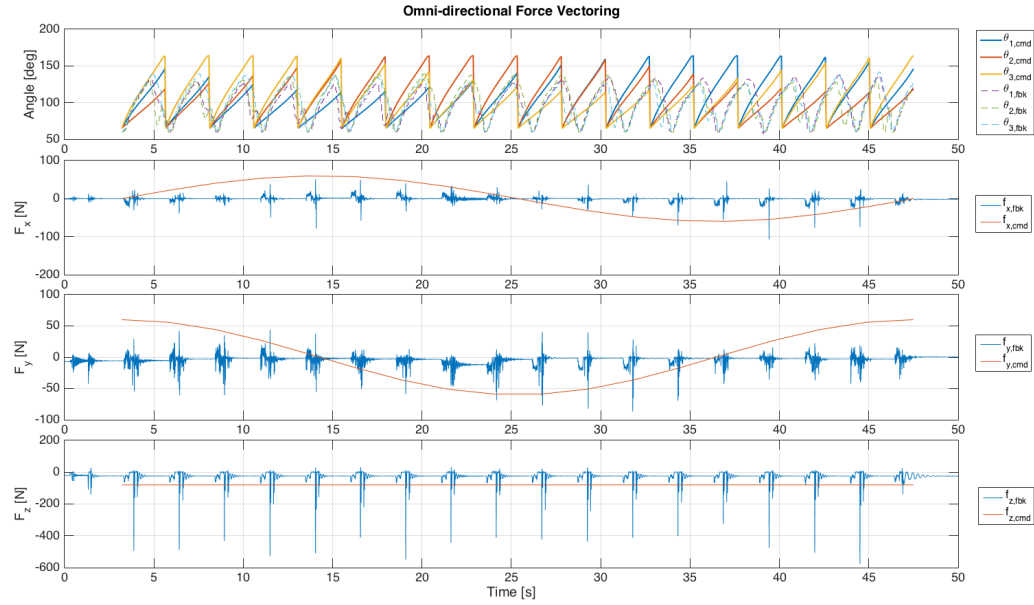


Figure 3.29: Data from the 6-axis force-torque load cell was collected to determine the ground reaction forces generated at the foot of the robot. The commanded and actual forces are presented. The data shows that the leg can produce equal forces along all vectors of the frontal plane (i.e. any combination of F_x and F_y within the actuators limits). This corresponds with the analytical data presented in Figs. 3.6 and 3.7.

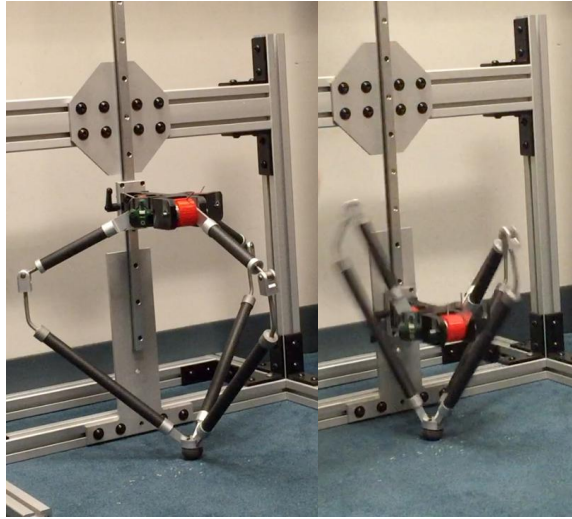


Figure 3.30: Passive landing tests were performed using 3 COTS torsion springs ($k_s = 4.11 \frac{N-m}{rad}$) in the 3 hip R-joints. The left image shows resting knee-below-hip position while the right image shows the 3-RSR knee-above-hip configuration absorbing energy upon landing.

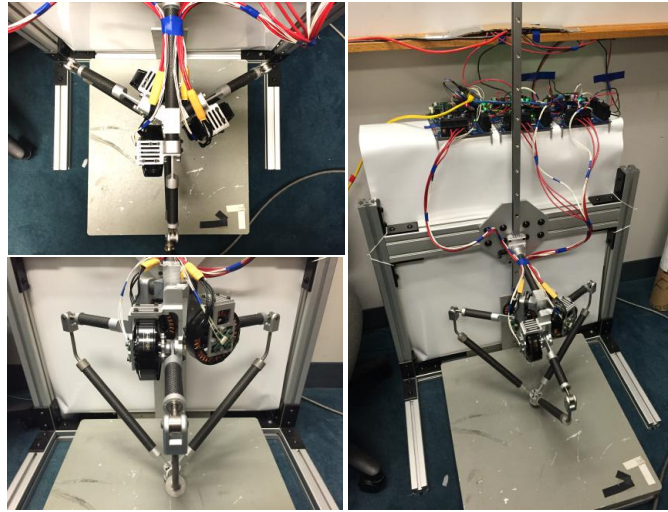


Figure 3.31: GOAT Leg prototype with T-motor U10 actuators mounted in direct-drive configuration.

high jumping, landing, and hopping tests.

2. was analytically and experimentally shown to be capable of generating omnidirectional force-torque wrenches at the foot with less required torque per actuator than the other leg topologies.
3. requires less torque per actuator and distributes foot loads over multiple actuators enabling the use of direct-drive and quasi-direct-drive actuation to achieve both explosive power and high fidelity proprioceptive force sensing for virtual compliance.
4. has optimized leg parameters which increase its workspace to encompass most of the required workspace for legged locomotion including walking, running, and jumping.
5. has very low limb inertia as compared to all current legs as all the actuators' stators are static and fixed to the hip frame. This means that the mass of the actuators does not contribute to the inertia of the leg like in the MIT Cheetah and other serially configured designs.

The GOAT leg has proven itself to be a mechanically robust 3D parallel mechanism with 3 degrees of freedom which allow it to exert force equally along any vector in the frontal plane with less required torque than would be required by the prismatic, series articulated, and parallel planar

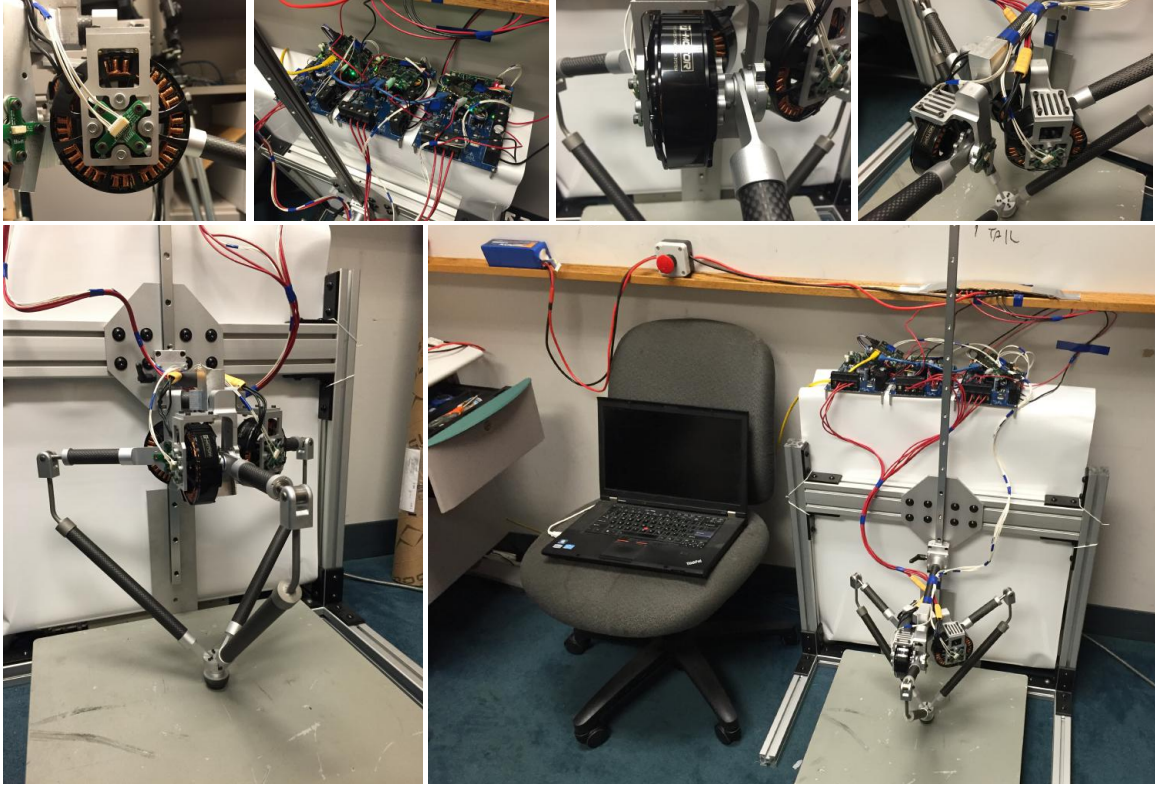


Figure 3.32: GOAT Leg prototype and experimental 1-DoF vertical jumping test bed. Electronics and power (LiPo battery — blue) are both shown in the bottom right image off-board, as tested. The gray ground plate the robot is standing on is a 6-axis force-torque load cell.

topologies⁶. While series-articulated limbs can use one large actuator at the knee⁷ for sagittal plane jumping and tilt the entire leg to produce out-of-plane forces, the leg structure is, similarly, not designed to bear high lateral forces. Additionally, for the series-articulated and prismatic limbs to produce forces at vectors which do not pass directly through the hip joint, much larger torques from the hip abduction/adduction actuator as well as the hip flexion/extension actuators are required. Therefore, if these actuators are made small — assuming the knee actuator will bear the brunt of the loads required for jumping — then the prismatic and series articulated leg topologies would be much weaker in producing omni-directional force vectors at any spot within their workspace as compared to the 3-RSR GOAT leg.

Also, by relying on a single actuator to carry the load for jumping as done in the prismatic and

⁶The parallel planar topology in ATRIAS is only extended to the third dimension using an abduction joint and thus the parallel mechanism portion of the leg is planar while the entire leg is made spatial. The fact that the parallel mechanism is planar makes ATRIAS' legs very susceptible to failure due to lateral (or out of sagittal plane forces).

⁷the knee joint actuator is responsible for leg extension/thrust while the hip actuator is responsible for leg angle swing. This decoupled actuation is inherent to both series-articulated limbs and prismatic limbs

series-articulated limbs, that actuator must almost certainly be outfitted with a transmission to produce required torques/forces. This comes at the sacrifice of an unequally distributed proprioceptive force sensitivity from each actuator. Therefore, it is important to note that a parallel leg topology which distributes foot loads over multiple actuators does not need to sacrifice proprioceptive sensing accuracy (by adding a transmission) for agility.

While the GOAT leg will most likely never be faster than the very impressive speeds achieved by the MIT Cheetah in running along a straight line, the design of GOAT sacrifices 1D top speed for the potential to run and jump in all 3 dimensions with more agility than the MIT Cheetah and all other dynamic legged robots to this date. The design of legged robots at this point is clearly task optimized and as such it is not entirely fair to compare the GOAT leg to the MIT Cheetah. This is because the MIT Cheetah was initially designed with biomimetic intentions and attaining high running speeds rather than focusing on 3D agility via omni-directional running and jumping.

Chapter 4

Proprioceptive Force Control for Dynamic Virtual Compliance

4.1 Simple Legged Locomotion Controllers

The 3-RSR was designed for high fidelity proprioceptive force control to enable a leg with mechanically variable spring stiffness and dampening to be emulated by virtual compliance from electromagnetic actuators driving a stiff leg structure. To understand why variable compliance is important in legged locomotion the SLIP model and Raibert controller are described. Both legged models of locomotion assume some level of compliance in the hopping leg. Variable stiffness is also important with regard to energy efficiency at different running/hopping speeds and over terrain of varying stiffness [64][21].

4.1.1 SLIP Models

From observing cursorial creatures in nature scientists have long known that the muscles and tendons of running animals acts as springs and dampers to store and deliver energy in each gait cycle. While many robots use designs integrating passive mechanical elements such as leaf springs into the leg mechanism few robots have achieved virtual compliance at the kHz time scale required for smooth spring emulation via electromagnetic actuators [9][12][11].

The purpose of the 3-RSR leg topology and associated quasi-direct-drive scheme aim to enable high fidelity virtual model control to enable the mechanically stiff leg to act like a spring upon landing impacts prevalent in hopping. Therefore, for reference, this document includes the well known derivations of 1-DoF and 2-DoF spring-loaded-inverted pendulum (SLIP) model which is one of the simplest yet most powerful models of dynamic legged locomotion [61]. Each model has two distinct dynamics equations of motion for stance phase and flight phase.

1-DOF SLIP Model

The one degree of freedom model taken from [61] describes the motion of a monopod hopper with a mass-less spring leg of stiffness k and an effective body point mass m . The point mass is constrained to motion only in the y-direction as indicated by Figure 4.1. The model assumes

1. mass-less/inertia-less limb
2. center of mass (CoM) located at the hip
3. ideal linear spring leg with no dampening

The **stance** phase dynamics are derived using Newton's 2nd law by summation of force acting on the point mass while the foot is in contact with the ground as follows [61]

$$m\ddot{y} = k(l_0 - y) - mg \quad (4.1)$$

where l_0 is the unstretched spring-leg length. The state space variable x is then defined as

$$x = \begin{bmatrix} y \\ \dot{y} \end{bmatrix} \quad (4.2)$$

$$\dot{x}_1 = \dot{y} = 0 \quad (4.3)$$

$$\dot{x}_2 = \ddot{y} = \frac{k}{m}(l_0 - y) - g \quad (4.4)$$

The dynamics equations of motion for the stance phase are then written in state-space form as

$$\begin{bmatrix} \dot{y} \\ \ddot{y} \end{bmatrix} = \begin{bmatrix} 0 & 0 \\ -\frac{k}{m} & 0 \end{bmatrix} \begin{bmatrix} y \\ \dot{y} \end{bmatrix} + \begin{bmatrix} 0 \\ \frac{k}{m}l_0 - g \end{bmatrix} \quad (4.5)$$

The **flight** phase dynamics are much simpler as the only force acting on the body mass is gravity. Therefore, the trajectory of the mass follows ballistic flight described by

$$m\ddot{y} = mg \quad (4.6)$$

$$\ddot{y} = g \quad (4.7)$$

2-DOF SLIP Model

The 2-DoF SLIP model from [61] is an extension of the same model which adds horizontal translation to the point mass body motion. This enables hopping in a plane as opposed to a vertical line. The same simplifying assumptions used for the 1-DoF model apply.

Using the Lagrangian formulation the system dynamics for the 2-DoF model **stance** phase can be determined. Taking the difference between the systems kinetic T and potential V energy yields

$$L = T - V \quad (4.8)$$

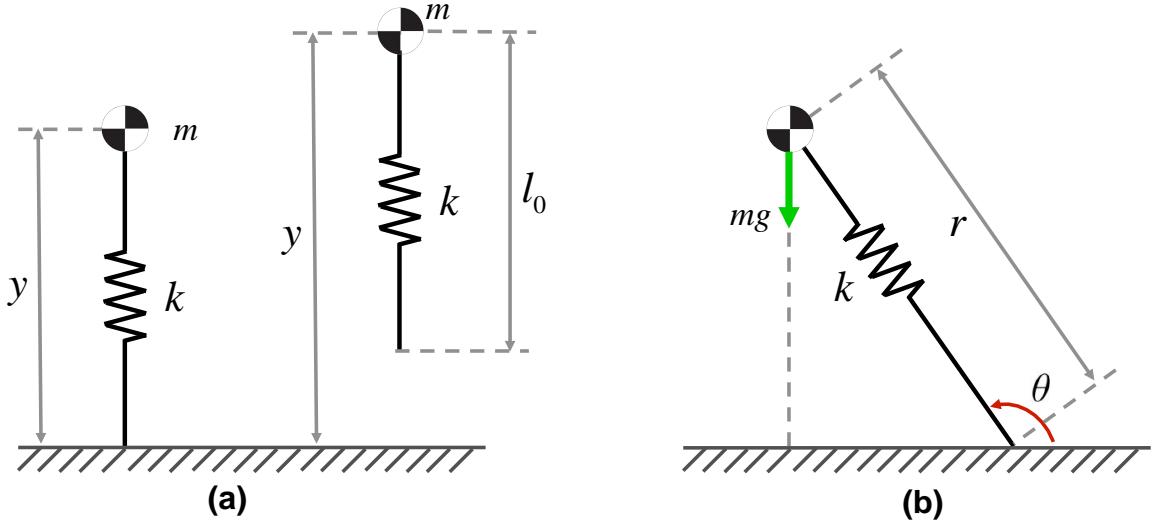


Figure 4.1: Spring-loaded inverted pendulum (SLIP) model with spring stiffness k and nominal leg length l_0 for (a) a 1-DoF hopper and (b) a 2-DoF hopper [61].

$$T = \frac{1}{2}m(\dot{r}^2 + r^2\dot{\theta}^2) \quad (4.9)$$

$$V = mg(r \sin \theta) + \frac{1}{2}k(l_0 - r)^2 \quad (4.10)$$

where the translational and angular velocity of the CoM are summed in T and the gravitational and spring potential are summed in V . Substituting T and V into L then yields

$$L = T - V = \frac{1}{2}m(\dot{r}^2 - r^2\dot{\theta}^2) - mg(r \sin \theta) - \frac{1}{2}k(l_0 - r)^2 \quad (4.11)$$

Forming state-space variables q_k

$$q_k = \begin{bmatrix} r \\ \theta \end{bmatrix} \quad \dot{q}_k = \begin{bmatrix} \dot{r} \\ \dot{\theta} \end{bmatrix} \quad \frac{\partial}{\partial L} \left(\frac{\partial L}{\partial \dot{q}_k} \right) - \left(\frac{\partial L}{\partial q_k} \right) = 0 \quad (4.12)$$

and taking the partial derivatives with respect to the state variable r

$$\begin{aligned} \frac{\partial}{\partial t} \left(\frac{\partial L}{\partial \dot{r}} \right) &= m\ddot{r} \\ \left(\frac{\partial L}{\partial r} \right) &= mr\dot{\theta}^2 - mg \sin \theta + k(l_0 - r) \\ m\ddot{r} &= -mg \sin \theta + k(l_0 - r) + mr\dot{\theta}^2 \end{aligned} \quad (4.13)$$

and the state variable θ

$$\begin{aligned}\frac{\partial}{\partial t}\left(\frac{\partial L}{\partial \dot{\theta}}\right) &= mr^2\ddot{\theta} \\ \left(\frac{\partial L}{\partial \theta}\right) &= -mgr \cos \theta\end{aligned}$$

$$r^2\ddot{\theta} = gr \cos \theta \quad (4.14)$$

The **flight** phase dynamics are again described by ballistic flight

$$\ddot{y} = g \quad (4.15)$$

$$\ddot{x} = 0 \quad (4.16)$$

The following system of equations is nonlinear and thus can be easily solved numerically, however an additional assumption simplifies the model and yields an analytical solution. The fourth assumption is

4. approximate gravity to only act along the vector of the leg (i.e. $\theta \approx 90^\circ$)

With this assumption the equations of motion for stance simplify to

$$m\ddot{r} = mr\dot{\theta}^2 + k(l_0 - r) - mg \quad (4.17)$$

$$r^2\ddot{\theta} = 0 \quad (4.18)$$

Therefore, solving the system analytically becomes feasible [61]

$$r(t) = l_0 - A \sin(\hat{\omega}t) + B(1 - \cos(\omega t)) \quad (4.19)$$

$$\hat{\omega} = \sqrt{\frac{k}{m} + 3\dot{\theta}^2} \quad (4.20)$$

4.1.2 Raibert Hopping Controller

In the late 1980's Marc Raibert at Carnegie Mellon University and later at MIT conceived the first truly dynamic hopping machines. Although these machines were tethered with off-board power and computing, the machines were capable of unprecedented motions at the time which are still impressive today.

Marc Raibert developed a control algorithm for monopod, biped, and quadruped hopping that are all essentially operating under the same control scheme. This scheme consists of three parallel, but decoupled, 1-DoF controllers operating under a finite state-machine. This control decomposition uses three separate controllers to modulate 1) hopping height, 2) forward speed, and 3) body attitude, based on the event triggers enumerated in Table 4.1.2.

The first 1-DoF controller regulates hopping height by applying leg thrust for a specified duration

State	Trigger Event	Action
1) Loading	touchdown	zero hip torque
2) Compression	leg shortens	servo body attitude with hip
3) Thrust	leg lengthens	pressurize leg, servo body with hip
4) Unloading	leg near full length	stop thrust, zero hip torque
5) Flight	ballistic	position leg for landing

Table 4.1: State machine for Raibert hopping controller [6].

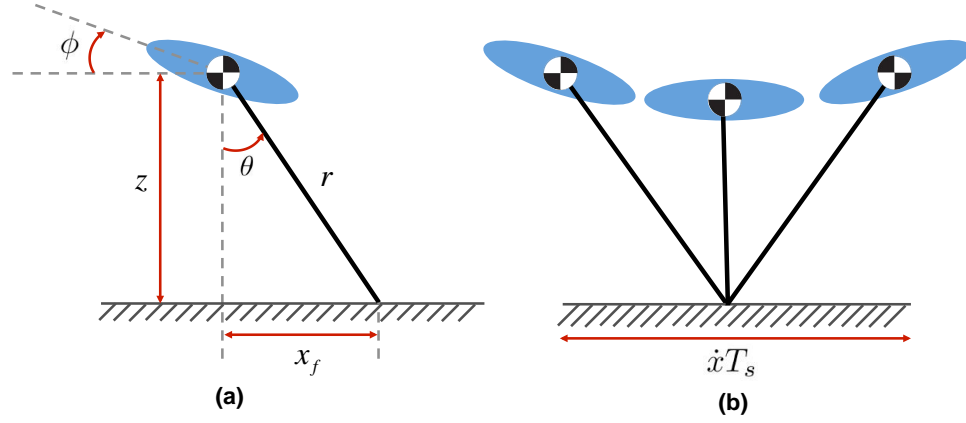


Figure 4.2: Leg model for the Raibert hopper parallel controller.

during stance phase. This leg thrust is used to accelerate the unsprung mass and input the energy lost upon impact from friction and dampening in the physical system.

The second 1-DoF controller regulates forward speed by calculated foot placement relative to the center of mass during touchdown of each step. The net forward acceleration is determined by the difference between forward speed at touchdown \dot{x}_{td} and lift-off \dot{x}_{lo}

$$\Delta\dot{x} = \dot{x}_{lo} - \dot{x}_{td}$$

where forward acceleration during flight is assumed to be zero because no horizontal forces are acting on the body in flight [6]. Therefore, all horizontal acceleration must be accomplished during stance. To accelerate the CoM the forward position of the foot upon touchdown, relative to the neutral point x_{fo} , must be calculated. The CG-print is defined by Raibert as the locus of points over which the CoG will travel during the next stance phase. From this definition the neutral-point (x_{fo}) is the center of the CG-print [6].

To accelerate the machine, the control system introduces asymmetry by displacing the foot touchdown placement from the neutral-point. This is done by the following algorithm [6]. First, the foot position upon touch-down must be calculated by

$$x_f = \frac{\dot{x}T_s}{2} + k_{\dot{x}}(\dot{x} - \dot{x}_d) \quad (4.21)$$

Using inverse kinematics the joint angles to achieve the desired foot position can be computed. In the case of the prismatic monopod hopper, the leg only consists of hip angle and leg length so the inverse kinematics are trivially solved by

$$\gamma_d = \phi - \sin^{-1}\left(\frac{x_f}{r}\right) \quad (4.22)$$

Finally, the desired hip angle is achieved by using a PID controller to servo the body angle by

$$\tau = -k_p(\gamma - \gamma_d) - k_v(\dot{\gamma}) \quad (4.23)$$

where ϕ is the body attitude, f_0 is the forward displacement in meters of the foot with respect to the CoM, \dot{x} is the forward speed in m/s , and T_s is the duration of the thrust during stance in seconds.

The final 1-DoF controller in the parallel control scheme is responsible for controlling body attitude (i.e. pitch) by servoing the hip the apply torque on the body during stance [6]. This servoing should maintain the body in an upright posture while friction holds the foot in place during stance. Another simple PID controller is used for attitude adjustment

$$\tau = -k_p(\phi - \phi_d) - k_v(\dot{\phi}) \quad (4.24)$$

where τ is the hip torque, ϕ is the pitch angle of the body, and k_p , k_v are the position and velocity feedback gains, respectively.

These three, decouple 1-DoF controllers run in parallel and maintain hopping height, forward speed, and body attitude. Extension to 3D hopping is trivial by applying the same 1-DoF controller to foot placement in the x and y axis of the ground plane for regulating horizontal speed. Similarly, for 3D hopping the same body attitude controller must now also regulate body roll in addition to body pitch.

4.2 Virtual Model Control for Compliant Dynamic Motions

Virtual model control, originally created by Jerry Pratt et. al in [25], is a force-based control frame-work that uses virtual components to create virtual forces that interact between the robot body and the environment. This control algorithm requires no dynamic model of the robot, no knowledge of the terrain or environment enabling a minimal sensory system, and requires only minimal computational power in comparison to real-time optimization for CoM trajectory planning or inverse dynamics. Virtual model control does not attempt to cancel the natural dynamics of the system but rather augments the natural dynamics with virtual components that emulate mechanical components like springs, dampers, dashpots, masses, latches, bearings, non-linear potential fields, or other force-based components [25].

The use of virtual model control for compliant monopod hopping allows virtual spring and damper components to be created using high bandwidth motors with accurate proprioceptive torque sensing to mimic the forces produced by mechanical spring and dampers.

4.2.1 Virtual Joint Compliance

Virtual joint compliance is accomplished by servoing the torque of each joint actuator to emulate the torques that would be produced if a physical **torsion spring was located in the hip joint** instead of a motor. This commanded torque (τ) at every instant is a function of the angular position error which is the difference between the nominal virtual torsion-spring position (θ_0) and the feedback joint position (θ_{fbk}) by

$$\tau = -k_s(\theta_0 - \theta_{fbk}) - k_d(\dot{\theta}) \quad (4.25)$$

4.2.2 Virtual Full Leg Compliance

Virtual full leg compliance is accomplished by servoing the torque of each joint actuator — using the Jacobian transpose method — at kHz timescales to produce foot forces which would match the force applied on the body if a physical **prismatic-spring connected the hip to the foot**. Implementing virtual spring and dampers can be done by specifying a time-varying force-torque wrench as a function of nominal foot position and foot velocity as follows.

$$F = [0 \ 0 \ f_z \ 0 \ 0 \ 0]^T \quad (4.26)$$

where,

$$f_z = k_s(z_{fbk} - z_{cmd}) + k_d(\dot{z}_{fbk} - \dot{z}_{cmd}) \quad (4.27)$$

where f_z is the vertical component of the force torque wrench to be applied by the leg emulating a virtual spring-damper, k_s is the virtual spring stiffness [N/m], k_d is the virtual dampening coefficient [N-s/m], and z is the z-coordinate of the foot position where the subscripts z_{cmd} and z_{fbk} denote the commanded and feedback positions. Typically \dot{z}_{cmd} , the commanded foot velocity in the z-direction, is set to zero. To emulate a spring applying 3D forces the force-torque wrench can be modified as such

$$F = [f_x \ f_y \ f_z \ m_x \ m_y \ m_z]^T \quad (4.28)$$

where f_x and f_y are of the same form as eq. 4.27 using the corresponding position and velocity feedback and commands x_{fbk} , y_{fbk} .

$$f_x = k_{s,x}(x_{fbk} - x_{cmd}) + k_{d,x}(\dot{x}_{fbk} - \dot{x}_{cmd}) \quad (4.29)$$

$$f_y = k_{s,y}(y_{fbk} - y_{cmd}) + k_{d,y}(\dot{y}_{fbk} - \dot{y}_{cmd}) \quad (4.30)$$

Once the virtual spring force-torque wrench F is determined with any desired spring and dampening coefficients (within the motors capabilities) the joint torques (τ) needed to produce this virtual force at any instant in time can be calculated using the Jacobian transpose of the leg (J^T) by

$$\tau = J^T F \quad (4.31)$$

To test the virtual model control the leg will jump and then land using virtual compliance to absorb the impulse and a damper to prevent oscillations. In future experiments it would be interesting to augment the system with a mechanical parallel spring combined with the virtual compliance to achieve both variable stiffness by using the virtual compliance to modulate the stiffness of the mechanical spring in real time while taking advantage of the fact that a mechanical spring can store and transmit energy for higher efficiency whereas virtual compliance alone cannot do so. The combined mechanical and virtual compliance also enables the leg to preload the mechanical spring which can then be used to induce more explosive jumping maneuvers and agile motions.

4.2.3 Simulation Model

A simulation of the leg was created in MATLAB's SimMechanics physics engine. A model of the 3-RSR leg was created, shown in Fig. 4.3, was used to simulate virtual model control for a 1-DoF hopping monopod.

The simulation dropped the leg from an initial height of 0.5 m and various virtual spring and damper coefficients were tested to determine optimal virtual component parameters for landing while absorbing energy and minimizing oscillations (i.e. bouncing). To decrease oscillations the dampening coefficient was increased and to absorb the impact of landing the spring stiffness was decreased until desired performance was achieved.

4.2.4 Experimental Validation

Control for Virtual Spring-Damper Leg

The control architecture for the 1-DoF hopping controller which uses virtual model control to virtually emulate a mechanical spring/damper is shown in Fig. 4.5. This controller allows the leg to compliantly absorb the impact during touchdown/landing, while providing large leg thrust forces for exerting large amounts of energy required for high jumping. The controller has a **Flight** and **Stance** phase of which the stance phase is composed of two sub-states: 1) stance and 2) jump.

Impedance Control Using Continuous Gain Scheduling

To achieve high-fidelity virtual compliance a modified impedance controller which modulates position gains rather than joint position to generate a desired torque trajectory was implemented. The components of the impedance control scheme are shown within the dotted box in the controller flow diagram in Fig. 4.5. Once a virtual spring-damper foot force is determined at a given instance in time, the Jacobian is used to transform that virtual spring-damper foot force into joint torques at the 3-RSR's 3 hip joints. These 3 joint torques becomes the desired torque command at the current time step. The desired joint torques τ are then fed, along with the joint position error ($pos_{err} = pos_{fbk} - pos_{cmd}$), to the impedance controller. The impedance controller then interpolates between the calibrated family of position error vs torque curves for various position gains (shown in Fig. 4.4) to determine the continuous gain value which will generate the desired torque at the current position error. This gain value is modulated and assigned at a frequency of 1 kHz¹ which enables the leg to mimic the response of a virtual spring damper at a very high bandwidth.

The controller then operates in a finite state machine as follows. While the leg is in stance and a jump is to be initiated from rest the leg is put into a crouched position and the virtual stiffness of the leg is set to be 1000 N/m. The jump is then initiated when the foot position is commanded to be fully extended. The impedance controller delivers around 6 N-m for approximately 80-100 ms while the virtual spring in the leg propels the robot upward in a dynamic and explosive jump. The controller then enters the flight phase of the finite state machine and immediately lowers the virtual leg stiffness to prepare for landing compliantly. The landing leg stiffness was tuned for the best performance as a stiffness that was too soft resulted in the foot position error upon landing being large and if the

¹modulated at 1 kHz in the high-level controller but the system bandwidth is around 200-250 Hz as shown in Fig. 4.6

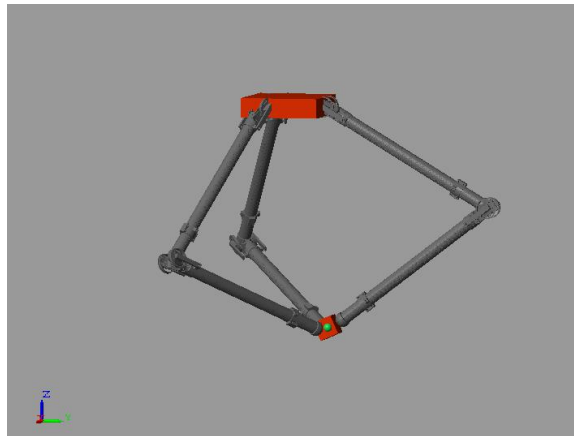


Figure 4.3: MATLAB SimMechanics model of the 3-DoF, 3-RSR leg being simulated for 1-DoF hopping and compliant landing.

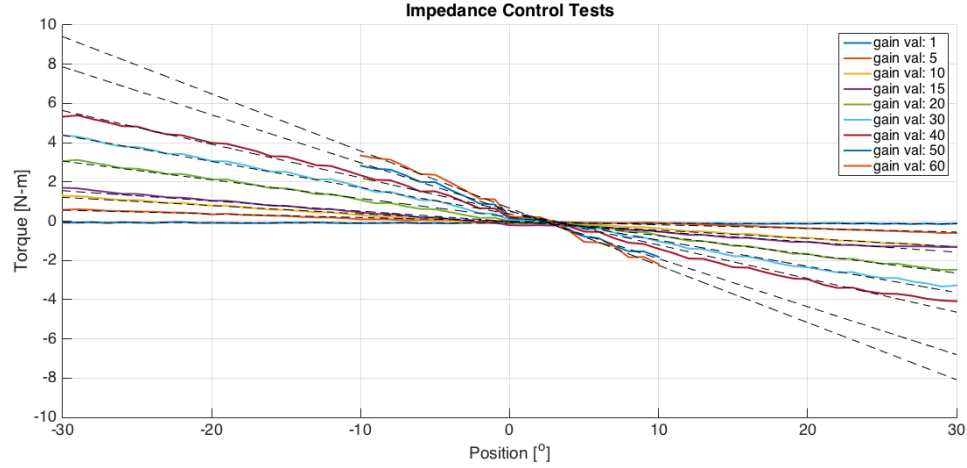


Figure 4.4: Calibration curves for the impedance controller based on gain scheduling. The impedance controller is based takes a position error and desired torque as inputs and outputs a position gain which generates the commanded input torque.

stiffness was too high there would be a larger impulse and less compliance for energy absorption during landing. A simple proprioception foot contact controller is implemented to determine ground contact to trigger a switch in the state machine from flight to stance. This contact controller is based on both instantaneous torque feedback (or foot force feedback through the leg Jacobian) as well as a history the torque feedback dating back a specified look-back window time. If instantaneous torque alone is used to determine ground contact then contact is falsely sensed true when the leg is still in flight. This is because the high stiffness during jumping and in flight cause the joint torques to fluctuate and oscillate at around $1/3$ the peak torque value (≈ 2 Nm). Therefore, torques of near 2 Nm are seen after jumping and before landing when the foot is in complete flight and the leg is

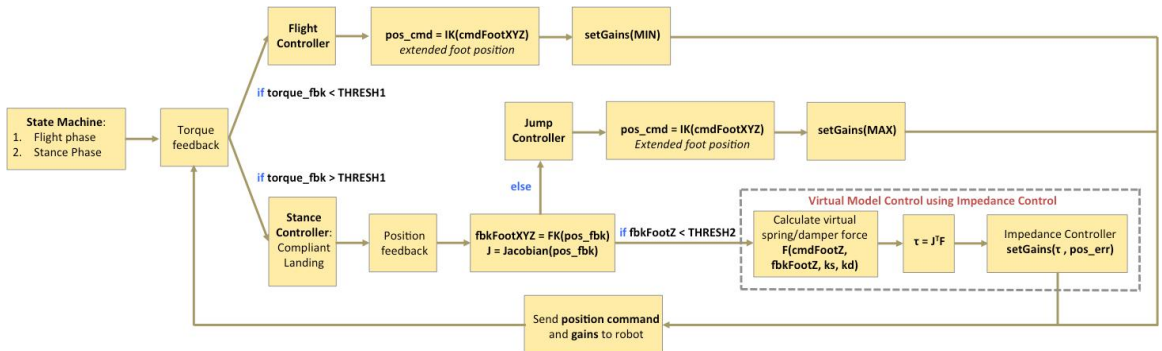


Figure 4.5: Schematic of the hopping control architecture using virtual model control to virtually emulate a mechanical spring/damper. This allows the leg to compliantly absorb the impact during touchdown/landing.

stabilizing from the jump impulse it just delivered. Therefore, if a torque threshold alone is applied to determine ground contact, that threshold would have to be around 2N-m or greater. A threshold that large significantly reduces the bandwidth of contact sensing or 'reaction time' from which the robot can switch its state machine from the flight controller to the stance controller. This is because once the leg comes into contact with the ground the torque feedback only method of proprioception will wait until the joint torques (or foot force) reach 2 Nm before triggering a switch in states. This time could be on the order of milliseconds which is visible through experimentation. Therefore by using the torque feedback history the contact controller can 'filter out' any false positive contacts that occur while in flight because those torque peaks of 2 Nm only last temporarily and switch signs whereas torque does not switch sign upon initial ground contact until the rebound occurs (i.e. when the body begins to move upward again after landing). This second method also decreases contact sensing bandwidth because it requires looking back at a short window of time but can be tuned to detect contact faster and more accurately than the first method. A contact controller can be avoided all together by fine tuning the landing stiffness (position gain of the foot) such that foot position is adequate without compromising landing compliance significantly. In this case the state machine is triggered by a designated admissible timer which always underestimates the time it takes for the robot to land after a jump. From testing, a timer value of 0.2 seconds seems to always work.

Once a land occurs and the state machine is switch to stance phase, the virtual model impedance controller operates and modulates hip torques to produce effective whole leg compliance which mimics a mechanical spring between the hip and the foot. This controller operates until the foot position or virtual spring is compressed passed a certain threshold in which the jump controller is called in the case of continuous hopping. This allows the energy transfer of the landing rebound to aid the motors in generating leg lift-off thrust to jump again. Once a jump occurs, the produce repeats to produce cyclic hopping with a stable apex hopping height.

4.2.5 Virtual Compliance Experiments

Using the continuous gain scheduling impedance controller, precise torques could be generated at the hip joint at over 200 Hz enabling high fidelity virtual model control. Numerous tests were conducted using various virtual spring and dampers. Virtual compliance was tested at the joint level as joint compliance — emulating the use of physical torsion springs at hip — and as full leg compliance — emulating the use of a physical spring-damper connecting the hip to the foot. These two virtual compliance approaches are shown in Fig. 4.8. The results for three such tests using virtual joint and full leg compliance are shown in Fig. 4.12. The two top rows correspond to torsional joint springs with stiffness of 18 and 36 Nm/rad, respectively, while the bottom plot has a full leg virtual stiffness of 250 N/m and dampening of 10 N-s/m. The full leg compliance uses a rectified virtual linear spring-damper in which the spring can only exert forces in the negative z-direction. This rectified spring is used to achieve shorter settling times and lower percent overshoot which is normally handled by

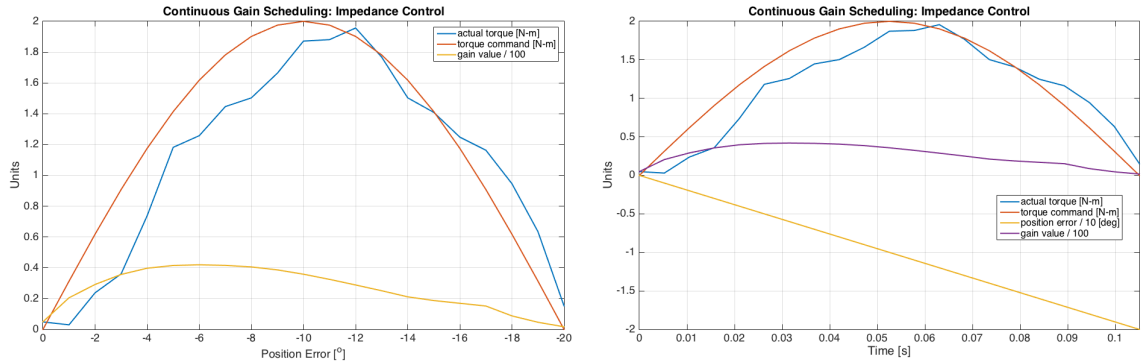


Figure 4.6: Experimental results using impedance controller based on continuous gain scheduling. The position error increases linearly with time but the commanded torque trajectory is non-linear (sinusoidal). Any arbitrary torque trajectory can be chosen; the continuous gain scheduler will modulate the gain based on the desired torque and the current position error. The torque trajectory is followed within 10% error by the direct-drive actuator at a bandwidth greater than 200 Hz.

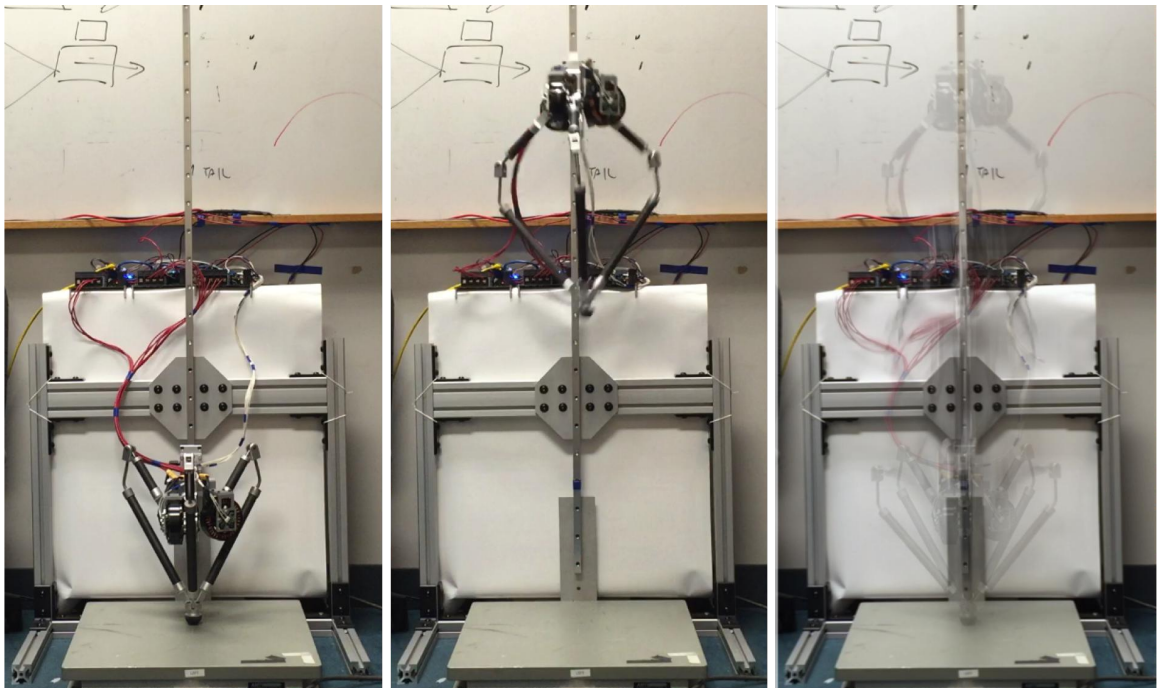


Figure 4.7: High jump experiments with the GOAT leg delivering 20.11 J of energy to produce a maximum jump height of 82 cm which is more than double the body height. For Full video: <https://www.youtube.com/watch?v=n319xVomJTQ>

Robot	Legs #	DoF #	Leg Length [m]	Mass [kg]	Motor Mass %	Gear Ratio	Max Vertical Jump Height [m]	Energy Delivered [J]
GOAT	1	3	0.26	2.5	48	n/a	0.82	20.11
MIT Cheetah	4	3	0.275	33	24	5.8	0.5	161.9
Minitaur	4	2	0.2	5.0	40	n/a	0.48	23.5
XRL	6	1	0.2	8	11	23	0.425	33.3
Delta Hopper	1	3	0.2	2.0	38	n/a	0.35	6.9
StarlETH	4	3	0.2	23	16	100	0.32	72.2
HRP3La-JSK	2	6	0.6	54	9.2	??	0.27	143
ATRIAS	2	3	0.42	60	11	50	0.11	64.7

Table 4.2: Agile Performance Comparison in Dynamic Legged Robots. The bulk of the data from this table has been tabulated and presented originally by Kenneally et. al in [12]. The performance specifications of GOAT are added to Kenneally’s table for purpose of comparison to other dynamic legged machines. We introduce a slightly different metric however for vertical agility which is just the max jumping height of the robot’s body and the energy delivered to the body during the jump. DoF is the degrees of freedom per leg.

increasing the virtual damper force. However, feedback during experiments yielded a noisy derivative term in the virtual damper force $k_d(\dot{z}_{fbk} - \dot{z}_{cmd})$. Therefore, the rectified spring has a similar effect on performance as increasing the dampening would but it allows for relatively low virtual dampening coefficients since high coefficients amplify the noise which results in leg jitter. The response for the whole leg compliance with rectified spring-damper force is shown to be ideal as the settling time is the shortest at 0.17 seconds compared to the settling times of the joint compliance (≥ 2 seconds). In these tests the two performance results desired were minimized settling time and minimized overshoot²

Vertical Agility Experiments

Several high jump experiments were conducted to determine the maximum jumping height for the leg. Within the preliminary tests a maximum jumping height of 82 cm was attained. The robot was able to land compliantly from all jump heights indicating that joint torques required for landing were not the limiting factor. The experimental energy delivered E_d during the highest jump was found to be 20.11 J.

$$E_d = mgh_{peak} = (2.5 \text{ kg})(9.81 \frac{m}{s^2})(0.82 \text{ m}) = 20.11 \text{ J} \quad (4.32)$$

Although the Table 4.2 shows that the GOAT leg is capable of jumping higher than any other electrically actuated legged robot, this comparison is not currently fair as the rest of the robots have on board power and electronics which is currently off-board for GOAT. The added weight of the

²where overshoot would lead to the leg hopping once it rebounded off the ground and long settling times would mean the robot oscillated for longer than desired before reaching steady state.

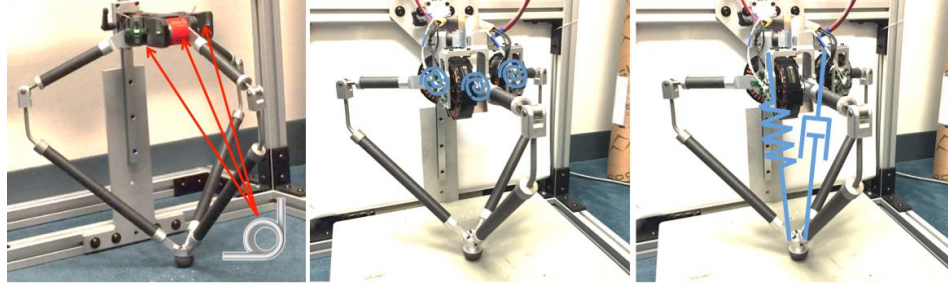


Figure 4.8: Experiments were conducted to compare (from left to right) 1) physical joint compliance using mechanical torsion springs in each of the three hip joints without any motors, 2) virtual joint compliance where motors are used to emulate torsion springs of various stiffness in the hip (no physical springs), and 3) virtual full leg compliance where motors are used to emulate the forces of a spring-damper connecting the hip to the foot (no physical springs). Virtual component placement is shown in blue.

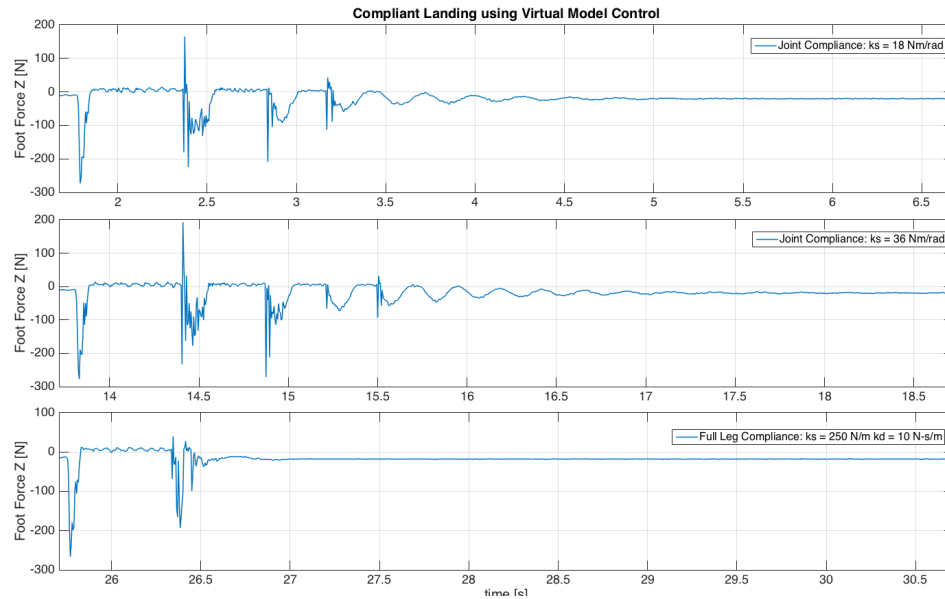


Figure 4.9: Experiments using 3 different virtual spring stiffness' and dampening coefficients and observing the response upon landing. The top two plots have virtual joint compliance with stiffness of 18 and 36 Nm/rad while the bottom plot has a full leg virtual rectified spring stiffness of 250 N/m and dampening of 10 N-s/m. The response for the whole leg compliance is ideal with the shown parameters.

battery and electronics is expected to be around 0.5 to 1 kg.

4.2.6 Proprioceptive Foot Force Sensing

To determine the accuracy of the proprioceptive foot force sensing capabilities the leg was commanded to jump a certain height and then land while the torque at each of the motors was calculated by directly measuring current draw ($\tau_m = k_t * i$). The motor torques τ_{fbk} were then used with the inverse leg Jacobian transpose $(J^T)^{-1}$ in eq. 4.33 to determine the foot force which should have been produced (assuming no friction in the mechanism).

$$F_p = (J^T)^{-1} \tau_{fbk} \quad (4.33)$$

This proprioceptive foot force F_p was then compared to a 6-axis force plate at the foot for ground truth. The max error in foot force sensing through proprioceptive current sensing was determined to be 36%. The average error however is much lower at 16% which gives an indication of the quality of the force transparency of the actuator and leg mechanism combined. These initial tests were conducted on a 1-DOF vertical jumping test rig and results from two such tests are shown in Figs. 4.10-4.11. The oscillations after the immediate jump are due to high position gains from the impedance controller when the leg is in flight (i.e. the leg is not in contact with the force plate).

4.2.7 1-DoF Vertical Hopping

Hopping tests were also included in the preliminary experiments. The hopping control framework described in Fig. 4.5 is used to deliver leg thrusts during take-off and operate using a continuous gain scheduling impedance controller during landing to absorb impacts smoothly using virtual compliance. The data from a sample of 10 seconds of 30 cm hopping at 1.5 Hz on a 1-DoF test rig is shown in Fig. 4.12. The leg was commanded to have a virtual whole leg compliance emulating a rectified prismatic spring with a stiffness of 375 N/m and dampening of 0 N-s/m.

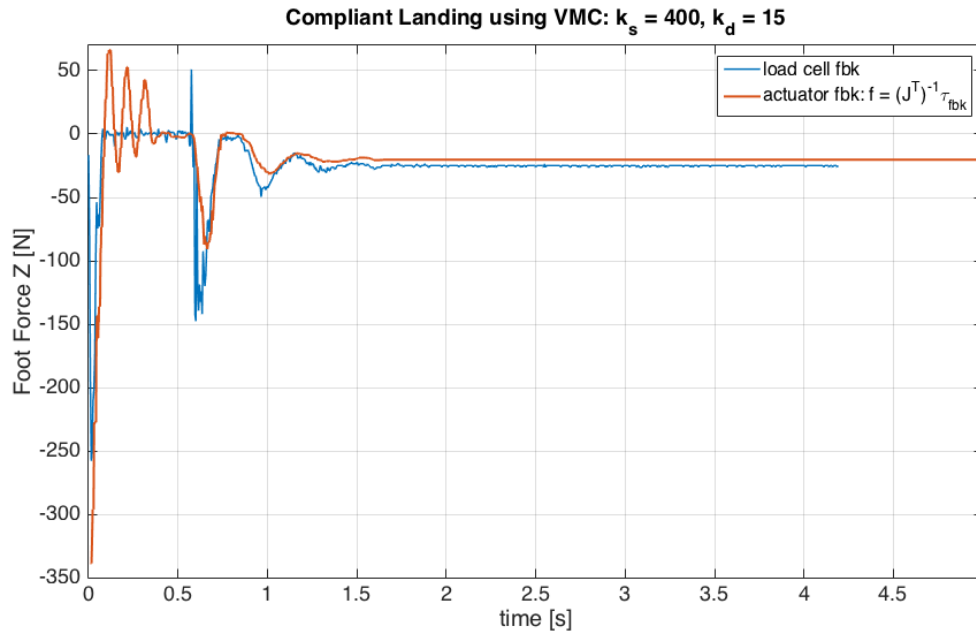


Figure 4.10: To determine the accuracy of the proprioceptive sensing of foot forces through motor current the actuator torque feedback is plugged into eq 4.33 to calculate the foot force. This calculated proprioceptive foot force is then compared to the ground truth from the 6-axis force-torque plate. The data shown here is from a jump/land experiment with virtual whole leg compliance with stiffness of 400 N/m and dampening of 15 N-s/m.

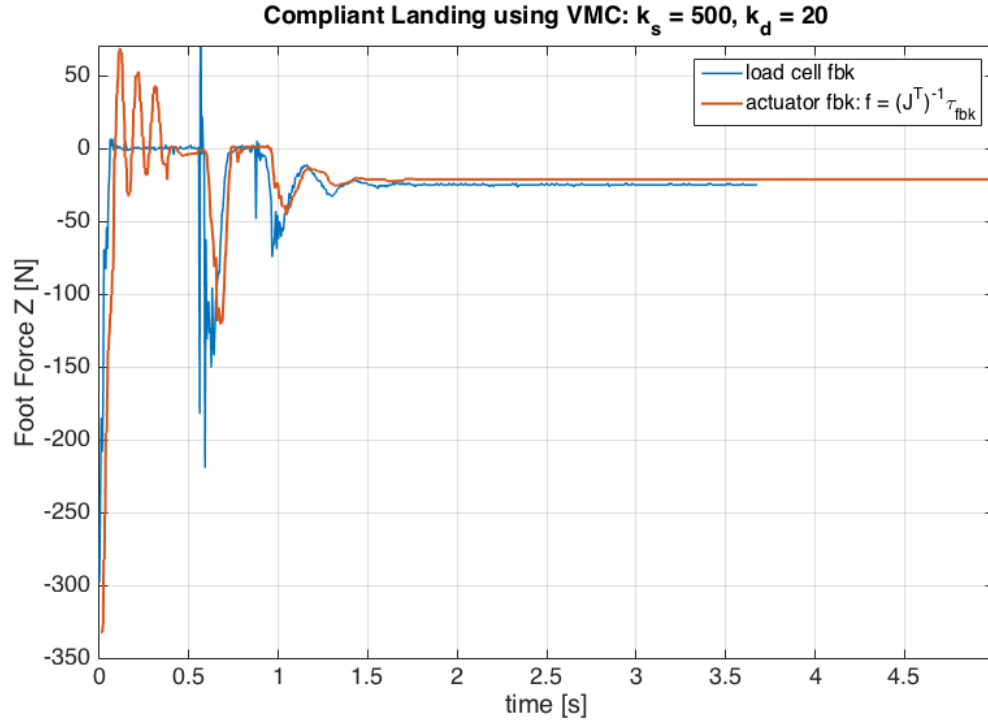


Figure 4.11: Data from a second test showing proprioceptive foot force sensing accuracy during a jump/land experiment.

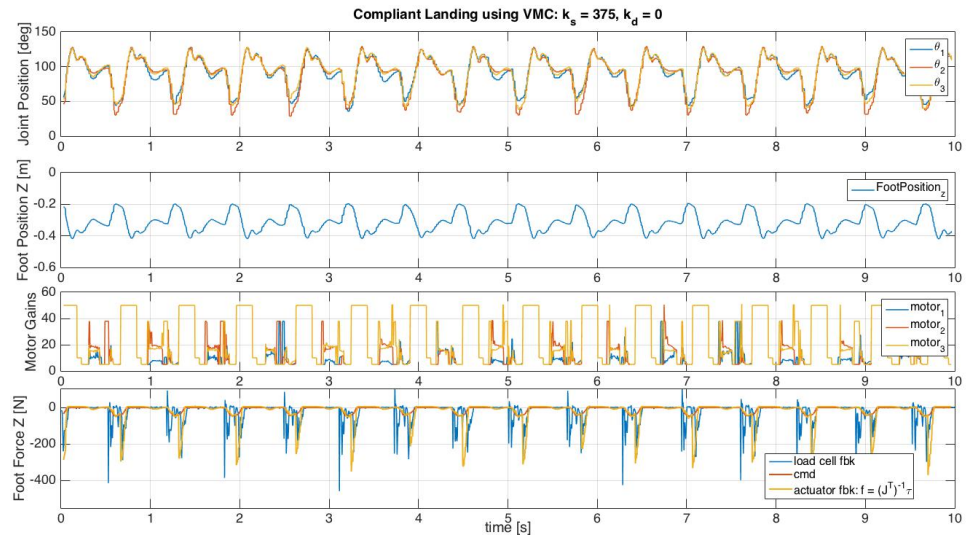


Figure 4.12: GOAT leg performing continuous 30 cm hopping at 1.5 Hz on a 1-DoF test rig.

Chapter 5

Conclusion and Future Work

At the time of this writing the GOAT leg has just been conceived and has only undergone a few weeks of preliminary testing. There is still plenty of analysis and further experimentation that can and should be done to further characterize the leg's current performance and the magnitude of its potential future performance. The first order of work that must be done is to finish the custom electronics and motor controllers so that all the electronics and power can be mounted on-board the robot. Once that is done a more fair maximum jumping height can be attained and GOAT can be compared more closely to other, untethered, agile jumping legged robots. Energy tests measuring the cost of transport and the efficiency of the entire leg system in converting electrical energy into gravitational potential energy during a jump would also be interesting for comparison purposes between direct-drive and quasi-direct drive actuation. It is expected that quasi-direct-drive will consume much less energy because the motors will not be operating in their most inefficient regime (low speed high torque) where Joule heating losses dominate energy consumption. These measures will also be important to understand where GOAT falls with respect to efficiency as compared to other robots with high efficiency like the MIT Cheetah.

Once the custom electronics are developed, the leg will ideally be removed from the 1-DoF test rig and tested in fully unconstrained 3D space (6-DoF) initially using simple Raibert style controllers. This will allow for true testing of the leg's robustness to 3D forces during omni-directional hopping.

Another interesting avenue for future research is augmenting the GOAT leg with a physical spring connecting the hip to the foot. This will allow the leg to recycle energy from stride to stride in the gait cycle by storing kinetic energy during touch-down as elastic energy and then re-delivering that energy during take-off. The effective stiffness of the leg could still be modulated by using virtual compliance in parallel with physical compliance to attain the benefits of both variable stiffness and energy recycling for enhanced efficiency.

Finally, perhaps the most exciting avenue for future exploration is adapting the GOAT leg to alternative robot morphologies like a biped or quadruped which have more stability than a monopod.

This would allow for a whole host of other agility maneuvers to be created, tested, and further explored. Because the leg is capable of delivering omni-directional force, a biped or quadruped using the leg topology will most likely behave unlike any other legged robots or legged animals. Instantaneous direction changes while running have the potential to create very unique mobility for future robots that has been unseen to this point in time.

There are many other potential paths for future research with this leg but at the current time the only certainty is that more testing and experimentation in 3D needs to be done to truly determine what the full potential of the GOAT leg is and if it has real-world utility.

Bibliography

- [1] National Geographic, Mountain Goat. [Online]. Available: <http://animals.nationalgeographic.com/animals/mammals/mountain-goat/>
- [2] Boston Dynamics [Online]. Available: bostondynamics.com
- [3] Atlas, The Next Generation. Boston Dynamics. <https://www.youtube.com/watch?v=rVlhMGQgDkY>
- [4] Introducing SpotMini. Boston Dynamics. <https://www.youtube.com/watch?v=tf7IEVTDjng>
- [5] Atlas, The Next Generation. Boston Dynamics. <https://www.youtube.com/watch?v=rVlhMGQgDkY>
- [6] M. Raibert, Legged robots that balance. MIT Press Cambridge, MA, 1986.
- [7] M. Raibert, K. Blankespoor, G. Nelson, and R. Playter, Bigdog, the rough- terrain quadruped robot, Proceedings of the 17th International Federation of Automation Control. April 2008.
- [8] C. Semini. "HyQ - Design and Development of a Hydraulically Actuated Quadruped Robot." Doctoral Thesis, Italian Institute of Technology, April 2010.
- [9] S. Seok, A. Wang, D. Otten, and S. Kim, Actuator design for high force proprioceptive control in fast legged locomotion, 2012 IEEE/RSJ International Conference on Intelligent Robots and Systems, 2012.
- [10] C. Hubicki, J. Grimes, M. Jones, D. Renjewski, A. Sprowitz, A. Abate, And J. Hurst. "ATRIAS: Design and Validation of a Tether-free 3D-capable Spring-Mass Bipedal Robot." The International Journal of Robotics Research. June 10, 2016.
- [11] M. Hutter. "StarLETH & Co. Design and Control of Legged Robots with Compliant Actuation." Doctoral Thesis, ETH, 2013.
- [12] G. Kenneally, A. De, D. Koditschek. "Design Principles for a Family of Direct-Drive Legged Robots." IEEE ROBOTICS AND AUTOMATION LETTERS, VOL. 1, NO. 2, JULY 2016.

- [13] K. Galloway, G. Haynes, B. Ilhan, A. Johnson, R. Knopf, G. Lynch, B. Plotnick, M. White, and D. Koditschek. "X-RHex: A Highly Mobile Hexapedal Robot for Sensorimotor Tasks."
- [14] G. C. Haynes, J. Pusey, R. Knopf, A. M. Johnson, and D. E. Koditschek, Laboratory on legs: an architecture for adjustable morphology with legged robots, in Unmanned Systems Technology XIV, R. E. Karlsen, D. W. Gage, C. M. Shoemaker, and G. R. Gerhart, Eds., vol. 8387. SPIE, 2012, p. 83870W.
- [15] W. Bosworth, S. Kim, N. Hogan. "The MIT Super Mini Cheetah: A small, low-cost quadrupedal robot for dynamic locomotion." IEEE, SSR. West Lafayette, Indiana, 2015.
- [16] "Google owned Schaft unveils new bipedal robot." <https://www.youtube.com/watch?v=iyZE0psQsX0>
- [17] W. Townsend, "The Effect of Transmission Design on Force-Controlled Manipulator Performance." Doctoral Thesis, Massachusetts Institute of Technology, April 1988.
- [18] W. Townsend, K. Salisbury. "Mechanical bandwidth as a guideline to high-performance manipulator design." IEEE International Conference on Robotics and Automation, 1989.
- [19] H.B. Brown, G. Zeglin. "The Bow Leg Hooping Robot." Proceedings. 1998 IEEE International Conference on Robotics and Automation, 1998.
- [20] B. Zeglin. "The Bow Legged Hopping Robot" Doctoral Thesis, Carnegie Mellon University, 1999.
- [21] J. Hurst. "The Role and Implementation of Compliance in Legged Locomotion." Doctoral Thesis, Carnegie Mellon, 2008.
- [22] K. Galloway. "Passive Variable Compliance for Dynamic Legged Robots." Doctoral Thesis, University of Pennsylvania, 2010.
- [23] S. Kalouche, D. Rollinson, H. Choset. "Modularity for Maximum Mobility and Manipulation: Control of a Reconfigurable Legged Robot with Series-Elastic Actuators." IEEE International Symposium on Safety, Security, and Rescue Robotics (SSRR), 2015, 1-8.
- [24] D. Rollinson. "Control and Design of Snake Robots." Doctoral Thesis, Carnegie Mellon University, 2014.
- [25] J. Pratt, C.M. Chew, A. Torres, P. Dilworth, G. Pratt. "Virtual Model Control: An Intuitive Approach for Bipedal Locomotion." The International Journal of Robotics Research Vol. 20, No. 2, February 2001, pp. 129-143.
- [26] H. Asada and K. Youcef-Toumi, Direct-drive robots: theory and practice. MIT press, 1987.

- [27] M. Murphy, A. Saunders, C. Moreira, A. Rizzi, and M. Raibert, "The LittleDog Robot," *International Journal of Robotics Research*, 2010.
- [28] Sand Flea Jumping Robot. Boston Dynamics. <https://www.youtube.com/watch?v=6b4ZZQkcNEo>
- [29] J. M. Duperret, G. D. Kenneally, J. L. Pusey, and D. E. Koditschek. "Towards a Comparative Measure of Legged Agility." *Experimental Robotics: The 14th International Symposium on Experimental Robotics*, 2016.
- [30] S. Seok, A. Wang, M. Chuah, D. Hyun, J. Lee, D. Otten, J. Lang, Fellow, IEEE, and S. Kim "Design Principles for Energy-Efficient Legged Locomotion and Implementation on the MIT Cheetah Robot." *IEEE/ASME Transactions on Mechatronics*, 2015.
- [31] H. Park, S. Kim. "The MIT Cheetah, an Electrically-Powered Quadrupedal Robot for High-speed Running." *Journal of the Robotics Society of Japan*, Vol. 32 No. 4, pp.323-328, 2014.
- [32] M. Woodward, M. Sitti. "Design of a Miniature Integrated Multi-Modal Jumping and Gliding Robot." *2011 IEEE/RSJ International Conference on Intelligent Robots and Systems*. 2011 SF, CA.
- [33] T. Tanaka, S. Hirose. "Development of Leg-Wheel Hybrid Quadruped "AirHopper" Design of Powerful Light-weight Leg with Wheel." *2008 IEEE/RSJ International Conference on Intelligent Robots and Systems*. 2008, Nice, France.
- [34] B. Wilcox. "ATHLETE: A Cargo-Handling Vehicle for Solar System Exploration" *Aerospace Conference*, 2011 IEEE.
- [35] M. Piccoli, S. Revzen, M. Yim, "SEAL Pack Versatile, Portable, and Rapidly Deployable SEa, Air, and Land vehicle." *2013 IEEE International Symposium on Safety, Security, and Rescue Robotics*.
- [36] S. Latscha, M. Kofron, A. Stroppolo, L. Davis, G. Merritt, M. Piccoli, M. Yim. "Design of a Hybrid Exploration Robot for Air and Land Deployment (H.E.R.A.L.D) for Urban Search and Rescue Applications. *2014 IEEE/RSJ International Conference on Intelligent Robots and Systems (IROS 2014)* September 14-18, 2014, Chicago, IL, USA
- [37] J. Whitney, T. Chen, J. Mars, and J. Hodgins. "A Hybrid Hydrostatic Transmission and Human-Safe Haptic Telepresence Robot." *Disney Research*, 2016.
- [38] J. McKenzie. "Design of Robotic Quadruped Legs." *Masters Dissertation*. MIT, 2012.

- [39] A. Tsiokanos, E. Kellis, A. Jamurtas, and S. Kellis, Passive bipedal running, The relationship between jumping performance and isokinetic strength of hip and knee extensors and ankle plantar flexors, vol. 10, pp. 107115, 2002.
- [40] L. D. Maes, M. Herbin, R. Hackert, V. L. Bels, and A. Abourachid, Steady locomotion in dogs: temporal and associated spatial coordination patterns and the effect of speed, Journal of Experimental Biology, vol. 211, no. 1, pp. 138149, 2008.
- [41] C. Semini et al., "Additive manufacturing for agile legged robots with hydraulic actuation," Advanced Robotics (ICAR), 2015 International Conference on, Istanbul, 2015, pp. 123-129.
- [42] E. Ackerman. "What Boston Dynamics is Working On Next." [Online]. Available: <http://spectrum.ieee.org/automaton/robotics/humanoids/what-boston-dynamics-is-working-on-next>
- [43] G. Kenneally, D. Koditschek. "Leg Design for Energy Management in an Electromechanical Robot." 2015 International Conference on Intelligent Robots and Systems, September, 2015.
- [44] J. Grimes. "ATRIAS 1.0 & 2.0 - Enabling Agile Biped Locomotion with a Template-Driven Approach to Robot Design." Masters Thesis, Oregon State University, 2013.
- [45] Wikipedia. "Specific Strength." [Online]. Available: https://en.wikipedia.org/wiki/Specific_strength
- [46] A. Hughes. "Electric Motors and Drives: Fundamentals, Types and Applications." ISBN: 9780080522043, 2005.
- [47] S. Colton. "Design and Prototyping Methods for Brush-less Motors and Motor Control." Masters Thesis, MIT, 2010.
- [48] J. Urata, T. Hirose, Y. Namiki, Y. Nakanishi, I. Mizuuchi and M. Inaba. "Thermal Control of Electrical Motors for High-Power Humanoid Robots." 2008 IEEE/RSJ International Conference on Intelligent Robots and Systems. France, 2008.
- [49] J. Urata, Y. Nakanishi, K. Okada, and M. Inaba, Design of high torque and high speed leg module for high power humanoid, in Intelligent Robots and Systems (IROS), 2010 IEEE/RSJ International Conference on. IEEE, 2010, pp. 4497 4502.
- [50] "Maxon DC motor Permanent magnet DC motor with coreless winding." Maxon Academy, maxonmotorusa.com, Nov, 16, 2015.
- [51] S. Kim. "MIT Cheetah - New Design Paradigm Shift Toward Mobiles Robots." [Online]. Available: <https://www.youtube.com/watch?v=R0dgELUeBTU>

- [52] G. Wyeth. "Control Issues for Velocity Sourced Series Elastic Actuators." Proceedings of the Australasian Conference on Robotics and Automation 2006.
- [53] A. Schepelmann, M. Taylor, H. Geyer. "Development of a Testbed for Robotic Neuromuscular Controllers," Robotics Systems and Science, 2008.
- [54] M. Piccoli and M. Yim, Cogging torque ripple minimization via position based characterization, in Proceedings of Robotics: Science and Systems, 2014.
- [55] S. Ford, D. Rollinson, A. Willig, and H. Choset. "Online Calibration of a Compact Series Elastic Actuator." IEEE ACC, Portland, OR, 2014.
- [56] Field Oriented Control (FOC) Made Ultra Simple. [Online]. Available: <http://www.roboteq.com/index.php/support/microbasic-reference/100-applications/how-to/359-field-oriented-control-foc-made-ultra-simple>.
- [57] WetSavannaAnimal aka Rod Vance (<http://physics.stackexchange.com/users/26076/wetsavannaanimal-aka-rod-vance>), Is squared motor gearbox ratio proportional to inertia ratio?, URL (version: 2013-08-08): <http://physics.stackexchange.com/q/73543>
- [58] G. Pratt, M. Williamson. "Series elastic actuators." Intelligent Robots and Systems 95.'Human Robot Interaction and Cooperative Robots', Proceedings. 1995 IEEE/RSJ International Conference on. Vol. 1. IEEE, 1995.
- [59] N. Paine. "High-Performance Series Elastic Actuation." Doctoral Thesis, University of Texas, 2014.
- [60] H. Horn, D. Wood, K Korane. "Planetary gears A review of basic design criteria and new options for sizing." [Online]. Available: <http://machinedesign.com/mechanical-drives/planetary-gears-review-basic-design-criteria-and-new-options-sizing>
- [61] R. Blickhan. "The Spring-Mass Model for Running and Hopping." J. Biomechanics Vol. 22, No 11/12, pp. 1217-1227, 1989.
- [62] H. Geyer, A. Seyfarth, R. Blickhan. "Compliant leg behaviour explains basic dynamics of walking and running." Proc. R. Soc. B (2006) 273, 28612867 doi:10.1098/rspb.2006.3637 Published online 11 August 2006.
- [63] Blickhan R., and Full R. Similarity in multilegged locomotion: bouncing like a monopode. Journal of Comp Phys A 173.5 (1993): 509-517.
- [64] D. Ferris, M. Louie, C. Farley. "Running in the real world: adjusting leg stiffness for different surfaces." Proc Biol Sci. 1998 Jun 7; 265(1400): 989994.

- [65] . M. Murray, Z. Li, S. S. Sastry, and S. S. Sastry, A Mathematical Introduction to Robotic Manipulation. Boca Raton, FL, USA: CRC Press, 1994.
- [66] McMaster-Carr. [Online]. Available: www.mcmaster.com
- [67] The Engineering Toolbox: Metal and Alloy Density. [Online]. Available: http://www.engineeringtoolbox.com/metal-alloys-densities-d_50.html
- [68] Microsemi. "Park, Inverse Park and Clarke, Inverse Clarke Transformations MSS Software Implementation User Guide." [Online]. Available: <http://www.microsemi.com/document-portal/docview/132799-park-inverse-park-and-clarke-inverse-clarke-transformations-mss-software-implementation-user-guide>
- [69] M. Zieserl. "Using Magnetic Sensor ICs In Highly Magnetic Environments." Online: Available sensorsmag.com, September 2015.
- [70] H., Neville. Impedance control: An approach to manipulation. American Control Conference, 1984. IEEE, 1984.
- [71] . D. Maes, M. Herbin, R. Hackert, V. L. Bels, and A. Abourachid, Steady locomotion in dogs: temporal and associated spatial coordination patterns and the effect of speed, Journal of Experimental Biology, vol. 211, no. 1, pp. 138149, 2008.
- [72] A. De, D. Koditschek. "The Penn Jerboa: A Platform for Exploring Parallel Composition of Templates." Technical Report, University of Pennsylvania, 2014.
- [73] M. Hutter, C. Gehring, M. H. Pflinger, M. Bloesch, and R. Siegwart, Fellow, IEEE. "Toward Combining Speed, Efficiency, Versatility, and Robustness in an Autonomous Quadruped." IEEE TRANSACTIONS ON ROBOTICS, VOL. 30, NO. 6, DECEMBER 2014 1427.